ULTRAWIDE STOP BAND IN A 3D ELASTIC METAMATERIAL WITH INERTIAL AMPLIFICATION MECHANISMS HAVING CROSS FLEXURE HINGES

by
Sedef Nisan Otlu
B.S., Program Name, Boğaziçi University, 2017

Submitted to the Institute for Graduate Studies in
Science and Engineering in partial fulfillment of
the requirements for the degree of
Master of Science

Graduate Program in Mechanical Engineering
Boğaziçi University
2022

ACKNOWLEDGEMENTS

First of all, I would like to offer my deep and sincere gratitude to Prof. Çetin Yılmaz. He is an admirable scientist and pure genius. Without his valuable guidance, I could not have completed this work with success.

I would like to thank to Osman Yüksel, Semih Tanıker and Adil Han Orta, who have significantly contributed to the initial stages of this study and helped me willingly throughout my study. I also owe a great thank to Berkay Acar for his technical support and notable contribution.

Finally, I wish to express my special appreciation to my beloved family: my little son, Doğa, and my husband, Burak. They have witnessed the entire process of my study and and given a deeper meaning to it. I would also like to thank my brother, Cem, and especially my mother, Semra, who has brought me up to this day. I am grateful to all of you for your emotional support and providing me a comfortable and lovely working environment.

This work was supported by TUBITAK Grant No. 218M475.

ABSTRACT

ULTRAWIDE STOP BAND IN A 3D ELASTIC METAMATERIAL WITH INERTIAL AMPLIFICATION MECHANISMS HAVING CROSS FLEXURE HINGES

Inertial amplification is a new method to obtain phononic band gaps in periodic structures. The aim in this thesis is to obtain an ultrawide stop band in three dimensions by using inertial amplification mechanisms. In order to be used in three dimensions, a two stage remote center flexure mechanism design that allows bending in two orthogonal axes is added to the ends of the inertial amplification mechanism. Moreover, cross flexure hinges that prevent undesired torsional, in-plane and out-of-plane bending modes of the inertial amplification mechanism are utilized in order to maximize the stop band frequency range. An octahedron structure is formed with this mechanism, which is also used as the building block of a 3D periodic structure. It is shown that a wide stop band can be achieved with the use of cross flexure hinges and a two stage remote center flexure mechanism. By making design and dimensional changes on the mechanisms forming the octahedron, the stop band of the octahedron is widened. Finally, the stop band is maximized by optimizing the thicknesses of the flexures in the inertial amplification mechanisms.

ÖZET

ÇAPRAZ ESNEK MAFSALA SAHİP ATALET ARTIRIM MEKANİZMALARIYLA 3 BOYUTLU ELASTİK METAMALZEMELERDE ULTRA GENİŞ DURDURMA BANDI

Atalet artırımı periyodik yapılarda fonon bant aralığı oluşturan yeni bir yöntemdir. Bu tezin amacı atalet artırım mekanizmalarıyla üç boyutta çok geniş bir durdurma bandı elde etmektir. Üç boyutlu olarak kullanılabilmesi için atalet artırım mekanizmasının uçlarına iki dik eksende bükülmeye izin veren iki kademeli bir uzak merkezli esnek mekanizma tasarımı eklenmiştir. Ayrıca, durdurma bandı frekans aralığını en üst düzeye çıkarmak için atalet artırım mekanizmasının istenmeyen burulma, düzlem içi ve düzlem dışı bükülme modlarını önleyen çapraz esnek mafsallar kullanılmıştır. Bu mekanizmayla üç boyutlu periyodik yapıların yapı taşı olarak kullanılacak bir oktahedron yapısı oluşturulmuştur. Çapraz esnek mafsallar ve iki kademeli uzak merkezli esnek mekanizma kullanılarak geniş bir durdurma bandının elde edilebileceği gösterilmiştir. Oktahedronu oluşturan mekanizmalar üzerinde tasarım ve boyut değişiklikleri yapılarak oktahedronun durdurma bandı genişletilmiştir. Son olarak, atalet artırım mekanizmalarındaki esnek bağlantıların kalınlıkları eniyilenerek durdurma bandı en yüksek seviyeye getirilmiştir.

TABLE OF CONTENTS

ACKNOWLEDGEMENTS iii
ABSTRACT iv
ÖZET v
LIST OF FIGURES viii
LIST OF TABLES xvii
LIST OF SYMBOLS xix
LIST OF ACRONYMS/ABBREVIATIONS xx
1. INTRODUCTION 1
1.1. Vibration Isolation with Periodic Structures 1
1.2. Literature Review 1
2. LUMPED PARAMETER MODEL OF THE INERTIAL AMPLIFICATION MECHANISM 4
3. 3D ULTRAWIDE INERTIAL AMPLIFICATION MECHANISM DESIGN . 8
3.1. Design of End Connections 12
3.2. Design of the Inertial Amplification Mechanism 19
3.3. Design Improvements and Topological Changes Regarding the Inertial Amplification Mechanism 45
3.4. Optimization of the Inertial Amplification Mechanism 62
4. CONCLUSION 73
REFERENCES 75
APPENDIX A: ELSEVIER LICENSE NUMBER 5236891087000 85
APPENDIX B: ELSEVIER LICENSE NUMBER 5236891191376 86
APPENDIX C: ELSEVIER LICENSE NUMBER 5236891010401 87
APPENDIX D: ELSEVIER LICENSE NUMBER 5236890632592 88

APPENDIX E: ELSEVIER LICENSE
NUMBER 5236890878590 89

LIST OF FIGURES

Figure 2.1. Lumped parameter model of the inertial amplification mechanism [1]. 4

Figure 2.2. Frequency response function plot showing the width and depth of the stop band for a two degrees of freedom system. Green dashed curve is for $\omega_{p1} = 3$, $\omega_{p2} = 23$, $\omega_{z1} = 10$, $\omega_{z2} = 22.9$. Red solid curve is for $\omega_{p1} = 3$, $\omega_{p2} = 23$, $\omega_{z1} = 10$, $\omega_{z2} = 23$. 6

Figure 3.1. Inertial amplification mechanism in [2]. 8

Figure 3.2. Mode shapes of the mechanism shown in Figure 3.1. (a) First mode shape of the mechanism at 279.2 Hz. (b) Second mode shape of the mechanism at 651.9 Hz [2]. 8

Figure 3.3. 2D periodic structure in [2]. 9

Figure 3.4. Frequency response function graph of the structure shown in Figure 3.3 [2]. 10

Figure 3.5. 2D periodic structure with the shape optimized inertial amplification mechanisms in [3]. 10

Figure 3.6. 2D periodic structure with remote center flexure mechanisms at the end connections and topologically optimized mechanisms in [1]. . . 11

Figure 3.7. Inertial amplification mechanism in [4]. 12

Figure 3.8. Mode shapes of the mechanism shown in Figure 3.7. (a) First mode shape of the mechanism at 6.9 Hz. (b) Second mode shape of the mechanism at 303.6 Hz, the bending mode of the long flexures in the middle. (c) Third mode shape of the mechanism at 373 Hz, vertical translation of the rectangular blocks at the ends [4]. . . . 13

Figure 3.9. Inertial amplification mechanism in [5] 13

Figure 3.10. Mode shapes of the mechanism shown in Figure 3.9. (a) First mode shape of the mechanism at 49.6 Hz. (b) Second mode shape of the mechanism at 241.6 Hz. (c) Third mode shape of the mechanism at 248.2 Hz [4]. 14

Figure 3.11. Octahedron structure built with the mechanism shown in Figure 3.9 [5]. 14

Figure 3.12. Building a 3D periodic structure with inertial amplification mechanisms having thin end connections. (a) Inertial amplification mechanism with thin end connections. (b) Octahedron structure formed with these mechanisms [5]. 15

Figure 3.13. Inertial amplification mechanism in [1]. 16

Figure 3.14. Pin-roller type of end connection designed in [1]. 16

Figure 3.15. Four-bar mechanism with remote center of rotation for link (1) at point O, which is the intersection of the extensions of the rods (2) and (4). 17

Figure 3.16. Planar flexure hinge mechanism with remote center of rotation at the intersection of the yellow dashed lines. 17

Figure 3.17. Spatial flexure hinge mechanism design that allows bending in two orthogonal axes. (a) Isometric view. (b) Side view in the x-y plane. (c) Top view in the x-z plane. 18

Figure 3.18. Instantaneous center of rotation of the spatial flexure hinge mechanism at the center of the back surface of the rectangular prism which is the intersection of the link extensions. (a) Isometric view. (b) Side view in the x-y plane. (c) Top view in the x-z plane. . . . 19

Figure 3.19. Initial design of the mechanism. 20

Figure 3.20. Alignment of the inertial amplification mechanism. (a) Side view of the mechanism in the x-y plane. (b) Close up view of the end of the mechanism. 21

Figure 3.21. Clamped-pin roller boundary condition for the initial design of the mechanism. (a) Boundary condition at the left end. The back surface of the rectangular prism of the left end is clamped, i.e., it cannot translate or rotate in any directions. (b) Boundary condition at the right end. The front surface of the rectangular prism of the right end is coupled with the reference point RP-2, and the translations in y- and z-axes of this point are prevented but all the other degree of freedoms are free. 22

Figure 3.22. First mode shape of the mechanism imposed to clamped-pin roller boundary condition at 33.73 Hz. 22

Figure 3.23. Second mode shape of the mechanism imposed to clamped-pin roller boundary condition at 177.9 Hz. 23

Figure 3.24. Third mode shape of the mechanism imposed to clamped-pin roller boundary condition at 283.3 Hz. 23

Figure 3.25. Fourth mode shape of the mechanism imposed to clamped-pin roller boundary condition at 390.7 Hz. 24

Figure 3.26. Fifth mode shape of the mechanism imposed to clamped-pin roller boundary condition at 673.0 Hz. 24

Figure 3.27. Sixth mode shape of the mechanism imposed to clamped-pin roller boundary condition at 720.3 Hz. 25

Figure 3.28. Seventh mode shape of the mechanism imposed to clamped-pin roller boundary condition at 876.6 Hz. 25

Figure 3.29. Eighth mode shape of the mechanism imposed to clamped-pin roller boundary condition at 901.7 Hz. 26

Figure 3.30. Ninth mode shape of the mechanism imposed to clamped-pin roller boundary condition at 1118 Hz. 26

Figure 3.31. Tenth mode shape of the mechanism imposed to clamped-pin roller boundary condition at 1121 Hz. 27

Figure 3.32. Clamped-roller boundary condition for the initial design of the mechanism. (a) Boundary condition at the left end. The back surface of the rectangular prism of the left end is clamped, i.e., it cannot translate or rotate in any directions. (b) Boundary condition at the right end. Only the translation in x-axis of the side and top surfaces of the rectangular prism of the right end is allowed. . 28

Figure 3.33. First mode shape of the mechanism imposed to clamped-roller boundary condition at 33.73 Hz. 29

Figure 3.34. Second mode shape of the mechanism imposed to clamped-roller boundary condition at 300.9 Hz. 29

Figure 3.35. Third mode shape of the mechanism imposed to clamped-roller boundary condition at 334.8 Hz. 30

Figure 3.36. Fourth mode shape of the mechanism imposed to clamped-roller boundary condition at 404.4 Hz. 30

Figure 3.37. Fifth mode shape of the mechanism imposed to clamped-roller boundary condition at 719.1 Hz. 31

Figure 3.38. Sixth mode shape of the mechanism imposed to clamped-roller boundary condition at 721.1 Hz. 31

Figure 3.39. Seventh mode shape of the mechanism imposed to clamped-roller boundary condition at 888.3 Hz. 32

Figure 3.40. Eighth mode shape of the mechanism imposed to clamped-roller boundary condition at 904.5 Hz. 32

Figure 3.41. Ninth mode shape of the mechanism imposed to clamped-roller boundary condition at 1118 Hz. 33

Figure 3.42. Tenth mode shape of the mechanism imposed to clamped-roller boundary condition at 1122 Hz. 33

Figure 3.43. Clamped-free boundary condition for the initial design of the mechanism. (a) Boundary condition at the left end. The back surface of the rectangular prism of the left end cannot translate or rotate in any direction. (b) The right end is free. 35

Figure 3.44. First mode shape of the mechanism imposed to clamped-free boundary condition at 33.73 Hz. 35

Figure 3.45. Second mode shape of the mechanism imposed to clamped-free boundary condition at 34.93 Hz. 36

Figure 3.46. Third mode shape of the mechanism imposed to clamped-free boundary condition at 48.69 Hz. 36

Figure 3.47. Fourth mode shape of the mechanism imposed to clamped-free boundary condition at 178.0 Hz. 37

Figure 3.48. Fifth mode shape of the mechanism imposed to clamped-free boundary condition at 474.6 Hz. 37

Figure 3.49. Octahedron structure formed with the mechanisms in Figure 3.19. 39

Figure 3.50. 3D periodic structure formed with the octahedron structures in Figure 3.49. 40

Figure 3.51. First mode shape of the octahedron in Figure 3.49 at 34.32 Hz. . . 43

Figure 3.52. 12th mode shape of the octahedron in Figure 3.49 at 50.69 Hz. . . 44

Figure 3.53. 13th mode shape of the octahedron in Figure 3.49 at 209.7 Hz. . . 44

Figure 3.54. 37th mode shape of the octahedron in Figure 3.49 at 402.0 Hz. . . 45

Figure 3.55. Close up view of the short flexures in the second mode shape shown in Figure 3.23 at 177.9 Hz. 46

Figure 3.56. Design of cross flexures. 47

Figure 3.57. The second mode shape of the mechanism with cross flexure design at 257.8 Hz. 47

Figure 3.58. Inertial amplification mechanism with cross flexures. 48

Figure 3.59. Octahedron structure formed with the mechanisms in Figure 3.58. 49

Figure 3.60. 12th mode shape of the octahedron in Figure 3.59 at 61.99 Hz. . . 51

Figure 3.61. 13th mode shape of the octahedron in Figure 3.59 at 277.6 Hz. . . 51

Figure 3.62. Inertial amplification mechanism in Figure 3.58 with horizontal and vertical lines passing through the center of mass of the mechanism. 52

Figure 3.63. Inertial amplification mechanism with triangular blocks with reduced heights. 53

Figure 3.64. Inertial amplification mechanism with triangular blocks supported by trusses. 53

Figure 3.65. Octahedron structure formed with the mechanism in Figure 3.64. . 54

Figure 3.66. 12th mode shape of the octahedron in Figure 3.65 at 107.4 Hz. . . 56

Figure 3.67. 13th mode shape of the octahedron in Figure 3.65 at 623.0 Hz. . . 57

Figure 3.68. Inertial amplification mechanism with the added rectangular blocks in the middle. 58

Figure 3.69. Isometric view of the inertial amplification mechanism in Figure 3.68 in which the middle flexures are divided into two and placed far away from each other to increase the out-of-plane bending stiffness. 58

Figure 3.70. Octahedron structure formed with the mechanism in Figure 3.68. . 59

Figure 3.71. 12th mode shape of the octahedron in Figure 3.70 at 102.7 Hz. . . 61

Figure 3.72. 13th mode shape of the octahedron in Figure 3.70 at 630.7 Hz. . . 62

Figure 3.73. Seven different thin flexures of the inertial amplification mechanism. (a) Flexures of the first remote center mechanism, (1), flexures of the second remote center mechanism, (2), horizontal short flexures, (3), cross flexures making a 45° angle with the vertical axis, (4) and (5). (b) Long flexures in the middle, (6), and short flexures between the triangular blocks, (7). 63

Figure 3.74. Surface plot of data given in Table 3.10 with Smoothed-particle hydrodynamics method for $x_1 = 0.15$ and $x_4 = 0.08$. The red dots show the maximum point on the surfaces. (a) Isometric view. (b) Side view such that x_2 is the horizontal axis. (c) Side view such that x_3 is the horizontal axis. 69

Figure 3.75. 12th mode shape of the final design of the octahedron at 34.41 Hz. 70

Figure 3.76. 13th mode shape of the final design of the octahedron at 469.6 Hz. 71

Figure 3.77. 3x2 periodic structure formed with optimized octahedron structure. 72

Figure A.1. Elsevier license of [1] for Figures 2.1, 3.6, 3.13 and 3.14. 85

Figure B.1. Elsevier license of [2] for Figures 3.1, 3.2, 3.3 and 3.4. 86

Figure C.1. Elsevier license of [3] for Figure 3.5. 87

Figure D.1. Elsevier license of [4] for Figures 3.7, 3.8, and 3.10. 88

Figure E.1. Elsevier license of [5] for Figures 3.9, 3.11 and 3.12. 89

LIST OF TABLES

Table 1.1. Bandwidth comparison of 3D elastic metamaterials and phononic crystals in the literature whose arithmetic mean normalized bandwidth, BW, exceeds 100%. 3

Table 3.1. First ten natural frequencies of the mechanism shown in Figure 3.19 imposed to clamped-pin roller boundary condition. 27

Table 3.2. First ten natural frequencies of the mechanism shown in Figure 3.19 imposed to clamped-roller boundary condition. 34

Table 3.3. First five natural frequencies of the mechanism shown in Figure 3.19 imposed to clamped-free boundary condition. 38

Table 3.4. First 40 non-zero natural frequencies of the octahedron structure shown in Figure 3.49 imposed to free boundary conditions. 41

Table 3.5. First 40 non-zero natural frequencies of the octahedron structure shown in Figure 3.59 imposed to free boundary conditions. 50

Table 3.6. First 40 non-zero natural frequencies of the octahedron structure shown in Figure 3.65 imposed to free boundary conditions. 55

Table 3.7. First 40 non-zero natural frequencies of the octahedron structure shown in Figure 3.70 imposed to free boundary conditions. 60

Table 3.8. First 40 non-zero natural frequencies of the octahedron structure with shell elements imposed to free boundary conditions. 65

Table 3.9. Run time comparison of solid and shell models of the octahedron structure. 66

Table 3.10. 30 data points with frequency ratios in descending order determined with the Latin hypercube sampling method for the following search space: x_1 is between 0.14 and 0.17, x_2 is between 0.05 and 0.14, x_3 is between 0.05 and 0.13, x_4 is between 0.05 and 0.12. 67

LIST OF SYMBOLS

BW	Arithmetic mean normalized bandwidth
$H(\omega)$	The frequency response function
k	The stiffness of the spring in the lumped parameter model
m	The mass at ends of the spring in the lumped parameter model
m_a	The mass in the upper part of the lumped parameter model
x	The output displacement in the lumped parameter model
x_1	The first variable of the optimization
x_2	The second variable of the optimization
x_3	The third variable of the optimization
x_4	The fourth variable of the optimization
y	The input displacement in the lumped parameter model
θ	The angle between the rigid link and the spring
ω	The excitation frequency
ω_i	The ith natural frequency
ω_l	Lower limit of the stop band
ω_p	The resonance frequency of the mechanism
ω_{p1}	The first resonance frequency of a mechanism
ω_{p2}	The second resonance frequency of a mechanism
ω_u	Upper limit of the stop band
ω_z	The antiresonance frequency of the mechanism
ω_{z1}	The first antiresonance frequency of a mechanism
ω_{z2}	The second antiresonance frequency of a mechanism

LIST OF ACRONYMS/ABBREVIATIONS

1D	One Dimensional
2D	Two Dimensional
3D	Three Dimensional
DOF	Degree of Freedom

1. INTRODUCTION

1.1. Vibration Isolation with Periodic Structures

Vibration isolation is a crucial concept for many systems and structures such as buildings, vehicles, white goods, industrial machines, sensitive measurement equipment, and opto-electronic devices. In this thesis, a mechanism providing broadband vibration isolation is designed with the inertial amplification method to be used for different purposes in many fields.

Recent studies in solid-state physics show that periodic structures can be used to prevent the transmission of vibrations and elastic waves [6–27]. If the elastic waves and vibrations excite periodic structures within the frequency range called phononic band gap, they cannot propagate in the structure. These band gaps, i.e. stop bands, can occur both in infinite and finite periodic structures. In an infinite periodic structure, the transmission of the waves corresponding to the phononic band gap is completely prevented [8]. On the other hand, the transmission of waves and vibrations can be partially blocked in a finite periodic structure. The depth of the band gap in frequency response functions of finite periodic structures determines the amount of vibration isolation of the system [19, 21]. Structures having phononic band gaps can be periodic in one, two or three dimensions. While the structure periodic in one dimension can prevent the transmission of the waves coming only in this direction, the structure periodic in three dimensions can block waves from all directions [7, 11].

1.2. Literature Review

3D periodic structures known as phononic crystals and elastic metamaterials display phononic band gaps so that they inhibit the propagation of vibrations or waves in certain frequency ranges irrespective of direction or polarization. The concept of phononic band gap can be applied to many structures of different sizes. Current studies

show that the structures periodic in one dimension [4,28–36], in two dimensions [1,2,37–42] and in three dimensions [5, 43–53] are developed. In the literature, local resonators and Bragg scattering methods are generally used to obtain phononic band gaps [54]. In the Bragg scattering method, the phononic band gap with the lowest frequency that can be produced is determined by the ratio of the wave transmission speed to the dimension of a unit cell in the periodic structure, which is also known as the lattice parameter. Therefore, materials with high density and low elastic modulus or large size structures are needed to create band gaps at low frequencies. On the other hand, local resonators can provide low frequency band gaps. However, heavy resonators are needed to obtain wide band gaps in this method. Periodic structures that utilize Bragg scattering method are oftentimes called as phononic crystals, while the ones that use the local resonance method are generally called as elastic metamaterials because band gaps can be generated below the Bragg limit.

In 2007, a new method called "inertial amplification" was developed to obtain phononic band gaps [54]. In this method, the effective inertia of the wave propagation medium is increased with some embedded mechanisms. Due to the increased inertia, the transmission of waves becomes difficult and the structure provides wide band gaps at low frequencies [54, 55]. As inertial amplification allows to form band gaps below the Bragg limit, periodic structures with embedded inertial amplification mechanisms are also considered as elastic metamaterials. Inertial amplification method has been applied to 1D [4,56], 2D [1–3] and 3D [5,57,58] structures. In recent years, many works have been published that highlight the potential of this method [33, 36, 39, 51, 59–72].

In Table 1.1, the bandwidth comparison of elastic metamaterials and phononic crystals in the literature which are capable of 3D vibration isolation and whose arithmetic mean normalized bandwidth ($BW = \frac{\omega_u - \omega_l}{(\omega_u + \omega_l)/2}$) exceeds 100% are given. As can be seen in Table 1.1, the maximum BW obtained as yet is 171.5% with a frequency ratio of the upper limit of the stop band, (ω_u), to the lower one, (ω_l), of 13.06 in Ref [53]. The aim in this study is to surpass this value and obtain the widest gap in three dimensions.

Table 1.1. Bandwidth comparison of 3D elastic metamaterials and phononic crystals in the literature whose arithmetic mean normalized bandwidth, BW, exceeds 100%.

References	ω_l (Hz)	ω_u (Hz)	BW	ω_u/ω_l
Muhammad and Lim, 2021 [53]	1292.5	16875	171.5%	13.06
Martinez et al., 2021 [73]	600000	7500000	170.4%	12.5
Muhammad and Lim, 2021 [52]	1247.2	11319	160.3%	9.1
Muhammad and Lim, 2021 [52]	929.24	7847.3	157.6%	8.44
Muhammad, 2021 [50]	2207.7	17890	156.1%	8.10
Muhammad, 2021 [50]	1446.4	11656	155.8%	8.06
D'Alessandro et al., 2019 [47]	455	2337	134.8%	5.14
D'Alessandro et al., 2016 [48]	3850	18870	132.2%	4.90
Taniker and Yilmaz, 2015 [5]	50	242	131.5%	4.84
Lu et al., 2017 [49]	75000	230000	101.6%	3.07

Finally, the original contributions of this research for the literature can be summarized as follows

- Two stage remote center flexure mechanisms are used at the end connections of the inertial amplification mechanisms for the first time. This type of connection allows obtaining a wide band gap in three dimensions.
- Cross flexure hinges are used within the inertial amplification mechanisms for the first time. This type of flexures prevent undesired torsional, in-plane and out-of-plane bending modes of the inertial amplification mechanism, which can reduce the bandwidth of the mechanism.
- Size optimization is conducted to maximize bandwidth of the mechanism and an octahedron structure is built with the optimized mechanisms that achieves a stop band in which ω_u/ω_l is 13.65. Hence, the stop band is achieved with 172.7% arithmetic mean normalized bandwidth. Moreover, a 3x2 periodic structure is formed using these octahedron structures and a stop band is obtained with 167.6% arithmetic mean normalized bandwidth.

2. LUMPED PARAMETER MODEL OF THE INERTIAL AMPLIFICATION MECHANISM

The lumped parameter model describing the main principle of the inertial amplification mechanism is given in Figure 2.1 [1].

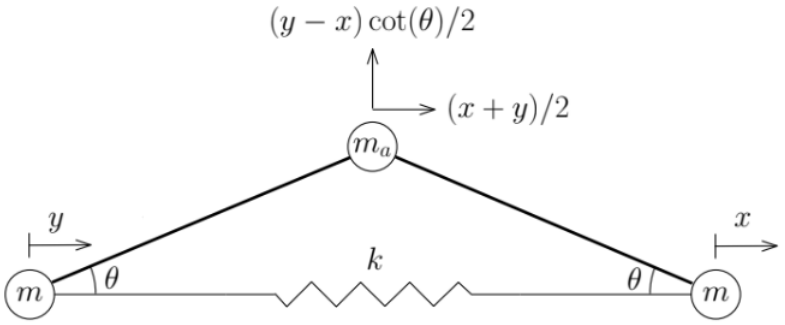


Figure 2.1. Lumped parameter model of the inertial amplification mechanism [1].

In the model shown in Figure 2.1, there are masses m at both ends of the mechanism. These masses are connected to each other by a spring with stiffness k. In the upper part of the mechanism, there is a mass m_a, which is connected to each mass m by rigid links. The angle between the links and the horizontal plane is shown as θ.

The input displacement of this mechanism is y, while the output displacement is x. In this case, the displacement of the mass m_a is calculated in terms of y and x as $\frac{x+y}{2}$ in the horizontal and $\frac{(y-x)cot(\theta)}{2}$ in the vertical directions. Therefore, motion of the mass m_a is coupled to the mass m and the base motion, and the degree of freedom of the mechanism is one.

Assuming that y and x displacements are very small relative to the dimensions of the mechanism, the equation of motion of the mechanism is calculated as [3, 55]

$$\left(\frac{m_a(cot^2(\theta)+1)}{4}+m\right)\ddot{x}+kx=\left(\frac{m_a(cot^2(\theta)-1)}{4}\right)\ddot{y}+ky. \tag{2.1}$$

The resonance frequency of the mechanism is calculated as

$$\omega_p = \sqrt{\frac{k}{m + \frac{m_a(cot^2(\theta)+1)}{4}}} \tag{2.2}$$

and the antiresonance frequency of the mechanism is calculated as

$$\omega_z = \sqrt{\frac{k}{\frac{m_a(cot^2(\theta)-1)}{4}}}. \tag{2.3}$$

When these equations are examined, it can be seen that the numerators of both resonance and antiresonance frequencies are the same, while the denominator of the resonance frequency is always greater than the denominator of the antiresonance frequency. Therefore, the resonance frequency of the mechanism is always smaller than the antiresonance frequency. These types of systems are low pass filter type of vibration isolation systems [3, 74].

In order to explain the width and depth of a stop band, a two degrees of freedom inertial amplification model with two resonance frequencies, ω_{p1} and ω_{p2}, and two antiresonance frequencies, ω_{z1} and ω_{z2}, can be analyzed. The frequency response function of this model can be found as the ratio of the output displacement to input displacement, or equivalently the ratio of the output acceleration to input acceleration. With the excitation frequency, ω, it can be calculated as [2]

$$H(\omega) = \left| \frac{\left(1 - \frac{\omega^2}{\omega_{z1}^2}\right)\left(1 - \frac{\omega^2}{\omega_{z2}^2}\right)}{\left(1 - \frac{\omega^2}{\omega_{p1}^2}\right)\left(1 - \frac{\omega^2}{\omega_{p2}^2}\right)} \right|. \tag{2.4}$$

In Figure 2.2, the frequency response function can be obtained with $\omega_{p1} = 3$, $\omega_{p2} = 23$, $\omega_{z1} = 10$, $\omega_{z2} = 23$ for the red solid curve. As, $\omega_{p2} = \omega_{z2}$, they cancel each other and the system behaves as if it is single degree of freedom with resonance frequency ω_{p1} and antiresonance frequency ω_{z1}. In order to have a system with two

degrees of freedom, ω_{p2} and ω_{z2} should be unequal. The green dashed curve shows the frequency response for $\omega_{p1} = 3$, $\omega_{p2} = 23$, $\omega_{z1} = 10$, $\omega_{z2} = 22.9$. The width and depth of the vibration isolation frequency band are shown in Figure 2.2.

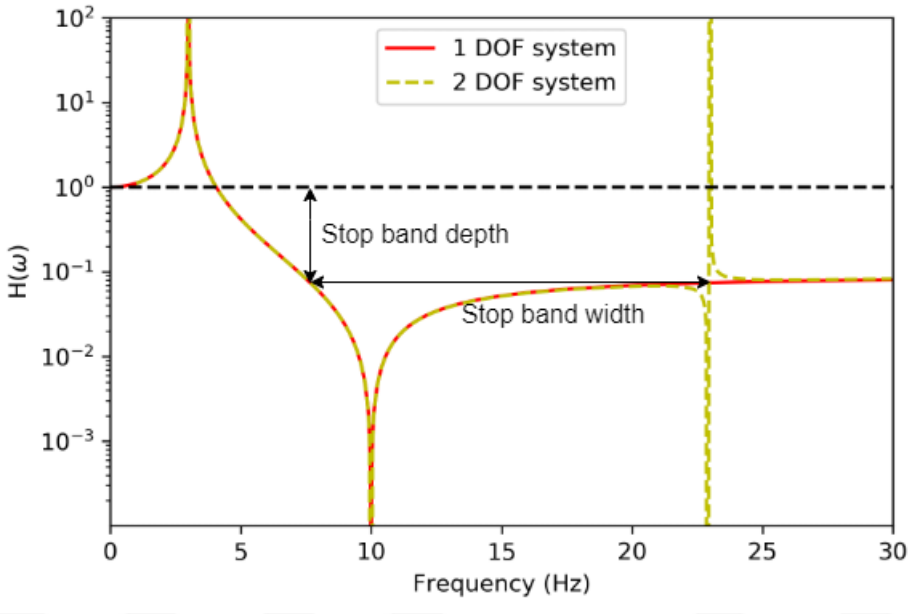


Figure 2.2. Frequency response function plot showing the width and depth of the stop band for a two degrees of freedom system. Green dashed curve is for $\omega_{p1} = 3$, $\omega_{p2} = 23$, $\omega_{z1} = 10$, $\omega_{z2} = 22.9$. Red solid curve is for $\omega_{p1} = 3$, $\omega_{p2} = 23$, $\omega_{z1} = 10$, $\omega_{z2} = 23$.

The stop band is defined as the interval in which $H(\omega)$ is lower than 1 [3]. In Equation 2.2, the mass m_a is multiplied by $\frac{cot^2(\theta)+1}{4}$ making it more effective. To obtain a high effective inertia, the θ angle is chosen small. In this way, a small mass of m_a affects the system as a mass much higher than its static value and reduces ω_p with the effect of the angle θ. Thus, the mechanism provides vibration isolation at low frequencies and this model shows the effect of the mass m_a in the middle of the mechanism on the reduction of the lower limit of the stop band. While the upper limit of the stop band can go to infinity for the lumped parameter single degree of freedom model as shown by the red dashed curve in Figure 2.2, there will be an upper limit for distributed parameter models that will be used in the next section. Hence, the stop

band will look like the green dashed curve in Figure 2.2, and to maximize bandwidth the lower limit should be minimized while the upper limit needs to be maximized.

3. 3D ULTRAWIDE INERTIAL AMPLIFICATION MECHANISM DESIGN

The basic principle of the inertial amplification mechanisms in the literature is to provide vibration isolation at low frequencies by increasing the effective inertia of the system without the need to reduce the stiffness. In Figure 3.1, the distributed parameter model of the inertial amplification mechanism examined in [2] is shown.

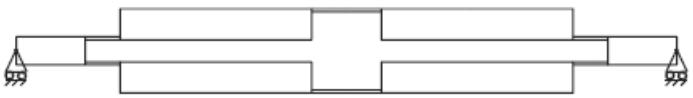
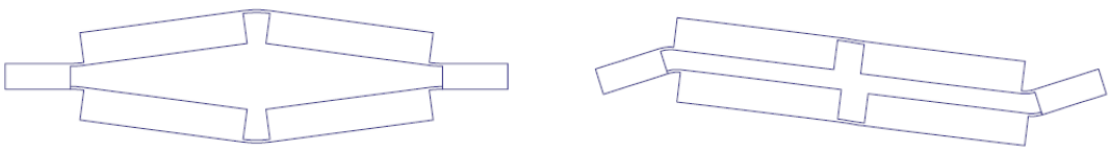


Figure 3.1. Inertial amplification mechanism in [2].

The first two mode shapes of the mechanism are shown in Figure 3.2. The first natural frequency of the mechanism is 279.2 Hz and the second natural frequency is 651.9 Hz obtained from the 1D finite element analysis result [2].



(a) (b)

Figure 3.2. Mode shapes of the mechanism shown in Figure 3.1. (a) First mode shape of the mechanism at 279.2 Hz. (b) Second mode shape of the mechanism at 651.9 Hz [2].

By periodically assembling these mechanisms in two dimensions, the structure shown in Figure 3.3 is obtained. Frequency response function graph of this structure obtained from 2D finite element model is given in Figure 3.4. In this graph, the lower

and upper limits of the stop band are 285 Hz and 617 Hz, and they are close to the first and second natural frequencies of a single inertial amplification mechanism. Therefore, when the difference between the natural frequencies of the first two modes are increased, a wider stop band can be obtained. For the structure in Figure 3.3, the frequency ratio of the upper limit to the lower one is around 2.16 [2].

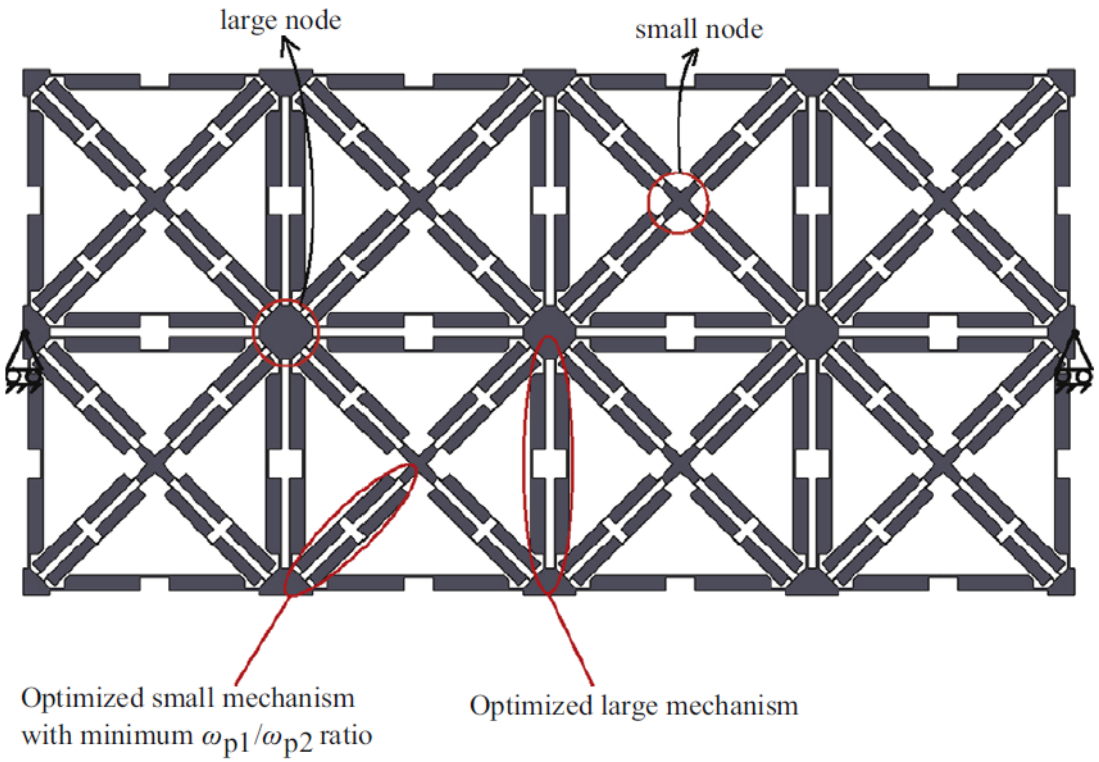


Figure 3.3. 2D periodic structure in [2].

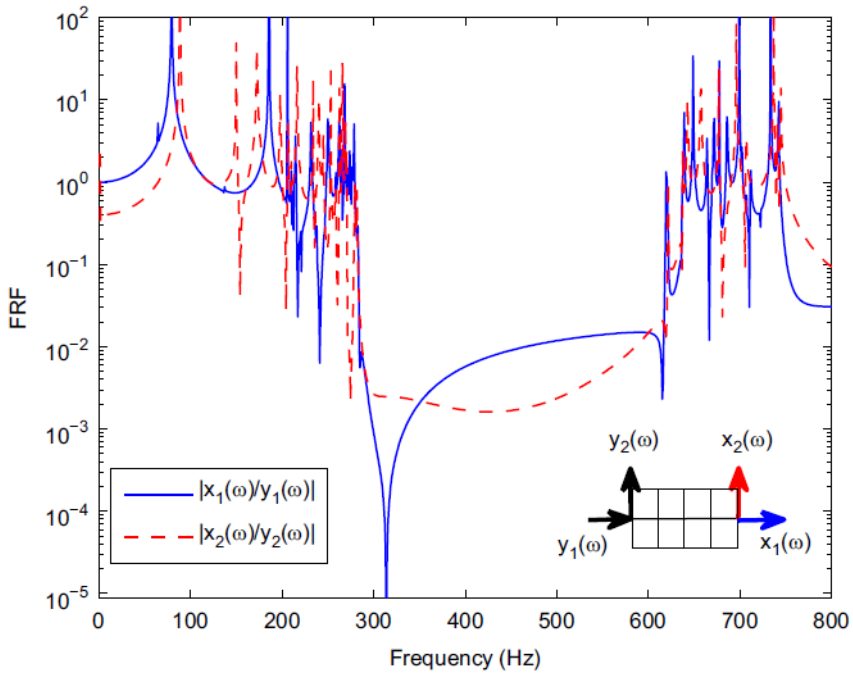


Figure 3.4. Frequency response function graph of the structure shown in Figure 3.3 [2].

By performing size and shape optimization on this mechanism, and assembling them in two dimensions as in Figure 3.5, a wider stop band is obtained between 265 Hz and 830 Hz, giving a frequency ratio of 3.13 [3].

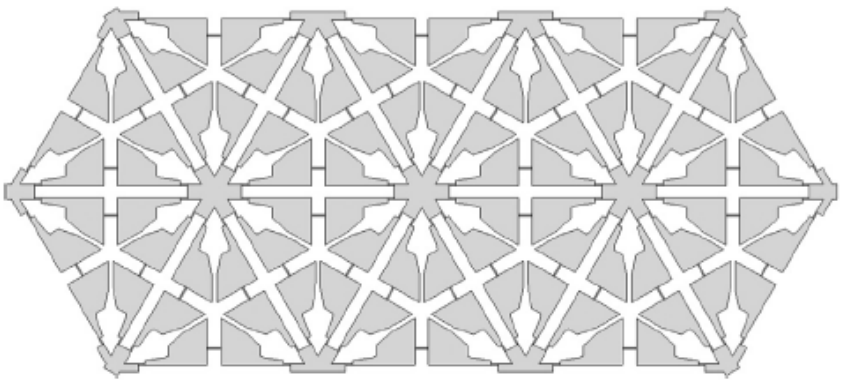


Figure 3.5. 2D periodic structure with the shape optimized inertial amplification mechanisms in [3].

In [1], the end connections of the mechanisms are redesigned and the mechanism is topologically optimized. At the end, the 2D periodic structure shown in Figure 3.6 is obtained. It provides a stop band between 29 Hz and 590 Hz, resulting in a frequency ratio of 20.3 [1].

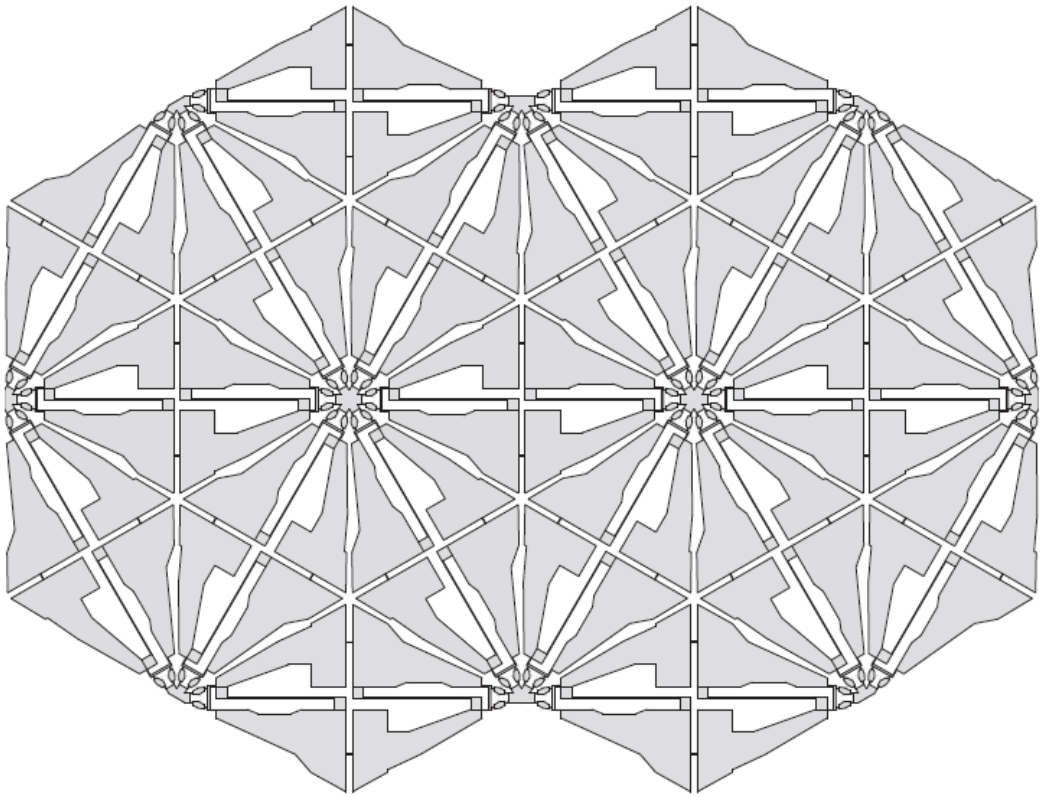


Figure 3.6. 2D periodic structure with remote center flexure mechanisms at the end connections and topologically optimized mechanisms in [1].

In this study, a 3D periodic structure will be designed with inertial amplification mechanisms and the stop band of this structure will be maximized. In order to do that, inertial amplification mechanisms should have appropriate end connections to be assembled in three dimensions.

3.1. Design of End Connections

Connecting inertial amplification mechanisms periodically in one, two, or three dimensions is a crucial concept to obtain a wide vibration isolation frequency band, since it has a direct effect on the natural frequencies and mode shapes of the mechanisms.

Figure 3.7 shows the inertial amplification mechanism generating an ultra wide vibration isolation band in one dimension analyzed in [4] and Figure 3.8 shows the first three mode shapes of this mechanism and their corresponding natural frequencies. For this 1D system, vibration isolation can be achieved between the first two modes. The ratio of the upper limit of the vibration isolation frequency band to the lower one is 38.9 for an infinitely periodic array in one dimension [4]. In this mechanism design, the rectangular blocks at the ends do not rotate. Therefore, although a wide isolation frequency band in one dimension can be obtained with this mechanism, it cannot provide the same in two or three dimensions.

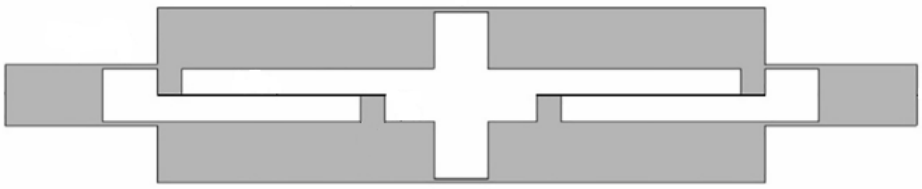


Figure 3.7. Inertial amplification mechanism in [4].

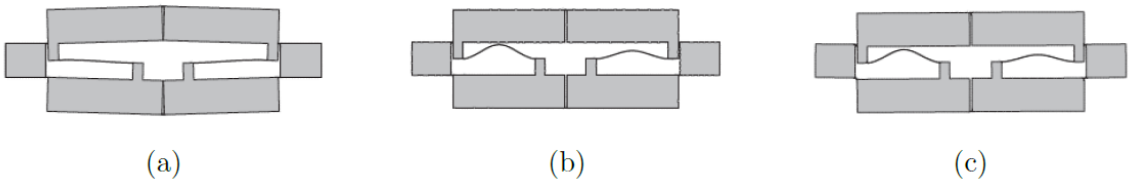


Figure 3.8. Mode shapes of the mechanism shown in Figure 3.7. (a) First mode shape of the mechanism at 6.9 Hz. (b) Second mode shape of the mechanism at 303.6 Hz, the bending mode of the long flexures in the middle. (c) Third mode shape of the mechanism at 373 Hz, vertical translation of the rectangular blocks at the ends [4].

The inertial amplification mechanism analyzed in [5] is shown in Figure 3.9. The four triangular blocks bring the center of gravity of the structure closer to the flexure hinges in the middle. Thus, it is aimed to decrease the first natural frequency by increasing the effective inertia of the system. The first three mode shapes of this mechanism are given in Figure 3.10.

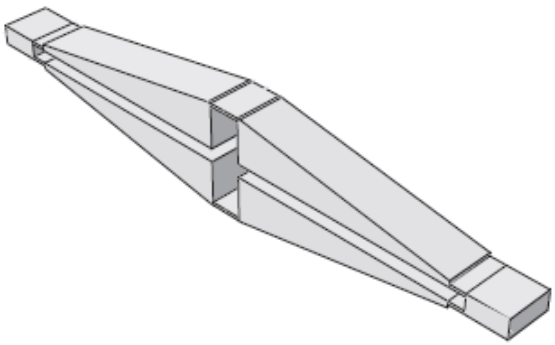


Figure 3.9. Inertial amplification mechanism in [5]

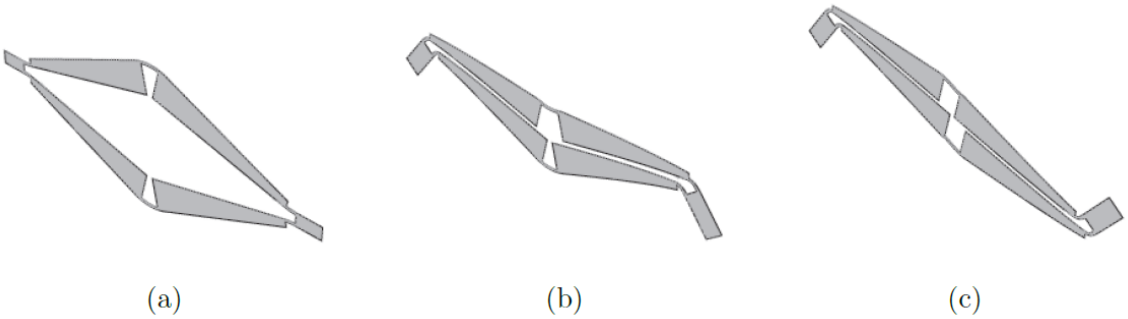


Figure 3.10. Mode shapes of the mechanism shown in Figure 3.9. (a) First mode shape of the mechanism at 49.6 Hz. (b) Second mode shape of the mechanism at 241.6 Hz. (c) Third mode shape of the mechanism at 248.2 Hz [4].

The octahedron structure built with this mechanism is shown in Figure 3.11. The stop band of this structure is between 64 and 267.2 Hz and the frequency ratio of the upper limit to the lower one is 4.18 [5]. Notice that this ratio is lower than the ratio of the second and first natural frequencies of the inertial amplification mechanism in Figure 3.10, which is 4.87.

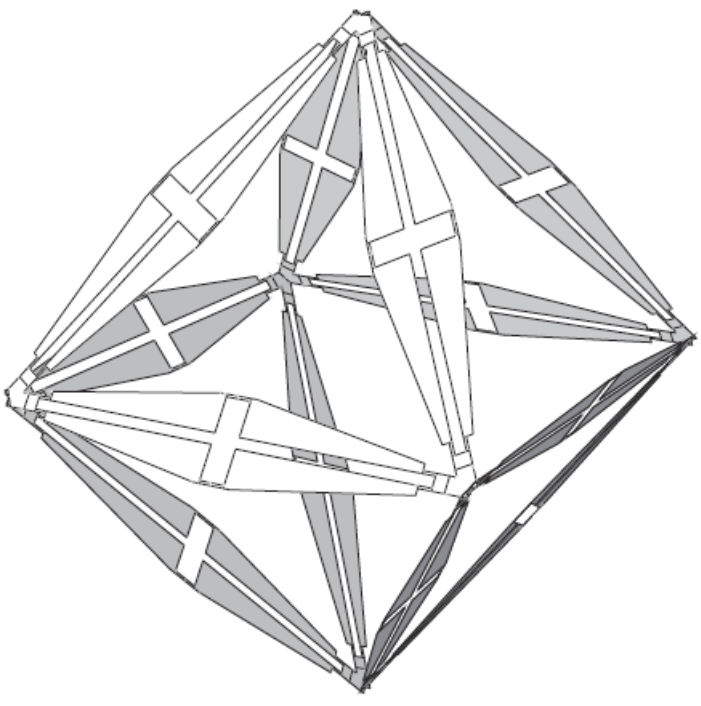
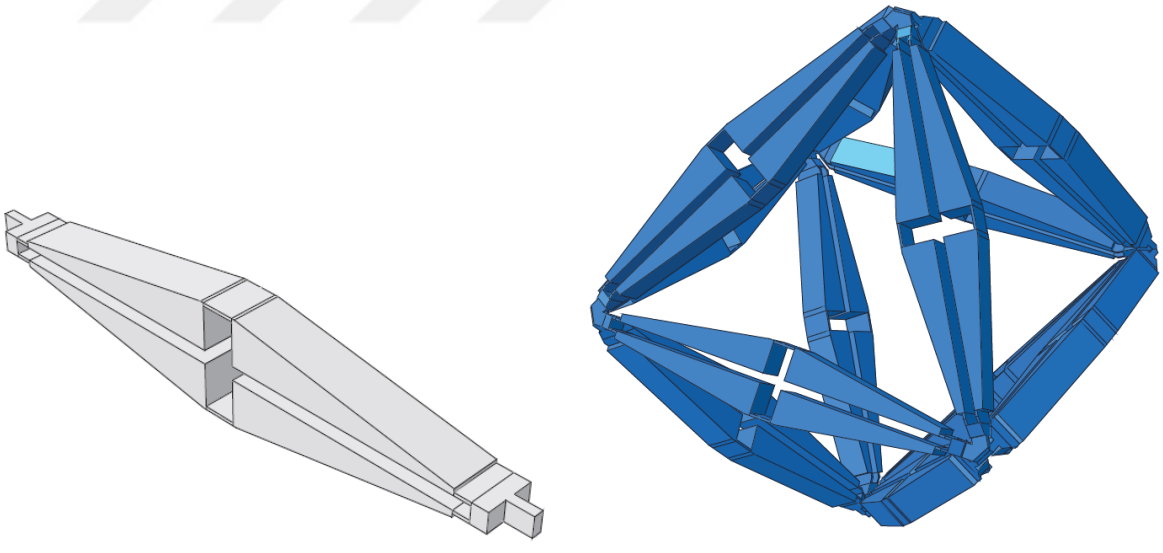


Figure 3.11. Octahedron structure built with the mechanism shown in Figure 3.9 [5].

In order to widen the stop band of the octahedron structure, the end connections of the inertial amplification mechanism in Figure 3.9 are modified as in Figure 3.12(a) [5]. Thin end connections can bend in a perpendicular direction compared to the neighboring flexure hinges. In this design, the thin end connections and flexure hinges allow the end of the mechanism to rotate in two orthogonal axes. When this mechanism is combined in three dimensions as shown in Figure 3.12(b), the ratio of the upper limit of the isolation frequency band to the lower limit is approximately 4.8 [5].

The bandwidth of structure in Figure 3.12(b) can be increased if the flexure hinge design is changed. In order to widen the stop band, the first natural frequency of the mechanism can be decreased by reducing the bending stiffness of the flexure hinges. However, this will also decrease the second natural frequency, resulting in a narrow stop band. Therefore, these flexures should not be allowed to rotate and a separate part should perform the rotation function.



(a) (b)

Figure 3.12. Building a 3D periodic structure with inertial amplification mechanisms having thin end connections. (a) Inertial amplification mechanism with thin end connections. (b) Octahedron structure formed with these mechanisms [5].

In Figure 3.13, a new end connection design is used, which involves a flexible four-bar mechanism model with a remote center of rotation [1]. As can be seen in Figure 3.14, the end connection of this mechanism act like a pin-roller type of connection in two dimensions. Using inertial amplification mechanisms with this type of an end connection, a vibration isolation band with a frequency ratio of 20.3 can be obtained in two dimensions [1]. In this thesis, this end connection idea is developed to be used in three dimensions.

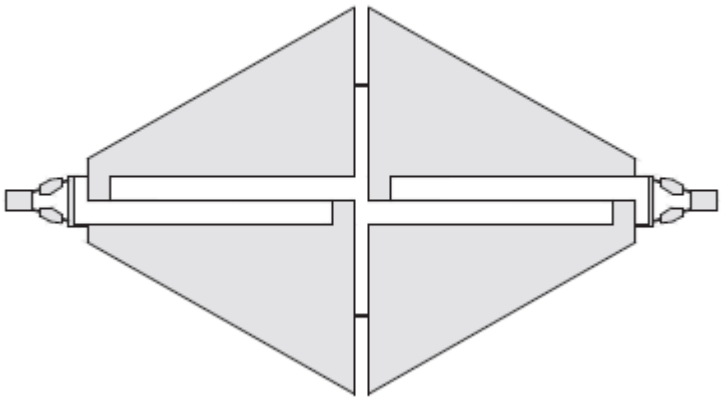


Figure 3.13. Inertial amplification mechanism in [1].

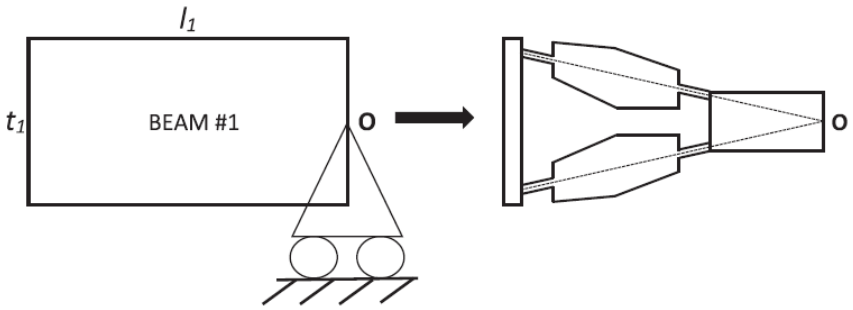


Figure 3.14. Pin-roller type of end connection designed in [1].

The remote center of rotation concept can be explained with a rigid four-bar mechanism. Figure 3.15 shows a planar four-bar mechanism. Assuming that the rectangular part (3) is fixed, it can be seen that the instantaneous center of rotation of the link (1) is point O.

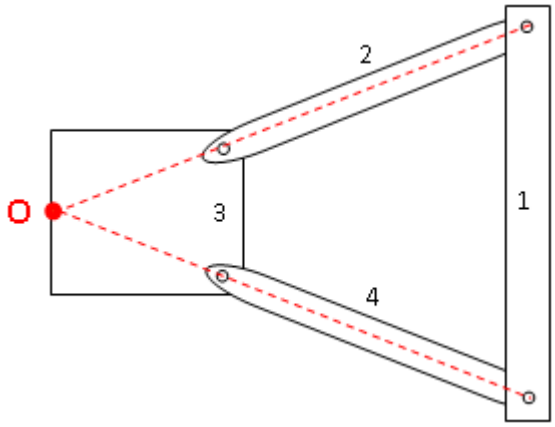


Figure 3.15. Four-bar mechanism with remote center of rotation for link (1) at point O, which is the intersection of the extensions of the rods (2) and (4).

Any structure added to link (1) will rotate around the point O. The flexure hinge design equivalent of the structure in Figure 3.15 is given in Figure 3.16. Instead of pin joints, thin sections acting as flexure hinges are used in order to eliminate the rattle, friction and wear problems. In this design, thick sections act like links.

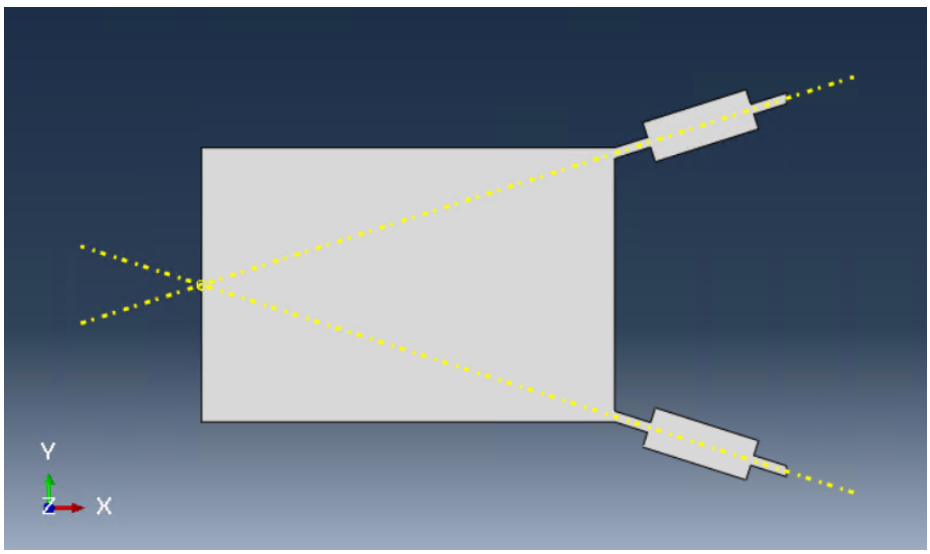


Figure 3.16. Planar flexure hinge mechanism with remote center of rotation at the intersection of the yellow dashed lines.

The flexure hinge mechanism in Figure 3.16 can be used in planar applications in which in-plane bending is possible. However, 3D structures can be subject to both

in-plane and out-of-plane bending loads. A new flexure hinge mechanism is designed which allows bending in two orthogonal axes while having the same remote center of rotation at point O as shown in Figure 3.17.

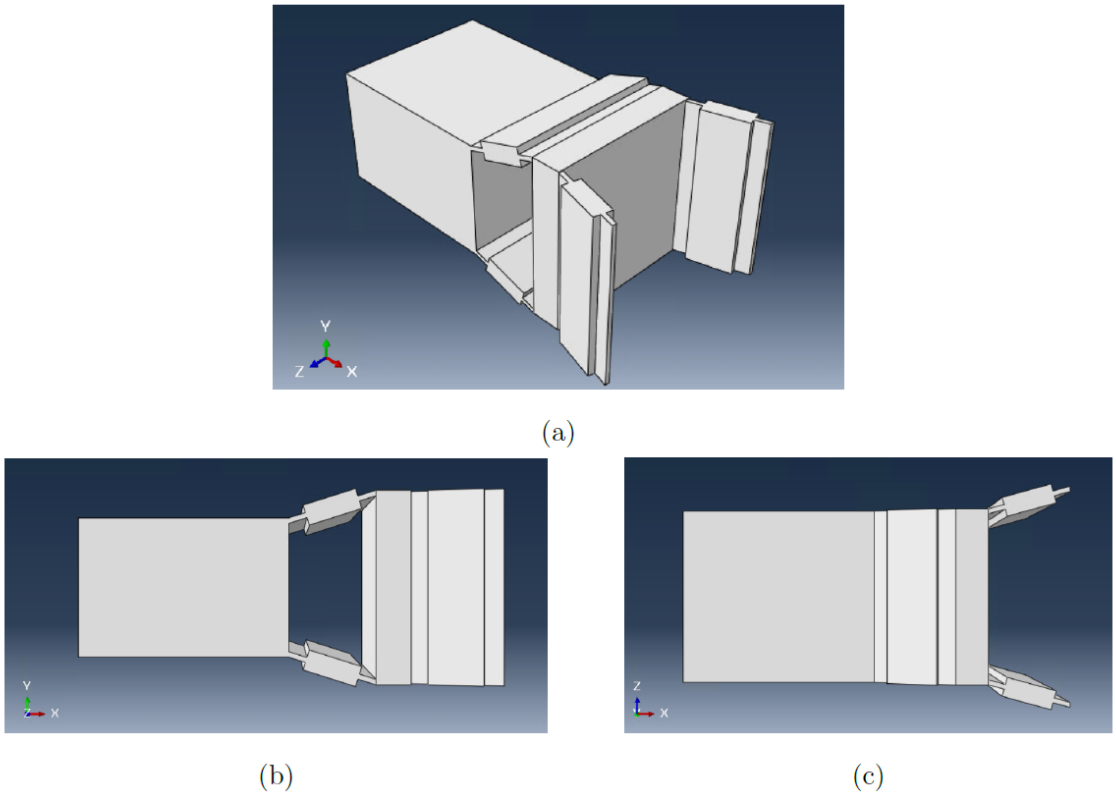


Figure 3.17. Spatial flexure hinge mechanism design that allows bending in two orthogonal axes. (a) Isometric view. (b) Side view in the x-y plane. (c) Top view in the x-z plane.

While the first stage of the structure moving in the x-y plane allows rotation around the z axis, the second stage connected in series moving in the x-z plane allows rotation around the y axis. There are two links with flexure hinges at both stages. The center of rotation of all of these links coincide at the center of the back surface of the rectangular prism to which they are attached. Figure 3.18 shows that the central lines of all four links intersect at the same point.

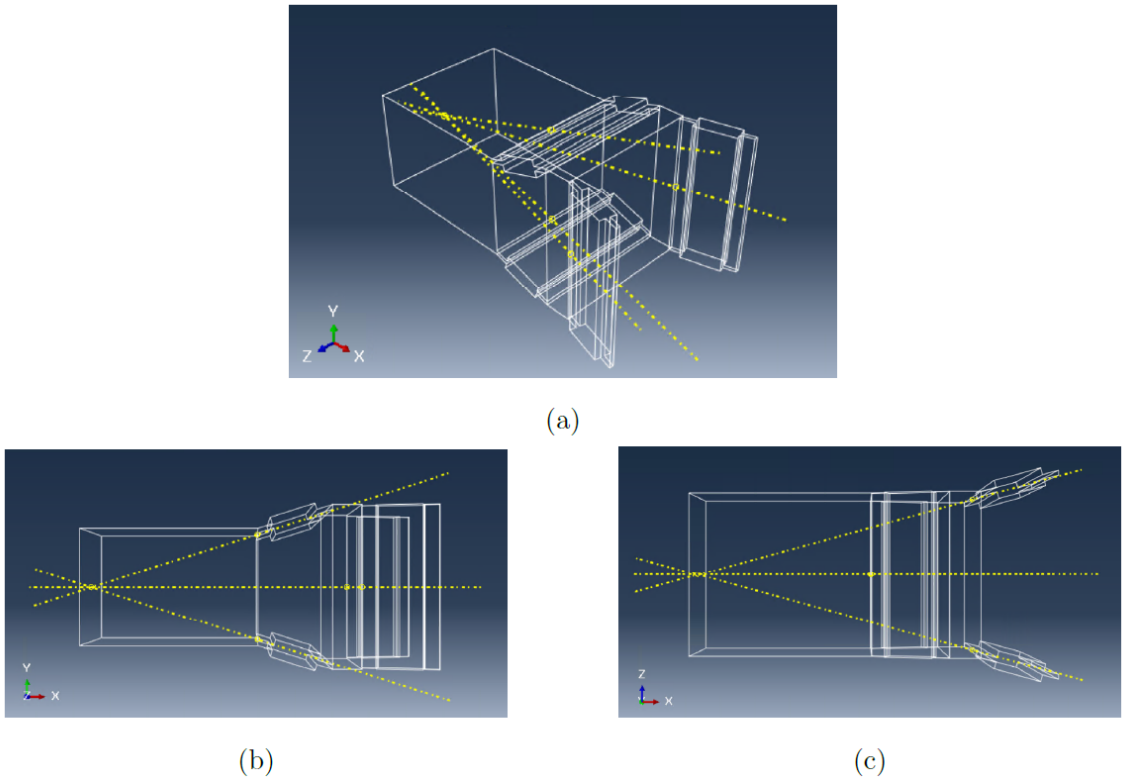


Figure 3.18. Instantaneous center of rotation of the spatial flexure hinge mechanism at the center of the back surface of the rectangular prism which is the intersection of the link extensions. (a) Isometric view. (b) Side view in the x-y plane. (c) Top view in the x-z plane.

3.2. Design of the Inertial Amplification Mechanism

The finite element analysis software Abaqus is used to design and analyze the mechanisms. Firstly, the 2D design in Figure 3.13 is modified as in Figure 3.19 in order to obtain a band gap in three dimensions. Although the mechanism in Figure 3.13 provides the widest band gap in two dimensions, it only moves in-plane and the out-of-plane and torsional modes are not taken into account. Since these modes should also be considered in 3D inertial amplification mechanism design, the bandwidth in this study should not be expected as wide as in [1]. In Figure 3.20, the alignment of the parts in the inertial amplification mechanism is shown. The yellow dashed lines pass through the center of the back surface of the rectangular block at the end of

the mechanism, the flexure hinge connected to this rectangular block, the center of the horizontal flexure between the remote center flexure mechanism and the triangular blocks, and the center of the short flexure in the middle of the mechanism. The remote center flexure mechanisms are added to the mechanism by keeping the total length same as in [1], and they are connected to the middle triangular blocks with horizontal flexures. As in [1], the thinnest parts of the initial design are 0.3 mm. The center of mass of the triangular blocks are close to the middle of the mechanism where displacement amplification is large for axial motions. These blocks can be optimized topologically as in [1]. However, the main aim in this study is to optimize the flexure hinges in the mechanism. So, different flexure hinge configurations are compared and the size optimization is done for the best configuration.

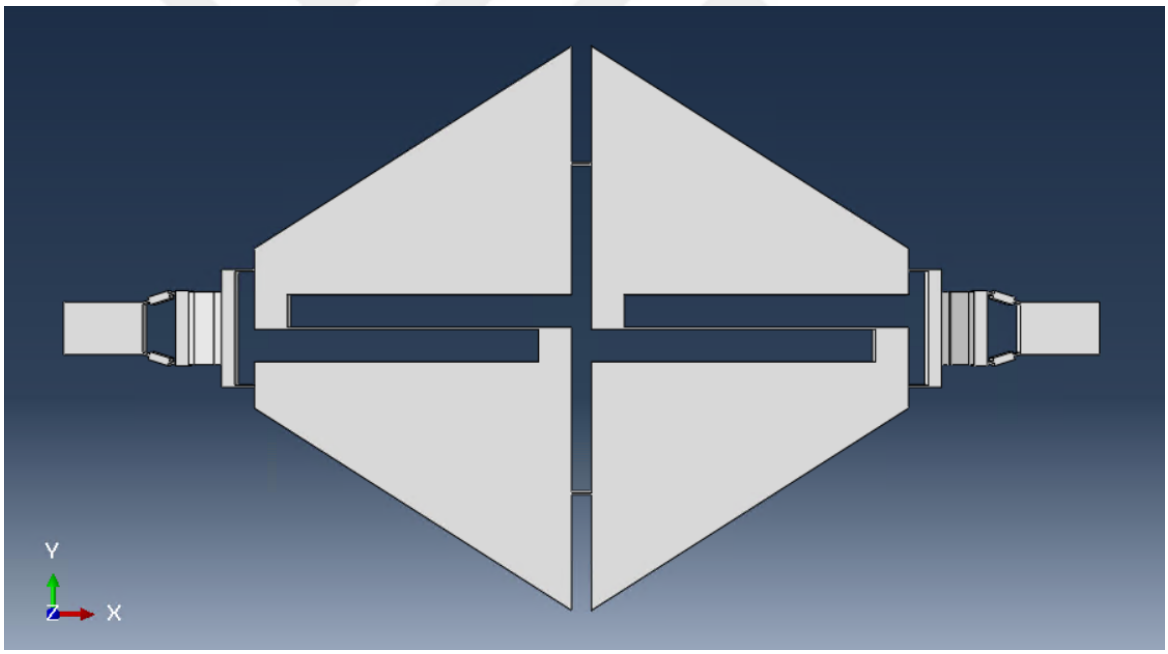
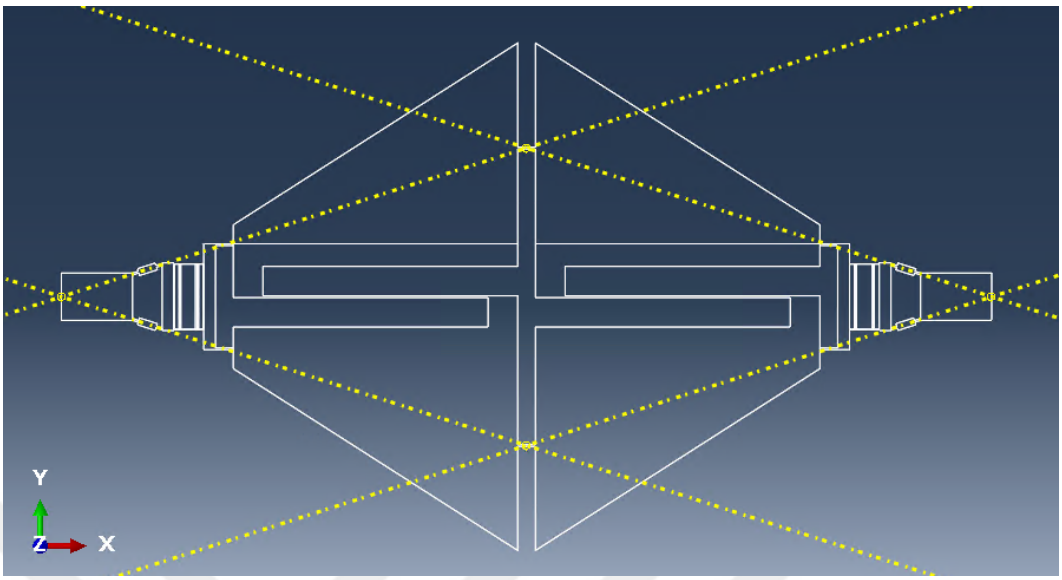
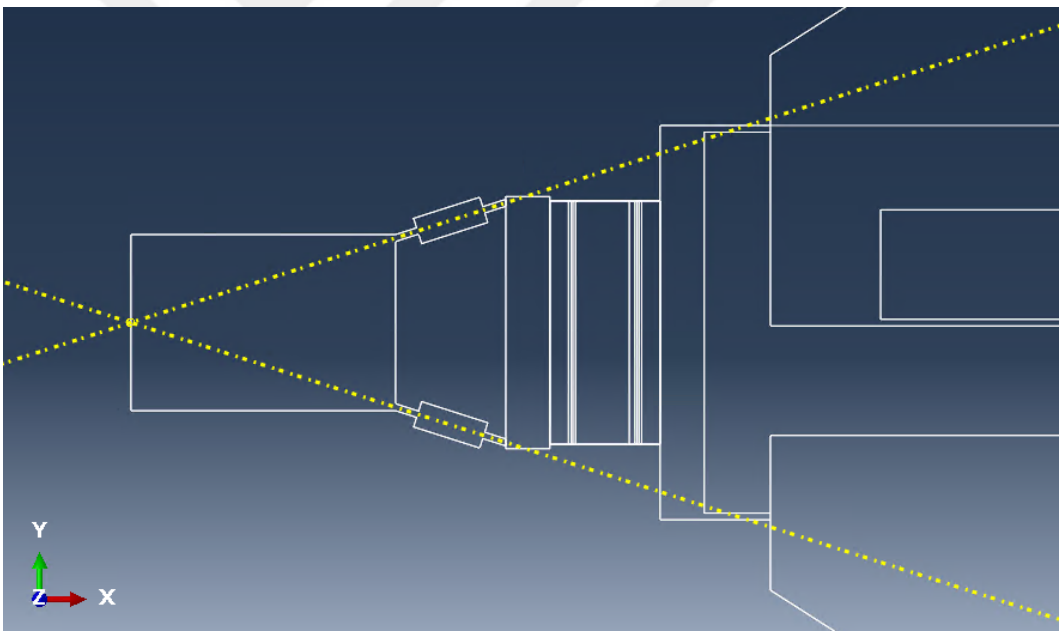


Figure 3.19. Initial design of the mechanism.



(a)

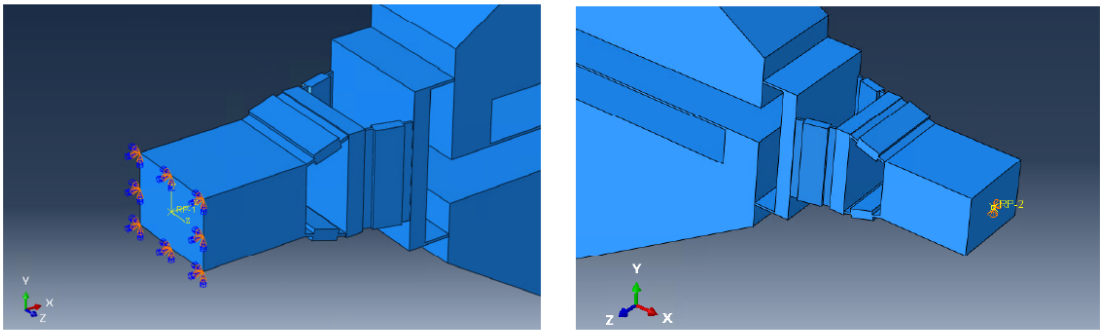


(b)

Figure 3.20. Alignment of the inertial amplification mechanism. (a) Side view of the mechanism in the x-y plane. (b) Close up view of the end of the mechanism.

In order to identify the mode shapes of the inertial amplification mechanism in Figure 3.19, different boundary conditions are imposed. First, the left end of the mechanism is clamped and pin-roller type of boundary condition is imposed to the other end as shown in Figure 3.21. The first ten mode shapes are given in Figures

3.22-3.31, and corresponding natural frequencies are given in Table 3.1.



(a) (b)

Figure 3.21. Clamped-pin roller boundary condition for the initial design of the mechanism. (a) Boundary condition at the left end. The back surface of the rectangular prism of the left end is clamped, i.e., it cannot translate or rotate in any directions. (b) Boundary condition at the right end. The front surface of the rectangular prism of the right end is coupled with the reference point RP-2, and the translations in y- and z-axes of this point are prevented but all the other degree of freedoms are free.

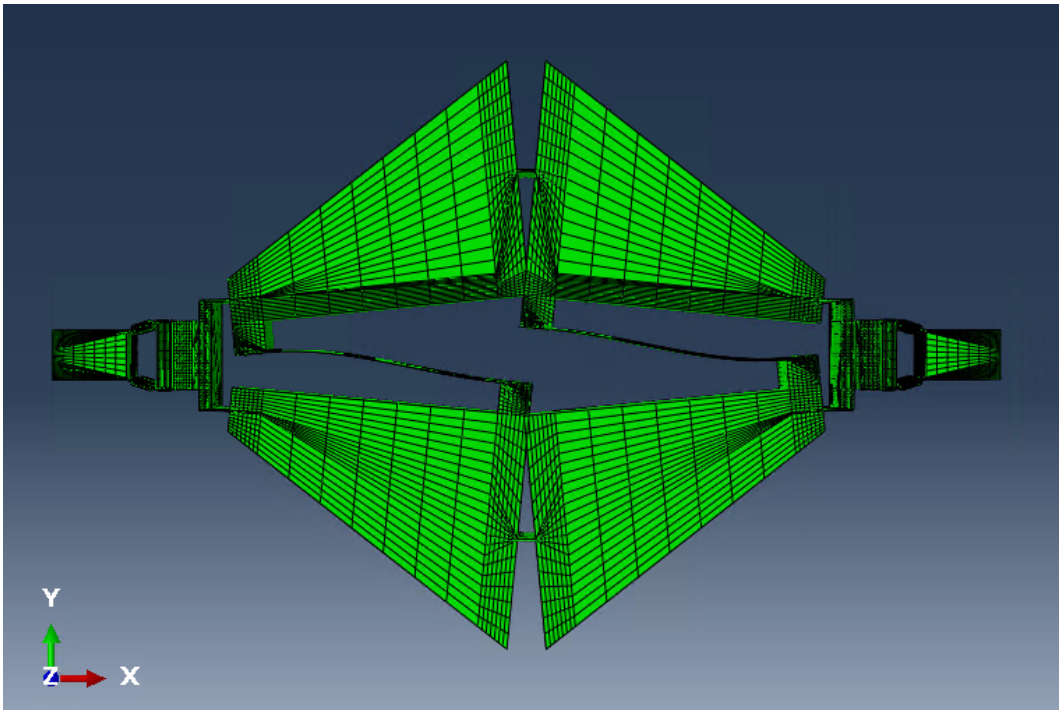


Figure 3.22. First mode shape of the mechanism imposed to clamped-pin roller boundary condition at 33.73 Hz.

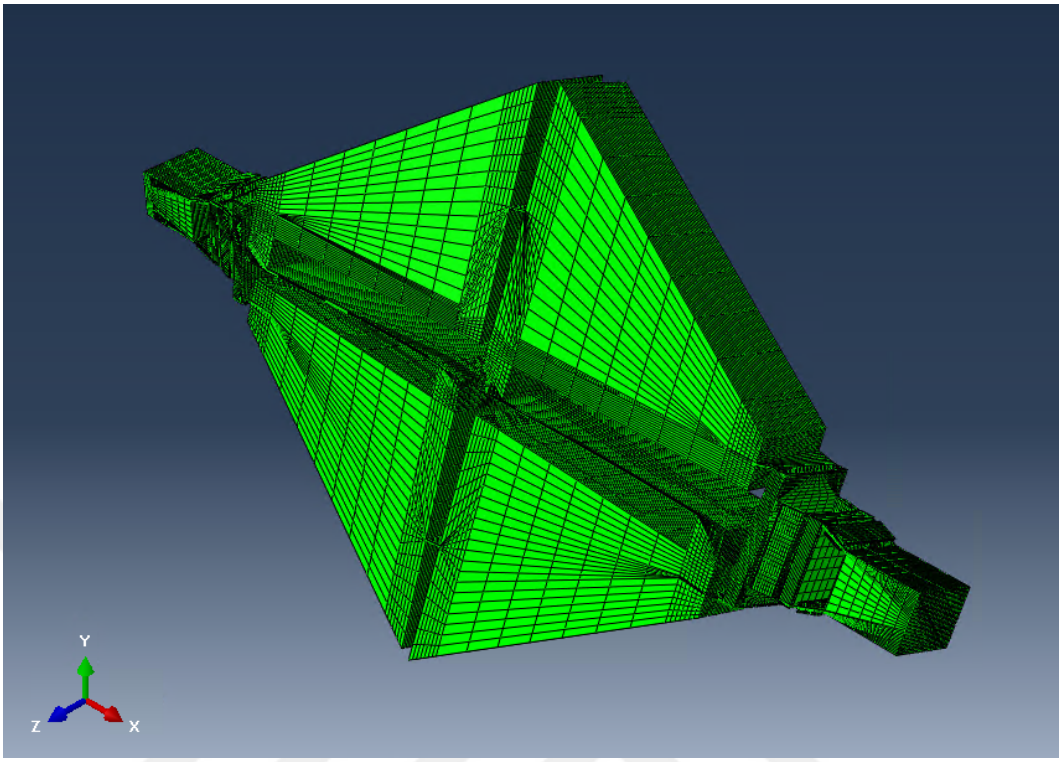


Figure 3.23. Second mode shape of the mechanism imposed to clamped-pin roller boundary condition at 177.9 Hz.

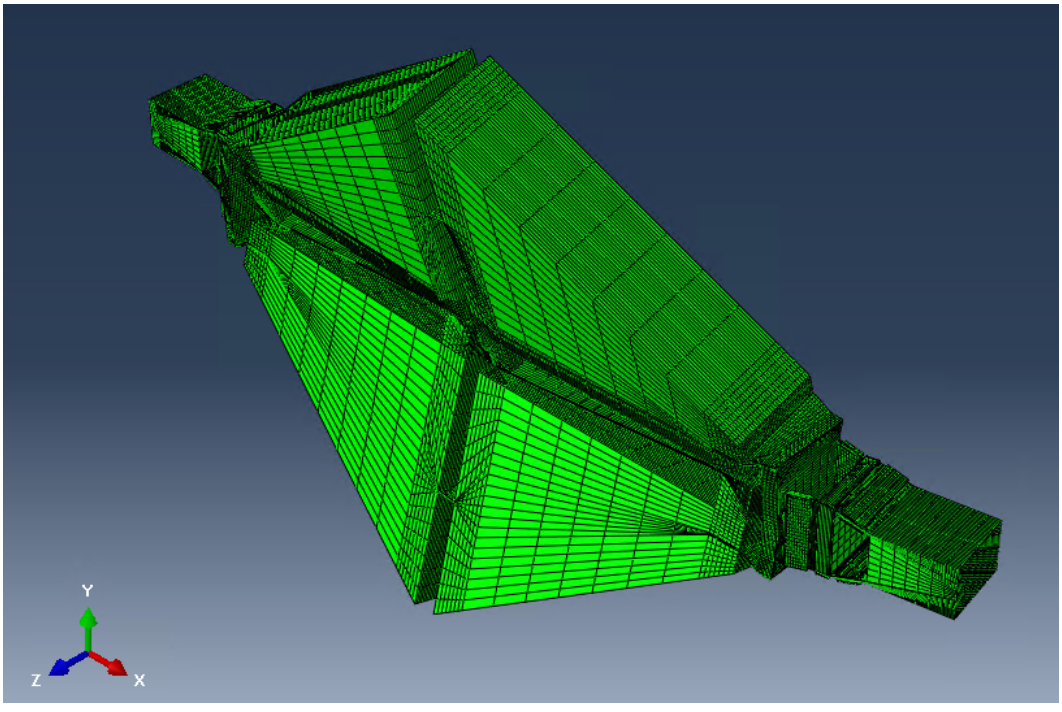


Figure 3.24. Third mode shape of the mechanism imposed to clamped-pin roller boundary condition at 283.3 Hz.

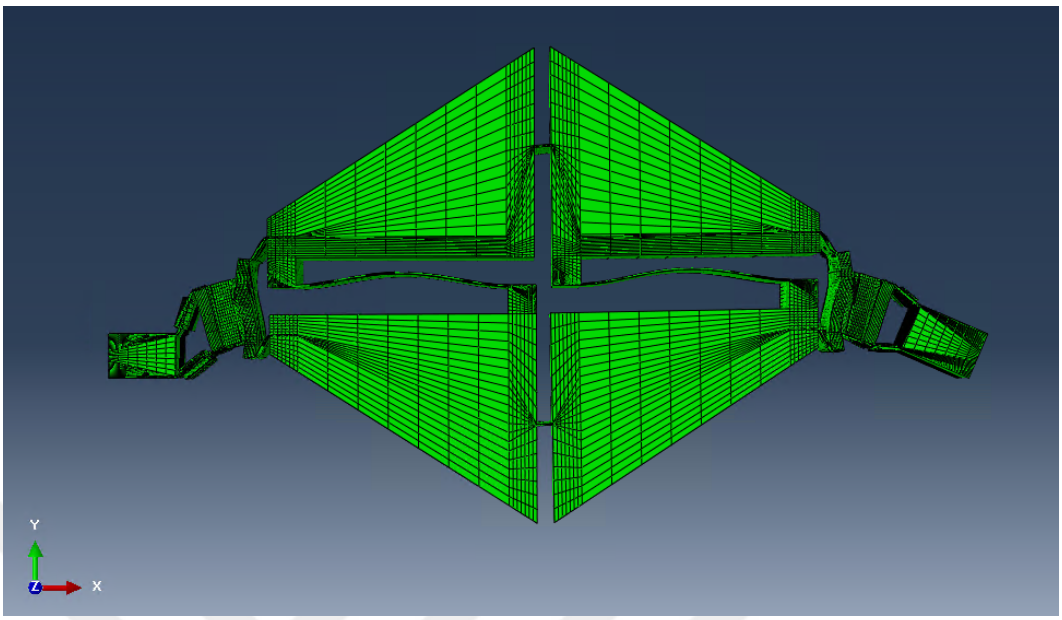


Figure 3.25. Fourth mode shape of the mechanism imposed to clamped-pin roller boundary condition at 390.7 Hz.

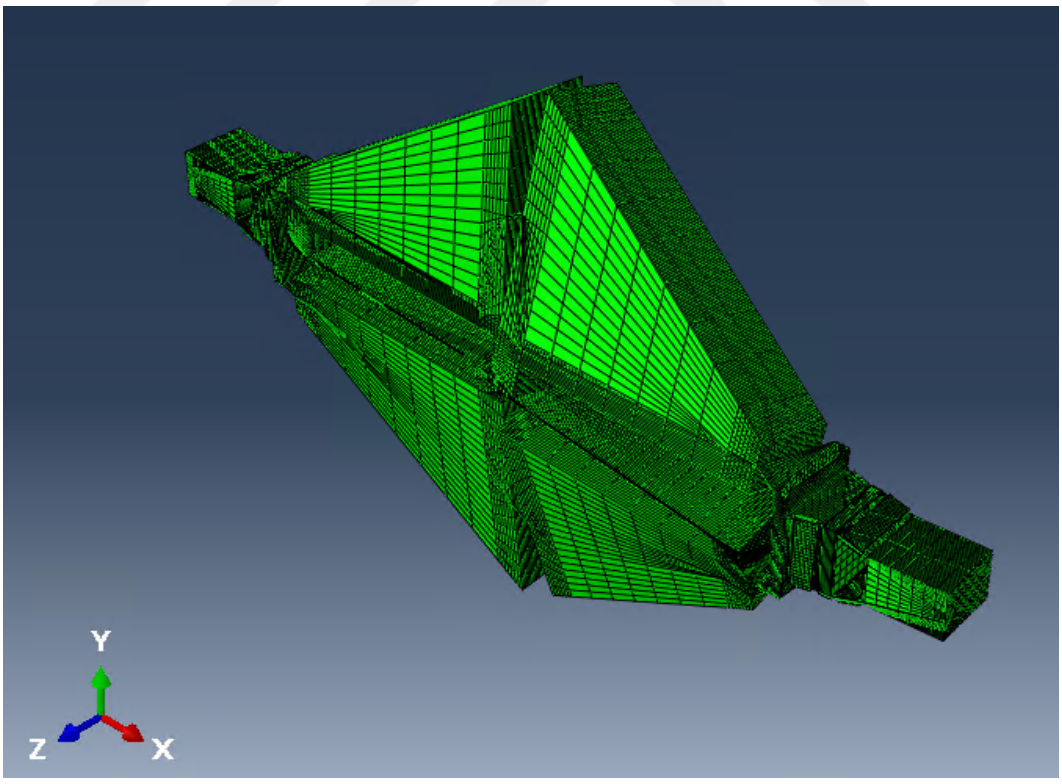


Figure 3.26. Fifth mode shape of the mechanism imposed to clamped-pin roller boundary condition at 673.0 Hz.

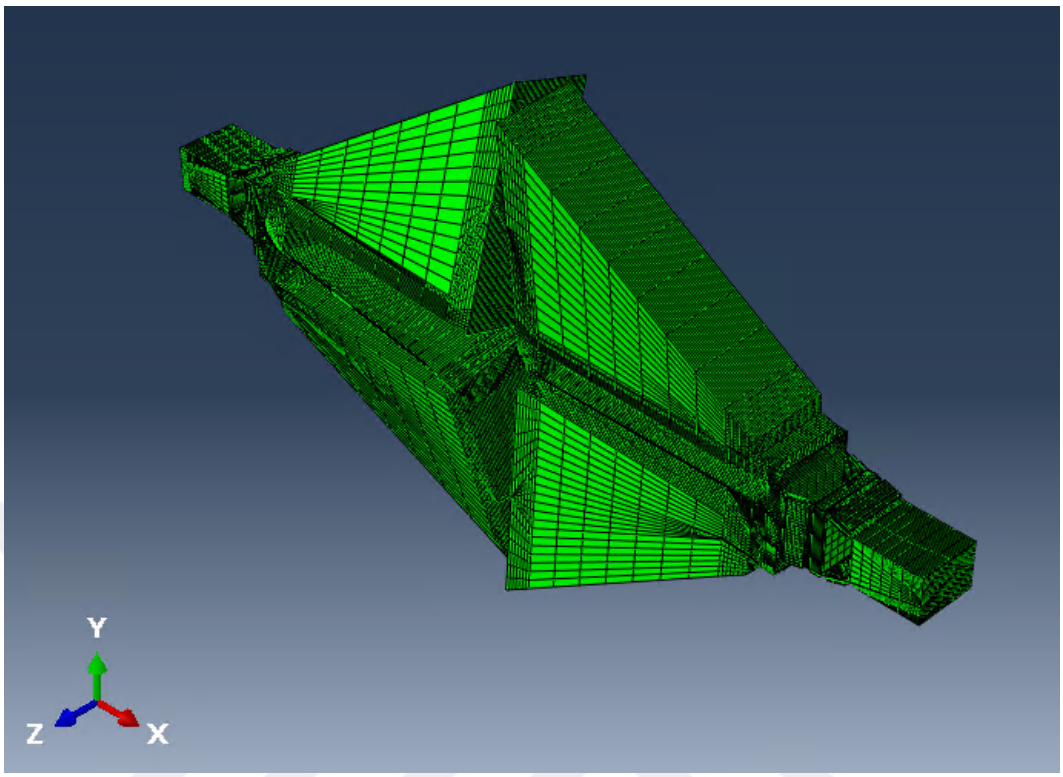


Figure 3.27. Sixth mode shape of the mechanism imposed to clamped-pin roller boundary condition at 720.3 Hz.

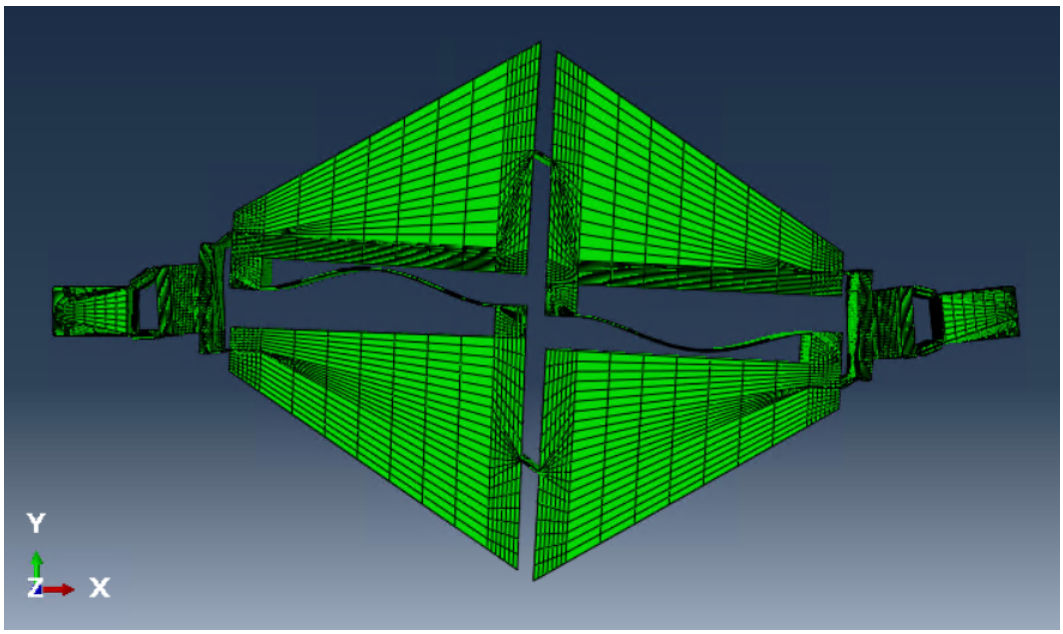


Figure 3.28. Seventh mode shape of the mechanism imposed to clamped-pin roller boundary condition at 876.6 Hz.

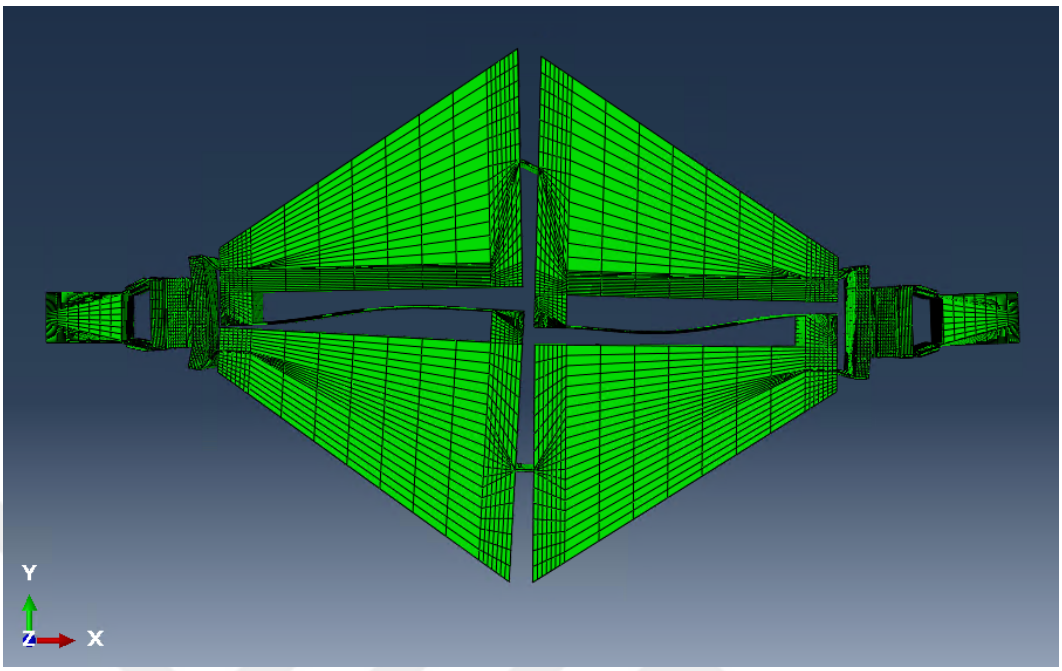


Figure 3.29. Eighth mode shape of the mechanism imposed to clamped-pin roller boundary condition at 901.7 Hz.

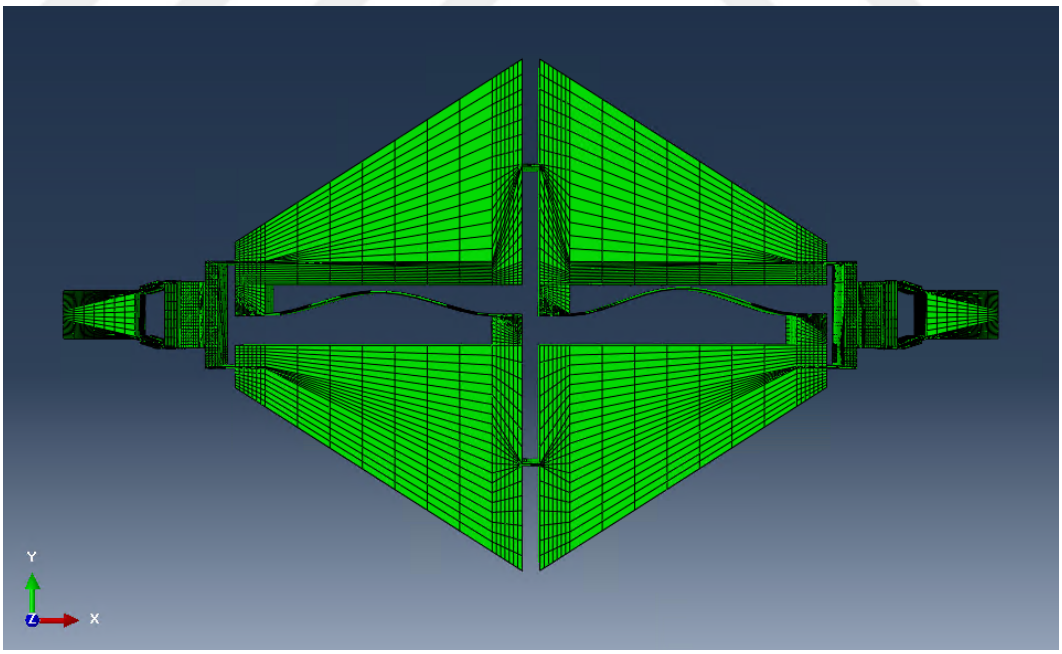


Figure 3.30. Ninth mode shape of the mechanism imposed to clamped-pin roller boundary condition at 1118 Hz.

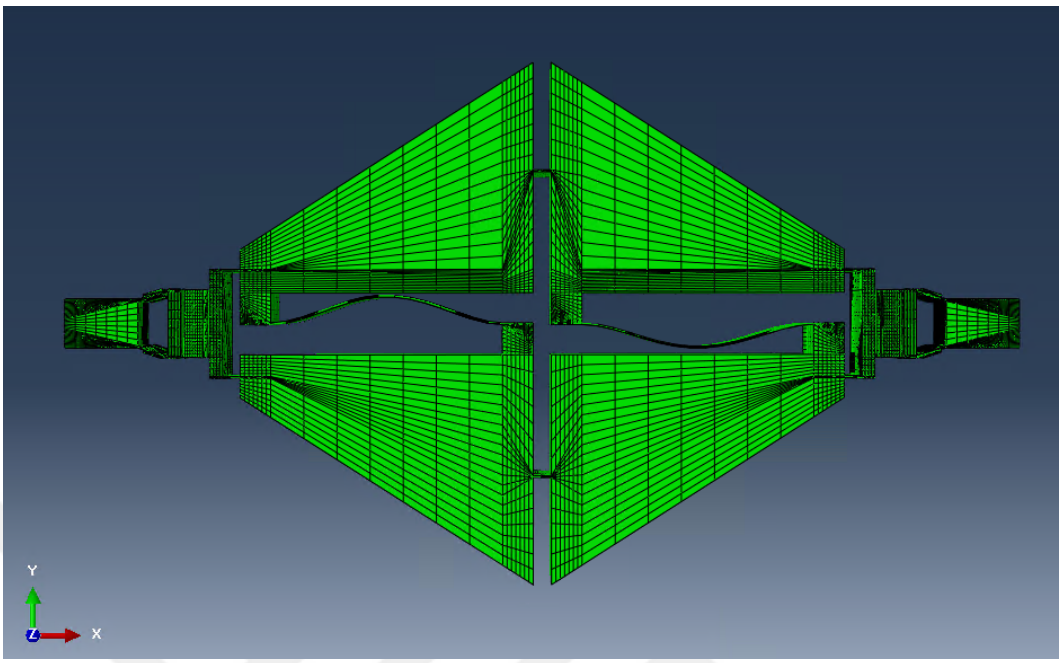
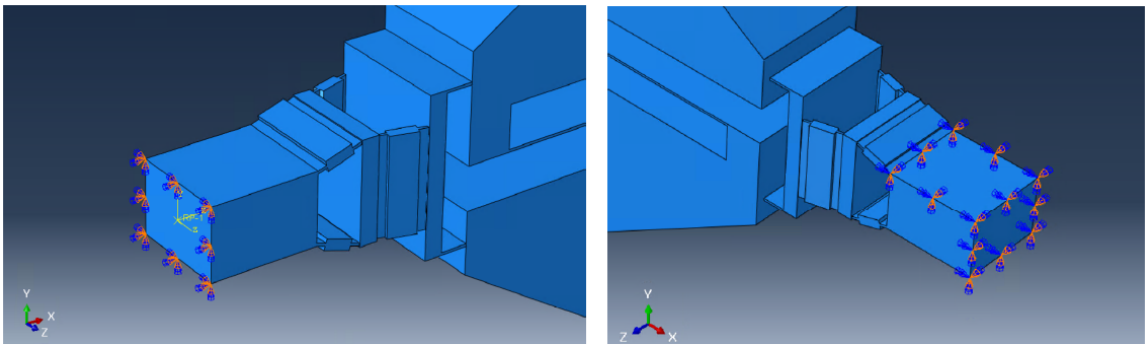


Figure 3.31. Tenth mode shape of the mechanism imposed to clamped-pin roller boundary condition at 1121 Hz.

Table 3.1. First ten natural frequencies of the mechanism shown in Figure 3.19 imposed to clamped-pin roller boundary condition.

Natural frequencies	Frequency (Hz)
ω_1	33.73
ω_2	177.9
ω_3	283.3
ω_4	390.7
ω_5	673.0
ω_6	720.3
ω_7	876.6
ω_8	901.7
ω_9	1118
ω_{10}	1121

When clamped-roller boundary condition is imposed to the inertial amplification mechanism as shown in Figure 3.32, the resulting first ten mode shapes are calculated and given in Figures 3.33-3.42 and corresponding natural frequencies are given in Table 3.2.



(a) (b)

Figure 3.32. Clamped-roller boundary condition for the initial design of the mechanism. (a) Boundary condition at the left end. The back surface of the rectangular prism of the left end is clamped, i.e., it cannot translate or rotate in any directions. (b) Boundary condition at the right end. Only the translation in x-axis of the side and top surfaces of the rectangular prism of the right end is allowed.

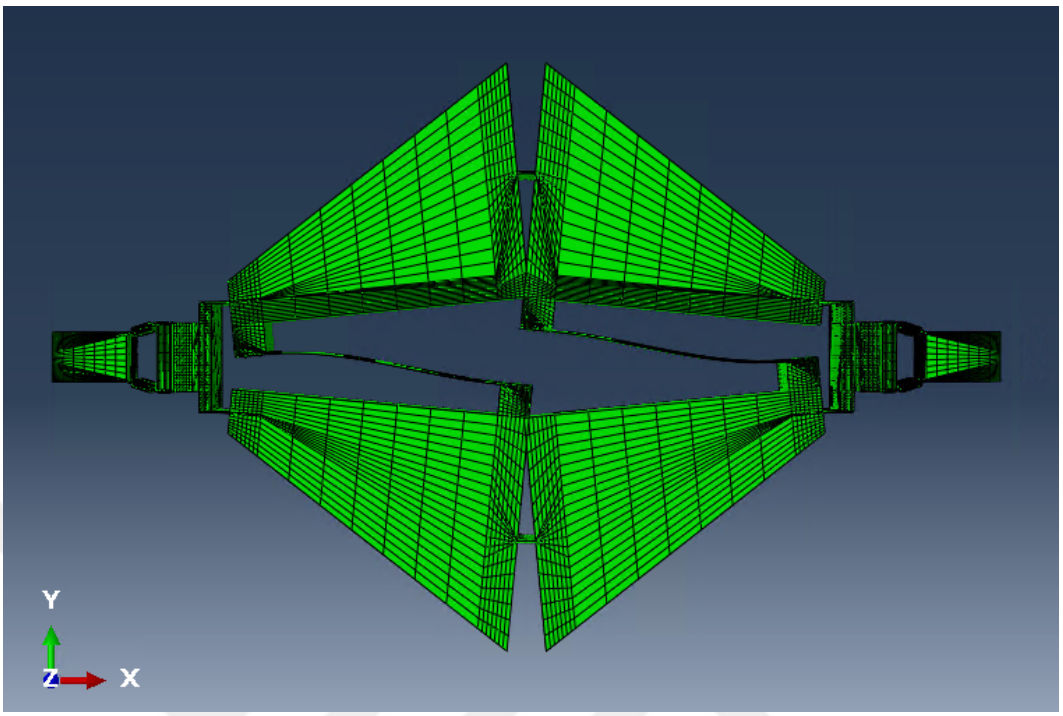


Figure 3.33. First mode shape of the mechanism imposed to clamped-roller boundary condition at 33.73 Hz.

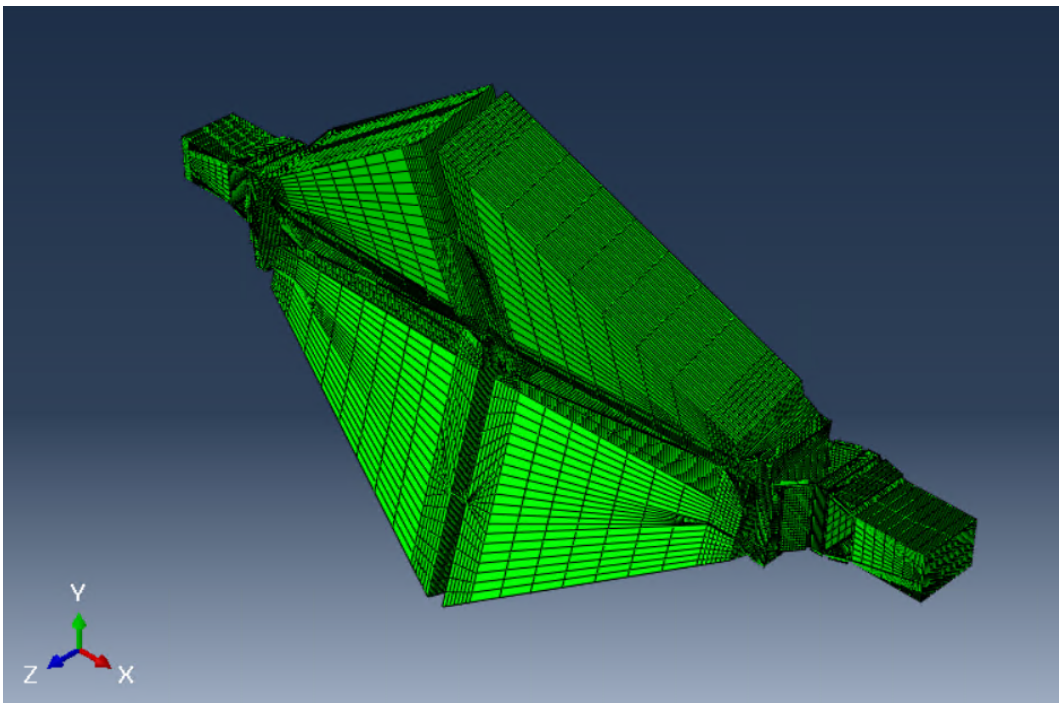


Figure 3.34. Second mode shape of the mechanism imposed to clamped-roller boundary condition at 300.9 Hz.

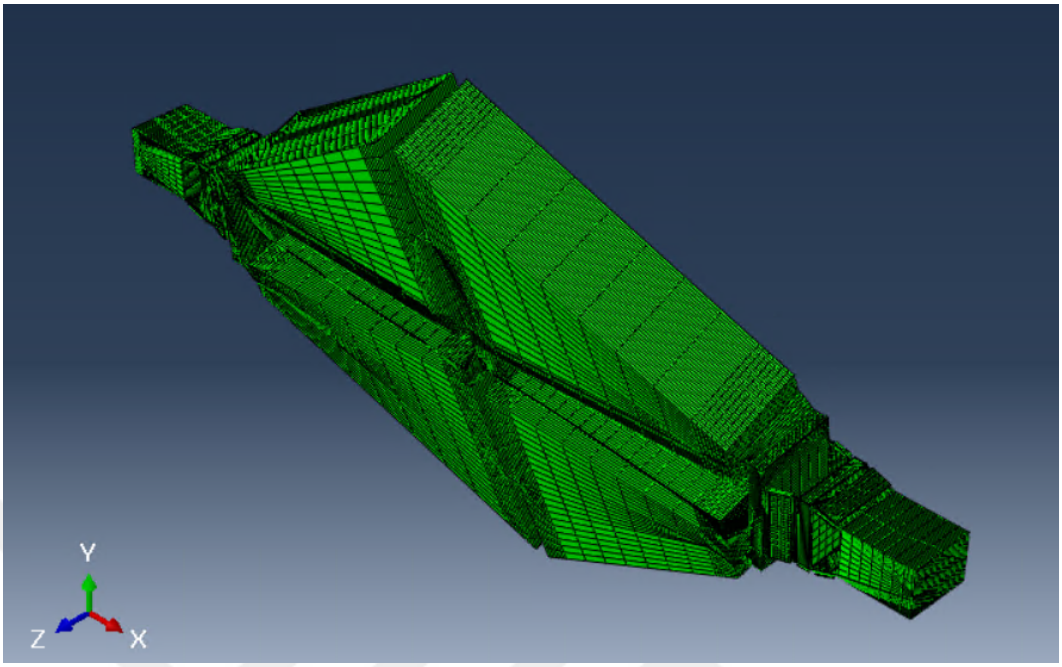


Figure 3.35. Third mode shape of the mechanism imposed to clamped-roller boundary condition at 334.8 Hz.

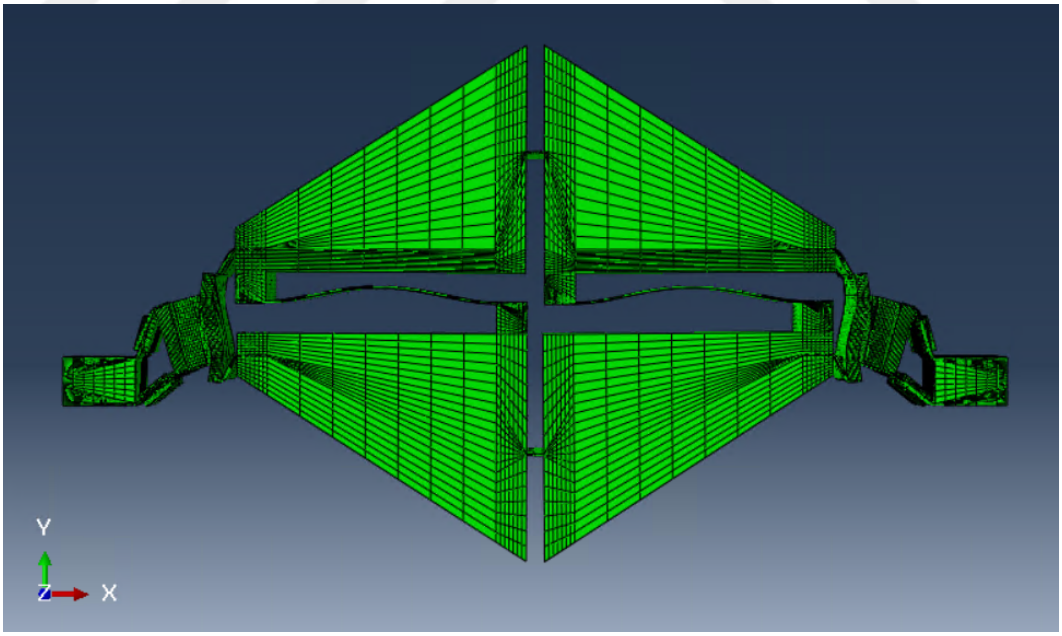


Figure 3.36. Fourth mode shape of the mechanism imposed to clamped-roller boundary condition at 404.4 Hz.

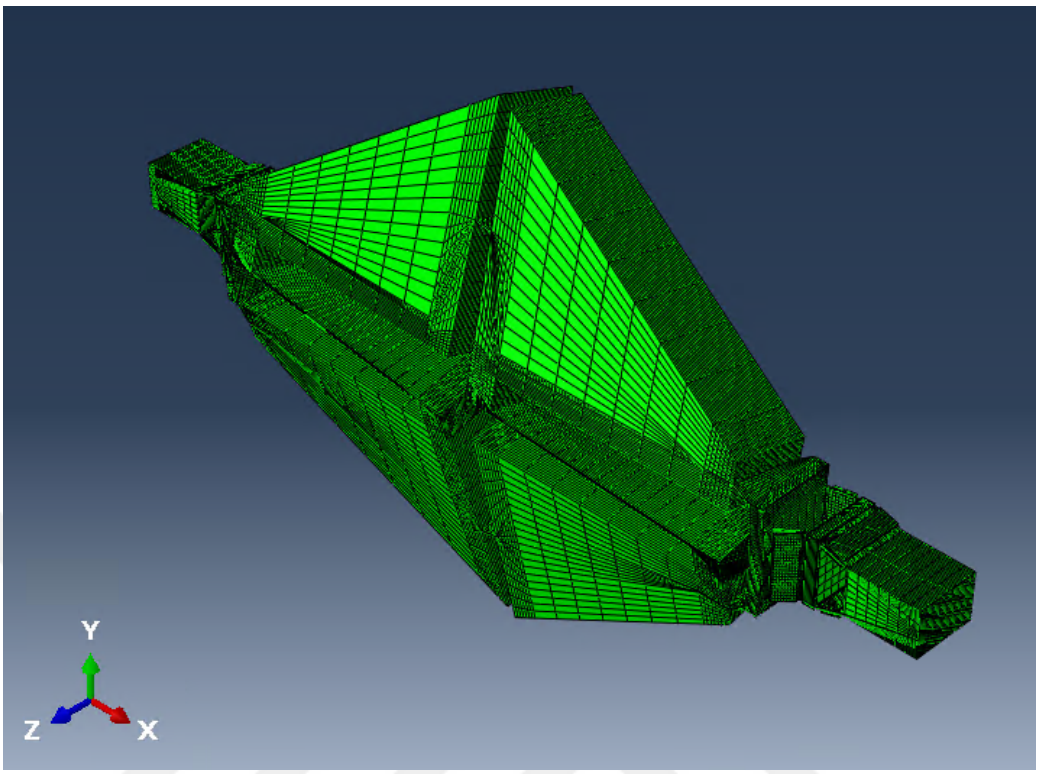


Figure 3.37. Fifth mode shape of the mechanism imposed to clamped-roller boundary condition at 719.1 Hz.

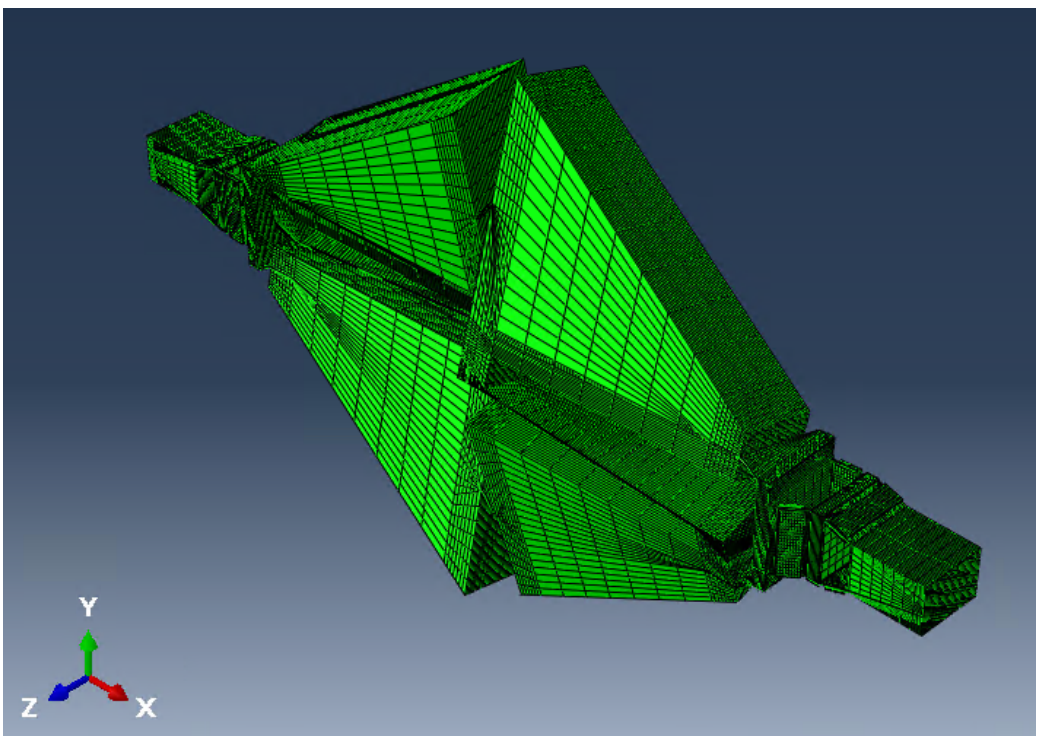


Figure 3.38. Sixth mode shape of the mechanism imposed to clamped-roller boundary condition at 721.1 Hz.

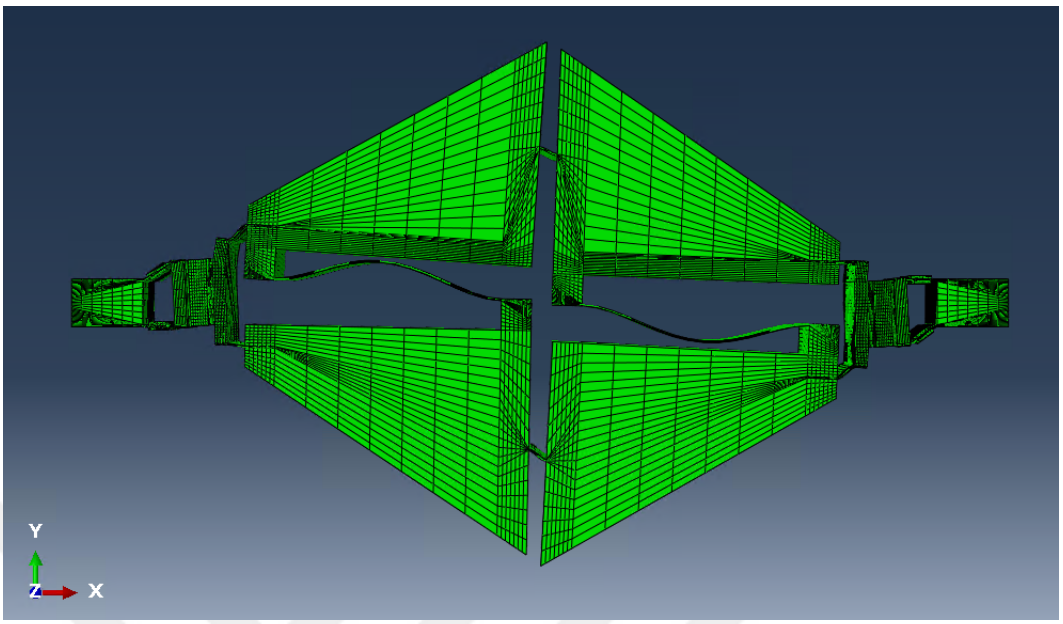


Figure 3.39. Seventh mode shape of the mechanism imposed to clamped-roller boundary condition at 888.3 Hz.

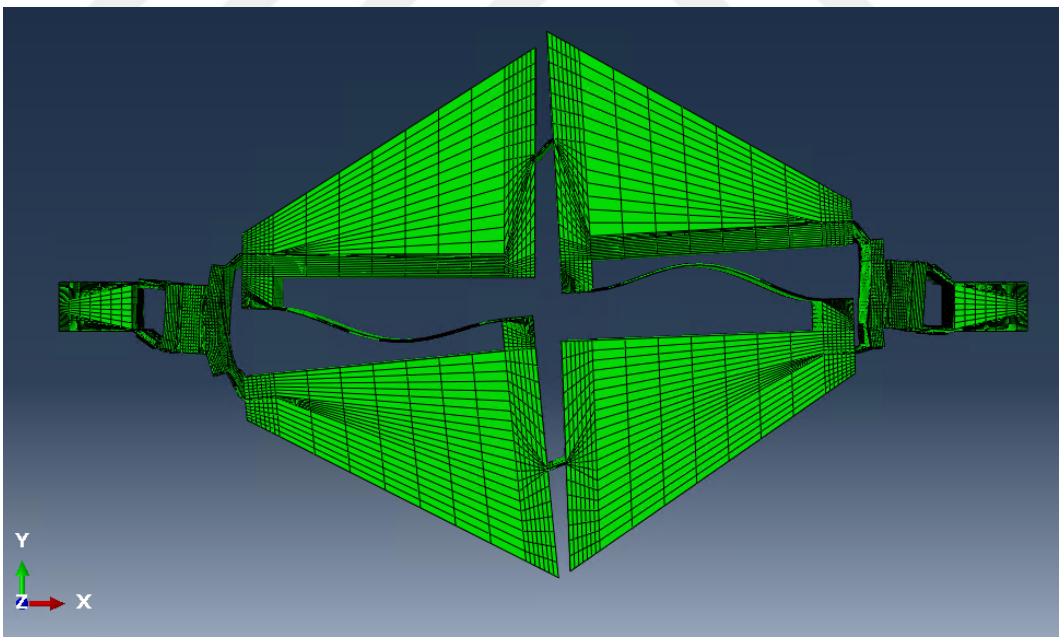


Figure 3.40. Eighth mode shape of the mechanism imposed to clamped-roller boundary condition at 904.5 Hz.

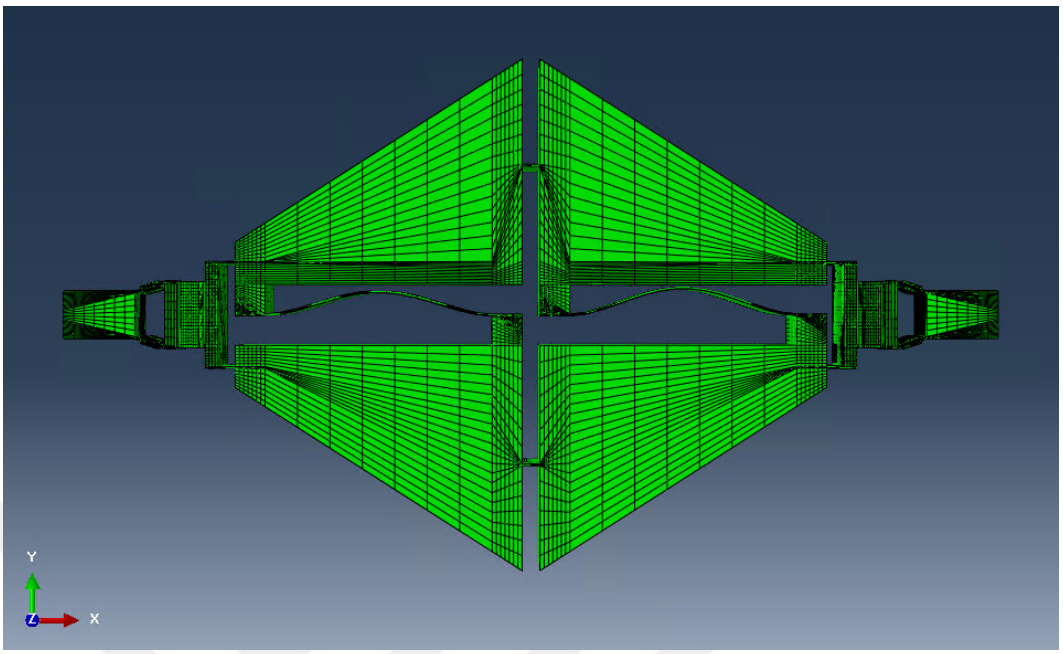


Figure 3.41. Ninth mode shape of the mechanism imposed to clamped-roller boundary condition at 1118 Hz.

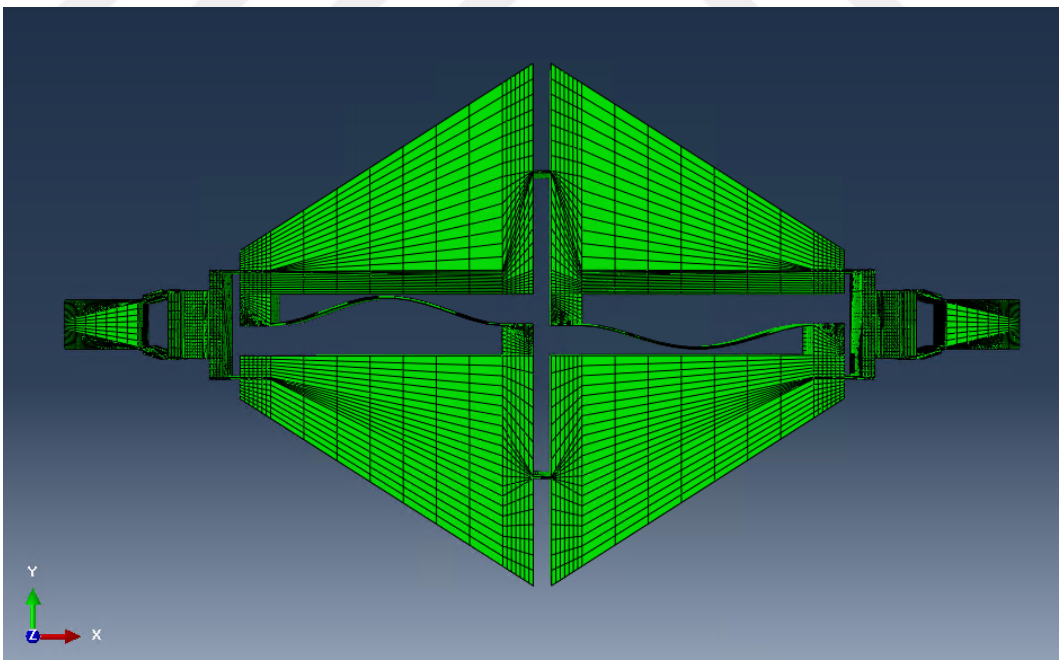
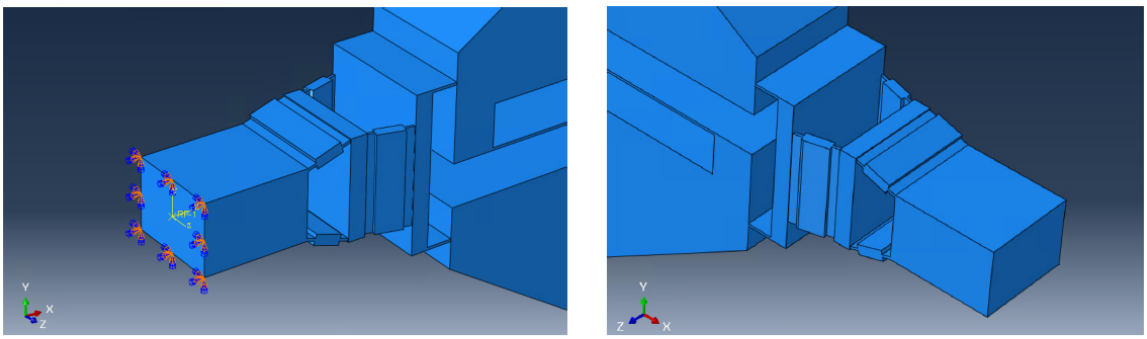


Figure 3.42. Tenth mode shape of the mechanism imposed to clamped-roller boundary condition at 1122 Hz.

Table 3.2. First ten natural frequencies of the mechanism shown in Figure 3.19 imposed to clamped-roller boundary condition.

Natural frequencies	Frequency (Hz)
ω_1	33.73
ω_2	300.9
ω_3	334.8
ω_4	404.4
ω_5	719.1
ω_6	721.1
ω_7	888.3
ω_8	904.5
ω_9	1118
ω_{10}	1122

When clamped-free boundary condition is imposed to the inertial amplification mechanism as shown in Figure 3.43, the resulting first five mode shapes are given in Figures 3.44-3.48, and corresponding natural frequencies are given in Table 3.3. The clamped boundary condition allows to investigate the bending stiffness of the remote center flexure mechanism in two orthogonal axes. Instead of a clamped end, if a frictionless ball joint were used, the natural frequencies of the modes seen in Figures 3.45 and 3.46 would be zero. However, the frequencies of these modes are greater than zero due to the stiffness of the remote center flexure mechanism in two orthogonal axes. As the natural frequency of the third mode is higher than the second mode, bending stiffness about the y axis is higher.



(a) (b)

Figure 3.43. Clamped-free boundary condition for the initial design of the mechanism. (a) Boundary condition at the left end. The back surface of the rectangular prism of the left end cannot translate or rotate in any direction. (b) The right end is free.

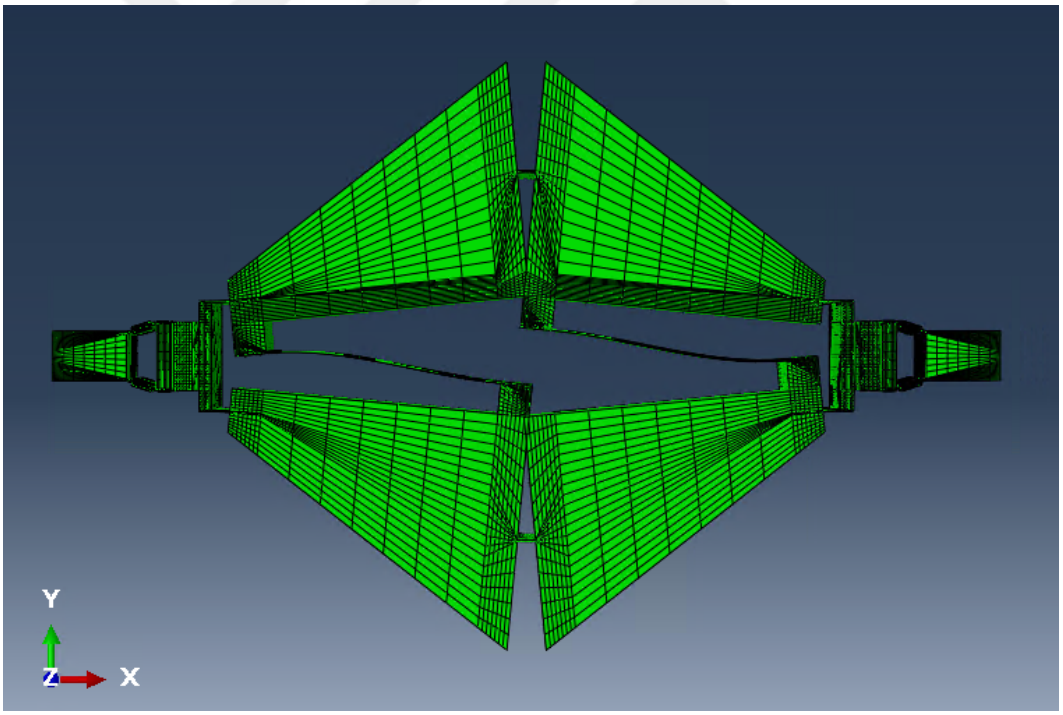


Figure 3.44. First mode shape of the mechanism imposed to clamped-free boundary condition at 33.73 Hz.

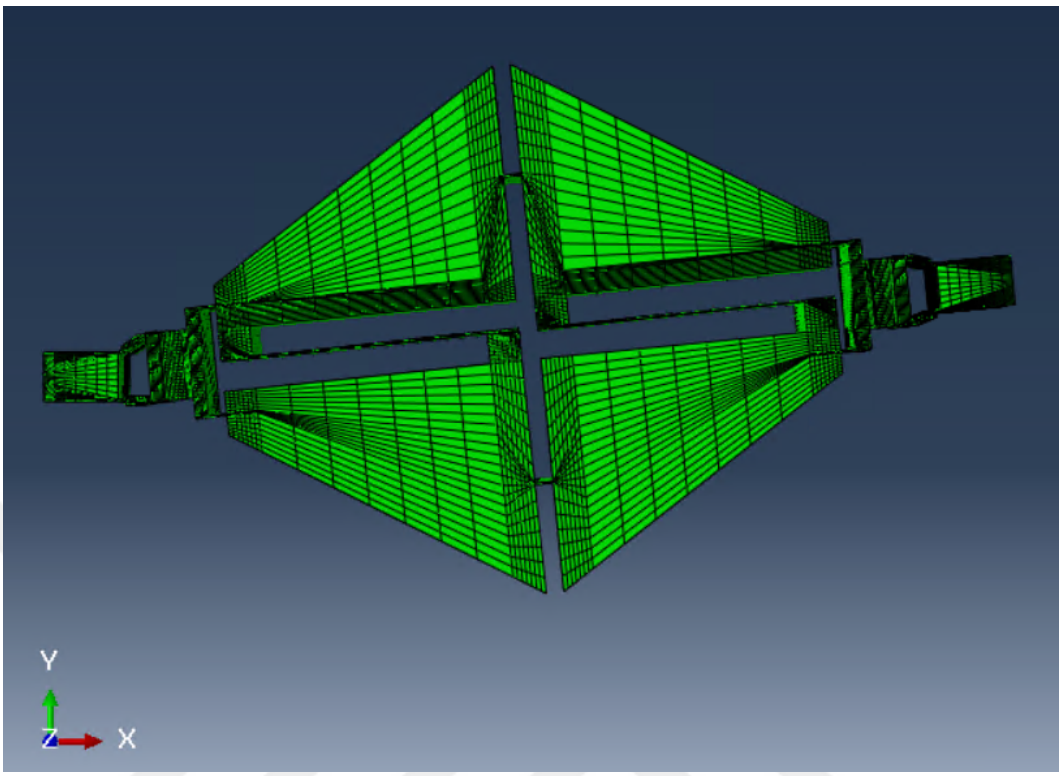


Figure 3.45. Second mode shape of the mechanism imposed to clamped-free boundary condition at 34.93 Hz.

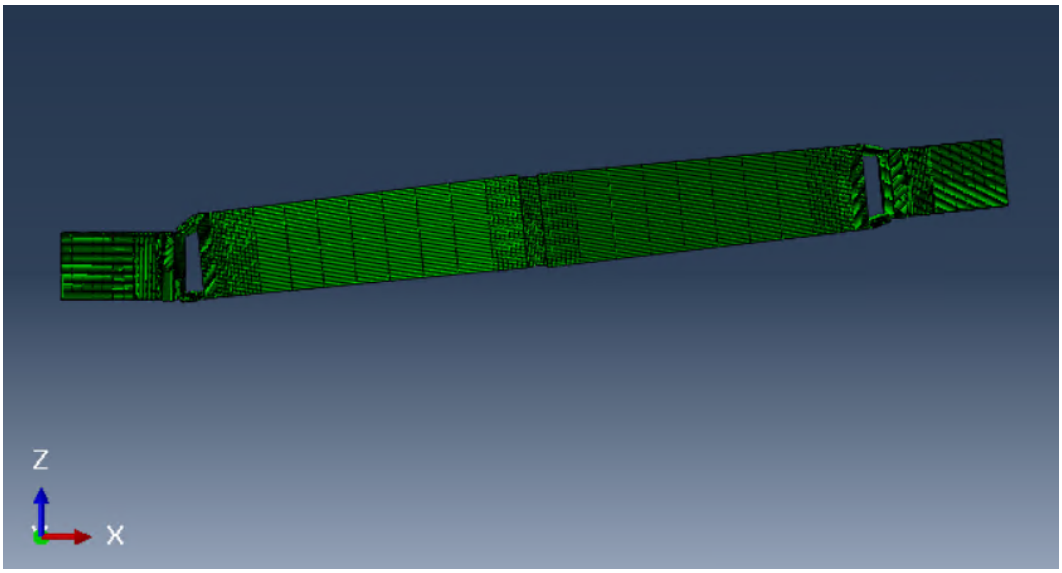


Figure 3.46. Third mode shape of the mechanism imposed to clamped-free boundary condition at 48.69 Hz.

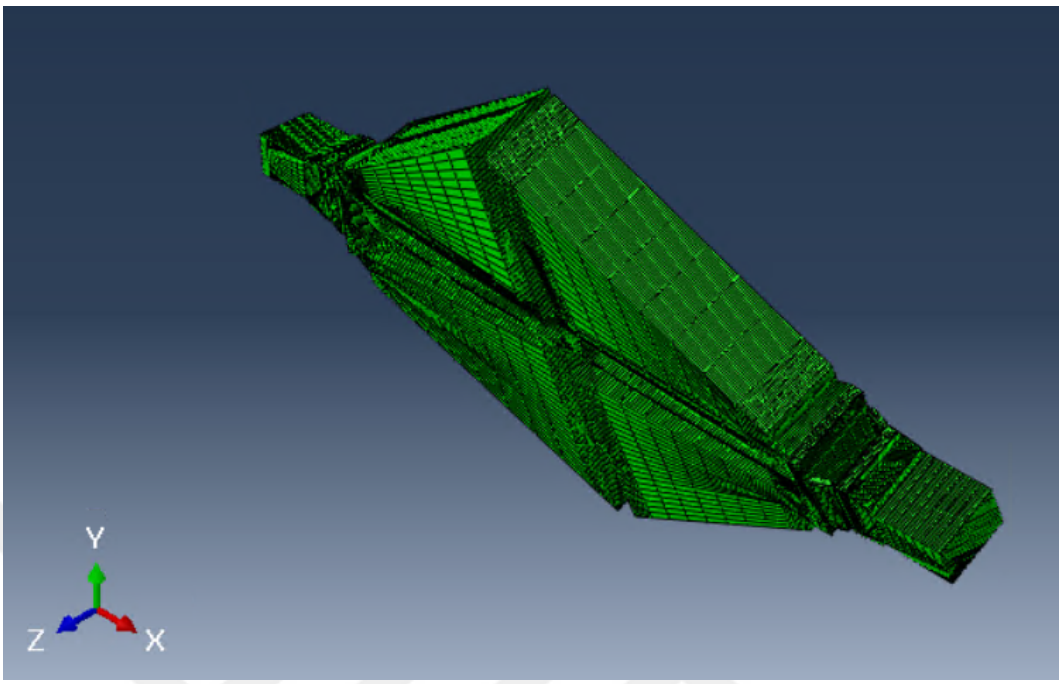


Figure 3.47. Fourth mode shape of the mechanism imposed to clamped-free boundary condition at 178.0 Hz.

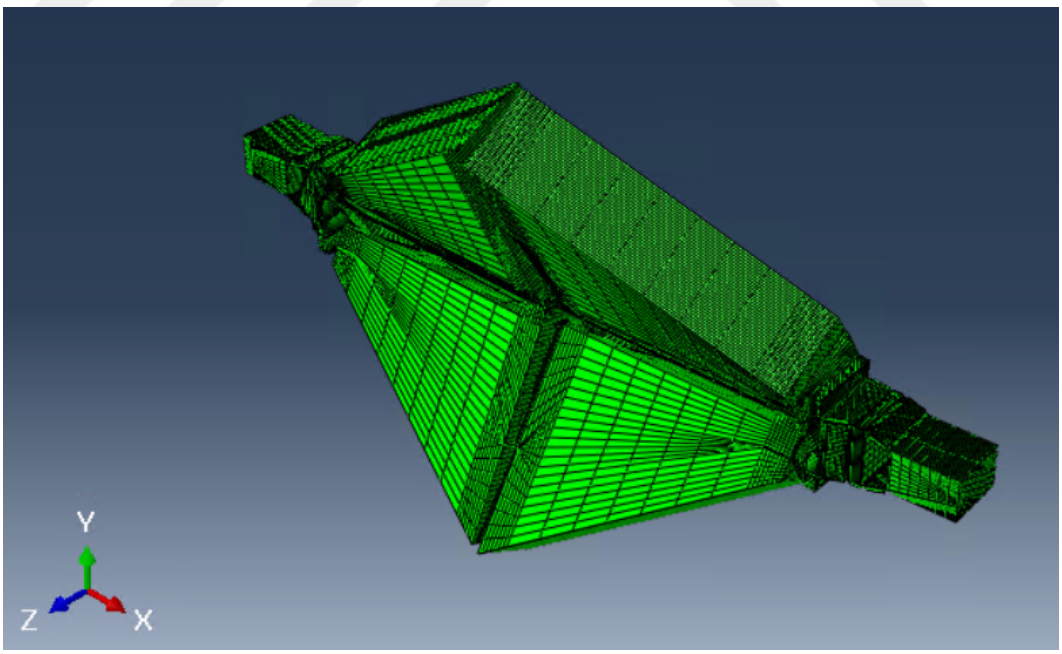


Figure 3.48. Fifth mode shape of the mechanism imposed to clamped-free boundary condition at 474.6 Hz.

Table 3.3. First five natural frequencies of the mechanism shown in Figure 3.19 imposed to clamped-free boundary condition.

Natural frequencies	Frequency (Hz)
ω_1	33.73
ω_2	34.93
ω_3	48.69
ω_4	178.0
ω_5	474.6

When Tables 3.1-3.3 are compared, one can see that the first natural frequency corresponding to the first mode is the same for different boundary conditions. However, as the boundary conditions change, the higher mode shapes and natural frequencies differ.

The aim in this thesis is to assemble inertial amplification mechanisms to form a 3D periodic structure. As an initial study, the mechanism in Figure 3.19 is used. The rectangular blocks at each end of the mechanism are joined at their centers of rotations shown in Figure 3.18 to form the nodes in the periodic structure. As there are two stages of remote center flexure mechanisms, the mechanisms can bend about two orthogonal axes. The initial design of the octahedron structure is shown in Figure 3.49, which is built as in [5]. The octahedron structure is the repeating unit cell in the 3D periodic structure shown in Figure 3.50.

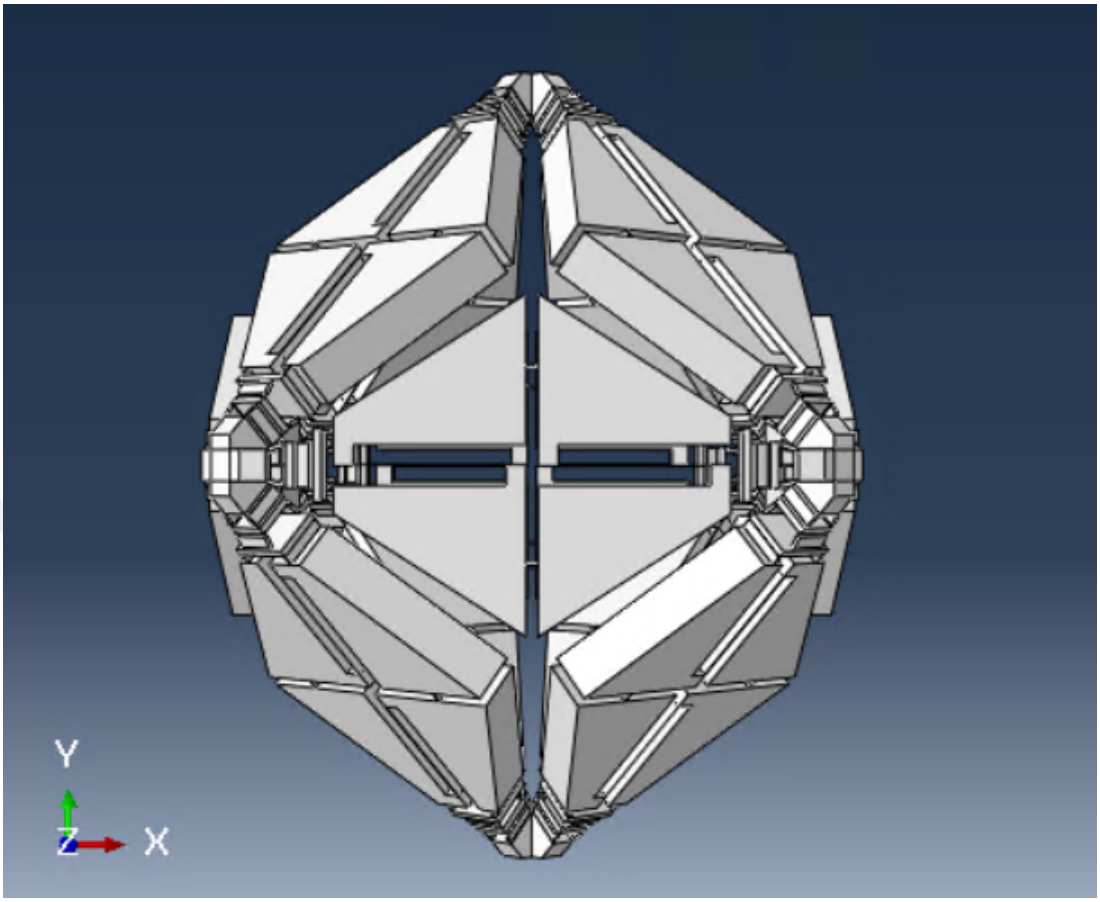


Figure 3.49. Octahedron structure formed with the mechanisms in Figure 3.19.

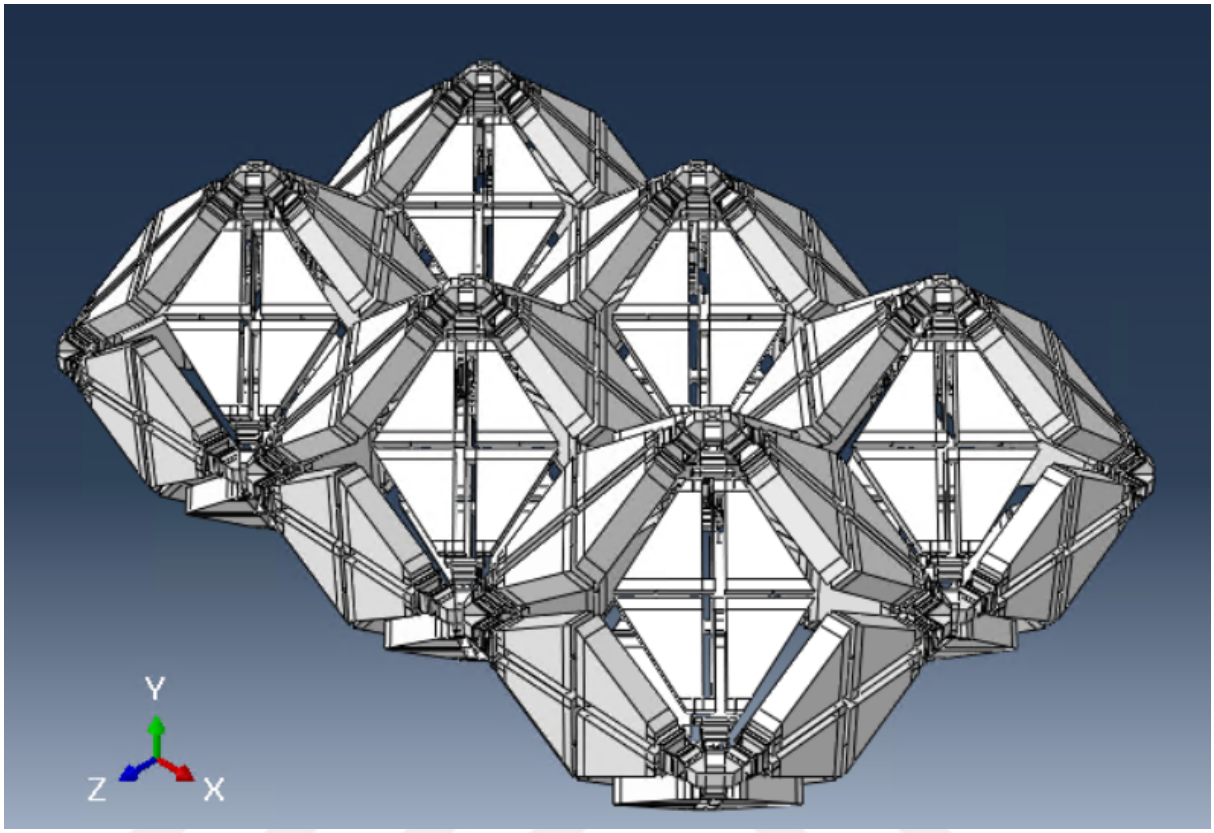


Figure 3.50. 3D periodic structure formed with the octahedron structures in Figure 3.49.

Imposing free boundary conditions, the natural frequencies of the octahedron structure are calculated. The finite element analysis shows that the first six frequencies are around zero, which correspond to the rigid body modes. Table 3.4 shows the non-zero natural frequencies of the structure.

Table 3.4. First 40 non-zero natural frequencies of the octahedron structure shown in Figure 3.49 imposed to free boundary conditions.

Natural frequencies	Frequency (Hz)	Natural frequencies	Frequency (Hz)
ω_1	34.32	ω_{21}	263.7
ω_2	36.60	ω_{22}	263.7
ω_3	37.24	ω_{23}	268.7
ω_4	37.24	ω_{24}	270.8
ω_5	42.26	ω_{25}	276.0
ω_6	42.26	ω_{26}	278.8
ω_7	42.60	ω_{27}	279.0
ω_8	46.27	ω_{28}	279.2
ω_9	46.27	ω_{29}	300.4
ω_{10}	46.50	ω_{30}	309.9
ω_{11}	50.32	ω_{31}	309.9
ω_{12}	50.69	ω_{32}	314.2
ω_{13}	209.7	ω_{33}	323.5
ω_{14}	209.7	ω_{34}	324.1
ω_{15}	227.7	ω_{35}	324.2
ω_{16}	227.7	ω_{36}	335.2
ω_{17}	227.8	ω_{37}	402.0
ω_{18}	253.6	ω_{38}	402.2
ω_{19}	253.6	ω_{39}	404.4
ω_{20}	263.2	ω_{40}	418.7

As can be seen from Table 3.4, the natural frequencies increase with small increments up to 50.69 Hz, which correspond to the 12th mode. The next mode occurs at 209.7 Hz. Hence, there is a large frequency gap between the 12th and 13th modes. The main aim in this study is to obtain a very wide frequency gap and to quantify the width of the frequency gap, ratio of the upper limit to the lower limit will be used.

ω_{13}/ω_{12} ratio can be calculated as 4.14 for the octahedron structure in Figure 3.49.

In the first 12 non-zero modes of the octahedron structure, the 1D building blocks, i.e., inertial amplification mechanisms, deform close to their first mode shapes for various boundary conditions given in Figures 3.22, 3.33 and 3.44. In fact, the frequency of the first mode shape of the inertial amplification mechanism is the same (33.73 Hz) for various boundary conditions as can be seen in Figures 3.22, 3.33 and 3.44. The first non-zero mode shape and the 12th mode shape of the octahedron structure, which determine the lower limit of the stop band, are shown in Figures 3.51 and 3.52, respectively. In the octahedron structure, when the nodes translate in three dimensions, the ends of the inertial amplification mechanisms are subject to both axial and transverse displacements. When the mechanism with clamped-free boundary condition is analyzed, it is seen that as the free end displaces transversely, the corresponding natural frequencies of the second and third modes given in Figures 3.45 and 3.46 are higher than that of the first mode shape in Figure 3.44 in which the free end displaces along the central axis of the mechanism. Due to these combined effects, the frequency of the 12th mode of the octahedron structure (50.69 Hz) is significantly higher than the first mode of the building block mechanisms (33.73 Hz) in which only axial displacements of the ends are observed. In the 13th mode shape given in Figure 3.53, which determine the upper limit of the stop band, the 1D building blocks, i.e., inertial amplification mechanisms, deform close to their second mode shapes in the case of clamped-pin roller boundary condition shown in Figure 3.23. In this mode, the triangular blocks display torsional vibration about the central axis of the mechanism. Moreover, the torsional mode shape is at 177.9 Hz when clamped-pin roller boundary condition is imposed to the mechanism and it is at 334.8 Hz when clamped-roller boundary condition is imposed. Torsional stiffness of the mechanism in which both ends are constrained to rotate is twice of that of the mechanism in which one end is constrained to rotate. Moreover, the inertia of the torsionally vibrating part is smaller when both ends are constrained to rotate. As the torsional stiffness is higher and the inertia is smaller in the case of clamped-roller boundary condition, the resulting natural frequency is significantly higher. In the octahedron structure, two ends of each mechanism are attached

to nodes. When these nodes are subject to torsional loads, they allow rotation but display some torsional resistance. Hence, the torsional natural frequency of the mechanisms in the octahedron structure is expected to be higher than the mechanism with clamped-pin roller boundary condition but lower than the mechanism with clamped-roller boundary condition. As expected, the natural frequency of the torsional mode shape of the octahedron is at 209.7 Hz, which is higher than 177.9 Hz, and lower than 334.8 Hz.

If the parameters of the inertial amplification mechanism are changed, another mode shape can be the upper limit of the stop band. For instance, in the 37th mode shape of the octahedron structure in Figure 3.54, some of the mechanisms display the fourth mode shape shown in Figure 3.36. Even small changes in the mechanism can increase or decrease the natural frequencies of the mode shapes, bring different mode shapes to the upper limit of the stop band and dramatically affect the ratio of the upper and lower limits of the stop band. In order to increase the upper to lower frequency ratio of the stop band, the upper limit is aimed to be increased while the lower limit is aimed to be decreased.

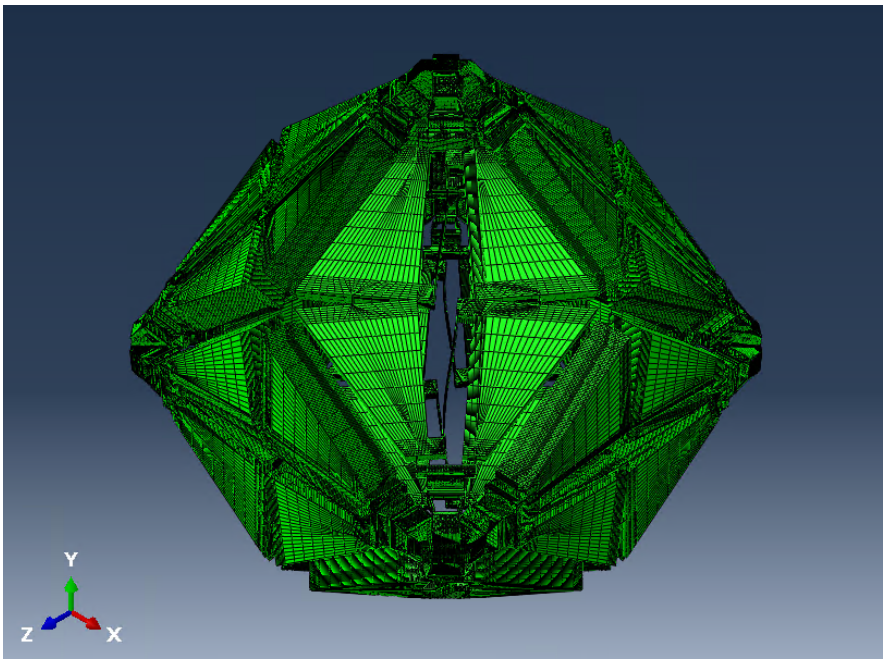


Figure 3.51. First mode shape of the octahedron in Figure 3.49 at 34.32 Hz.

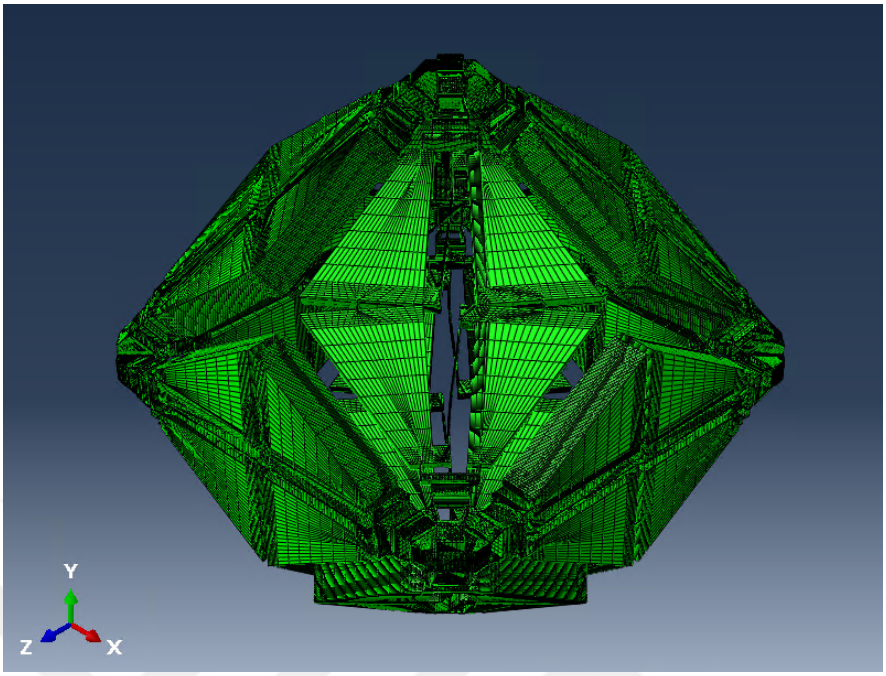


Figure 3.52. 12th mode shape of the octahedron in Figure 3.49 at 50.69 Hz.

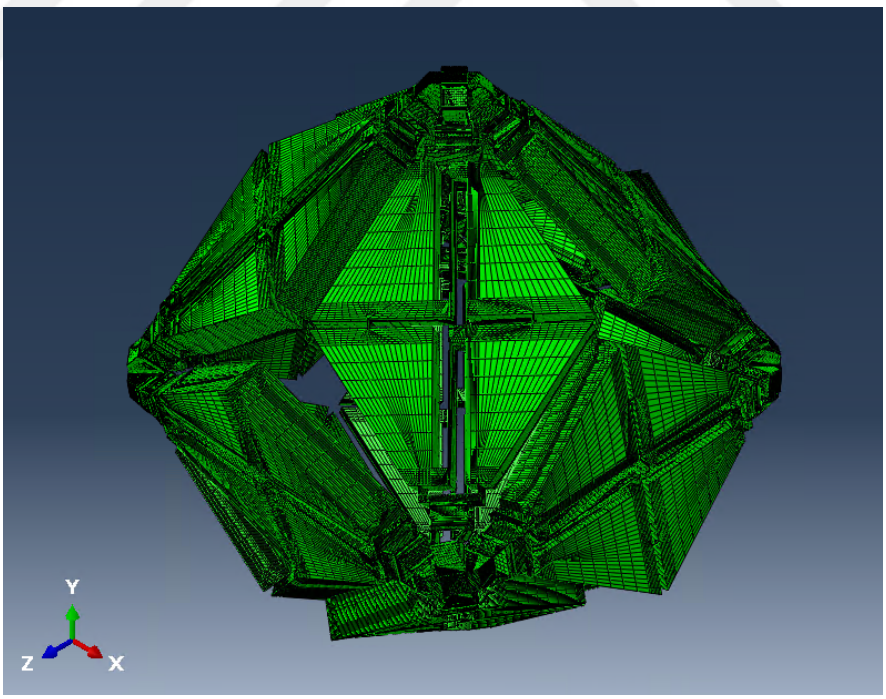


Figure 3.53. 13th mode shape of the octahedron in Figure 3.49 at 209.7 Hz.

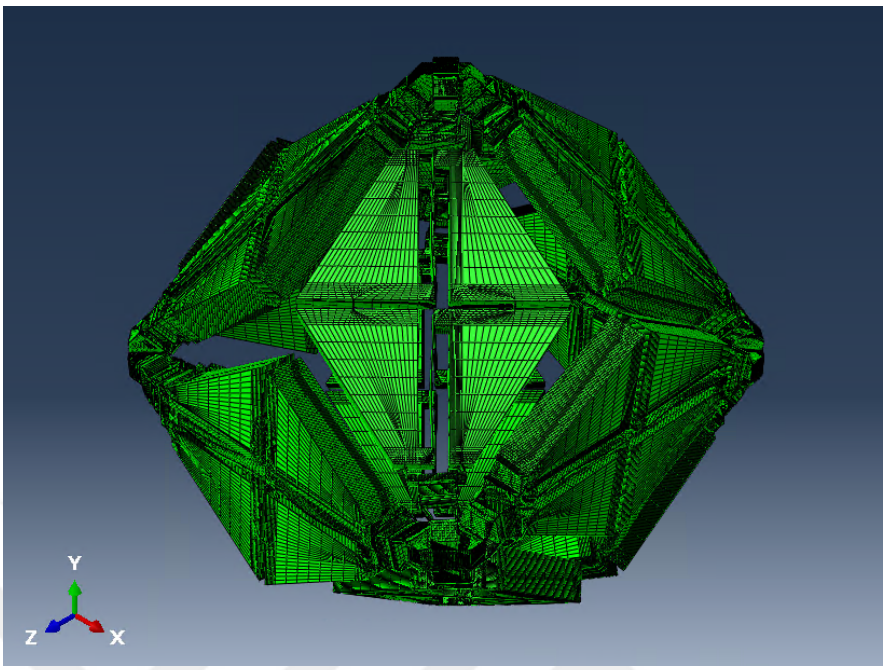


Figure 3.54. 37th mode shape of the octahedron in Figure 3.49 at 402.0 Hz.

3.3. Design Improvements and Topological Changes Regarding the Inertial Amplification Mechanism

The main purpose of the design improvement process is to maximize the ratio of the vibration isolation frequency band of the octahedron structure. Therefore, the lower limit of the stop band of the octahedron, with the first mode shape motion of a single mechanism in Figure 3.22, is aimed to be minimized, and the next natural frequency, with whichever type of mode shape (torsional, in-plane bending, out-of-plane bending, etc.), is aimed to be maximized.

In Figure 3.55, the short flexures that are attached to the triangular blocks can be seen in close up view regarding the second mode shape of the inertial amplification mechanism at 177.9 Hz. It can be seen that the short flexures are twisted due to the torsional motion of the triangular blocks.

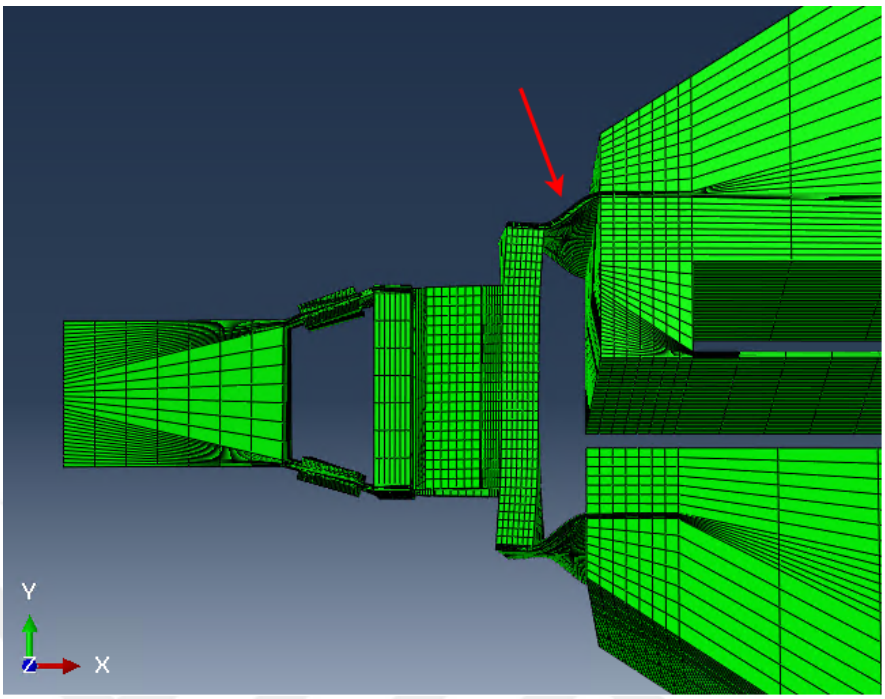


Figure 3.55. Close up view of the short flexures in the second mode shape shown in Figure 3.23 at 177.9 Hz.

Rather than dimensional changes, a topological design change is needed for the short flexures to prevent torsional motion of the triangular blocks. Instead of wide horizontal flexures, the novel cross flexure design is added to the mechanism. While this design does not change the first natural frequency significantly (33.73 Hz vs. 32.70 Hz), it provides much higher torsional stiffness, which in turn significantly increases the second natural frequency of the mechanism (177.9 Hz vs. 257.8 Hz). The cross flexure design is shown in Figure 3.56. Each inner flexure makes a 45° angle with the vertical axis. These flexures increase the torsional stiffness. However, cross flexures do not provide high axial stiffness, which is required to increase the natural frequencies of the out-of-plane modes. In order to increase the stiffness in the axial direction, horizontal flexures are used at the two sides. Figure 3.57 shows the second mode shape of the mechanism subject to clamped-pin roller boundary condition.

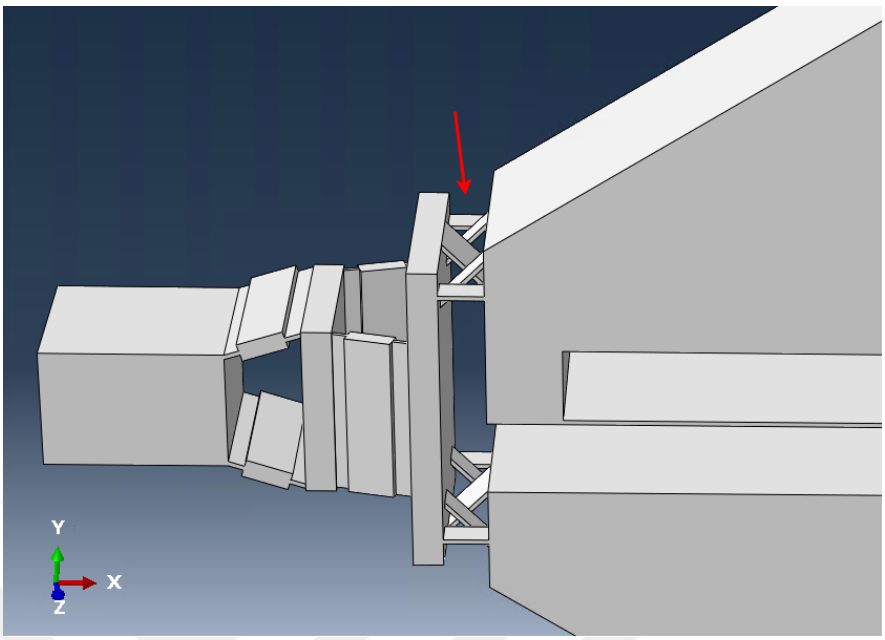


Figure 3.56. Design of cross flexures.

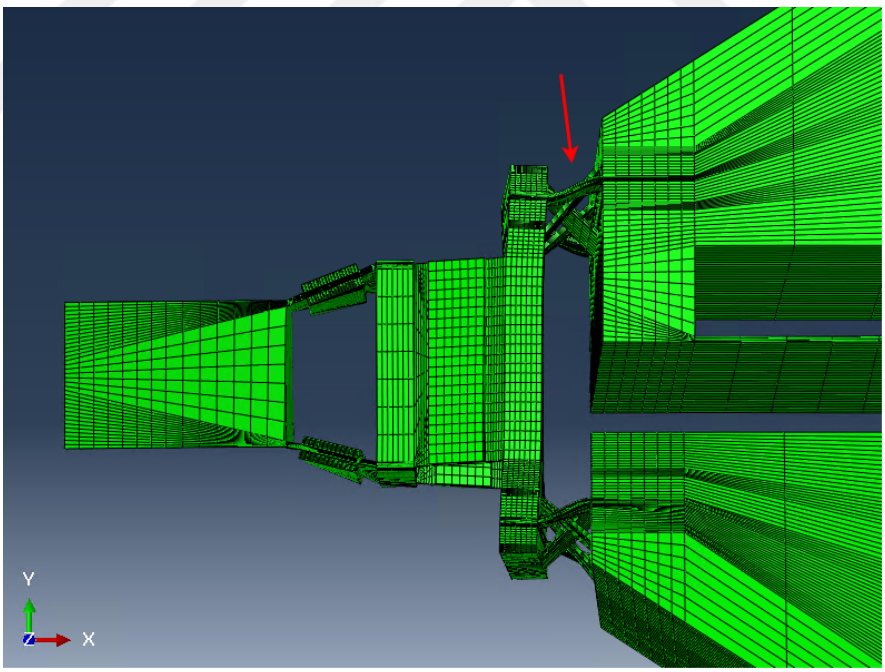


Figure 3.57. The second mode shape of the mechanism with cross flexure design at 257.8 Hz.

With clamped-pin roller boundary condition, the first natural frequency, ω_1, and the second natural frequency, ω_2, of the mechanism in Figure 3.19 with horizontal flexure are at 33.73 Hz and 177.9 Hz, respectively. Hence, the ratio of the second natural

frequency to the first one, ω_2/ω_1, is 5.27. Imposing the same boundary conditions, the first natural frequency, ω_1, and the second natural frequency, ω_2, of the mechanism with cross flexures are at 32.70 Hz and 257.8 Hz, and the ratio of these natural frequencies, ω_2/ω_1, is 7.88. Therefore, this design change improves the bandwidth of the mechanism.

The inertial amplification mechanism with cross flexures is shown in Figure 3.58. In this mechanism, the thickness of the rectangular blocks connected to the flexure hinge mechanisms arrowed in Figure 3.58 are increased by keeping the total length of the mechanism constant. Hence, the bending motion of these blocks are prevented. The octahedron structure built with these mechanisms is shown in Figure 3.59.

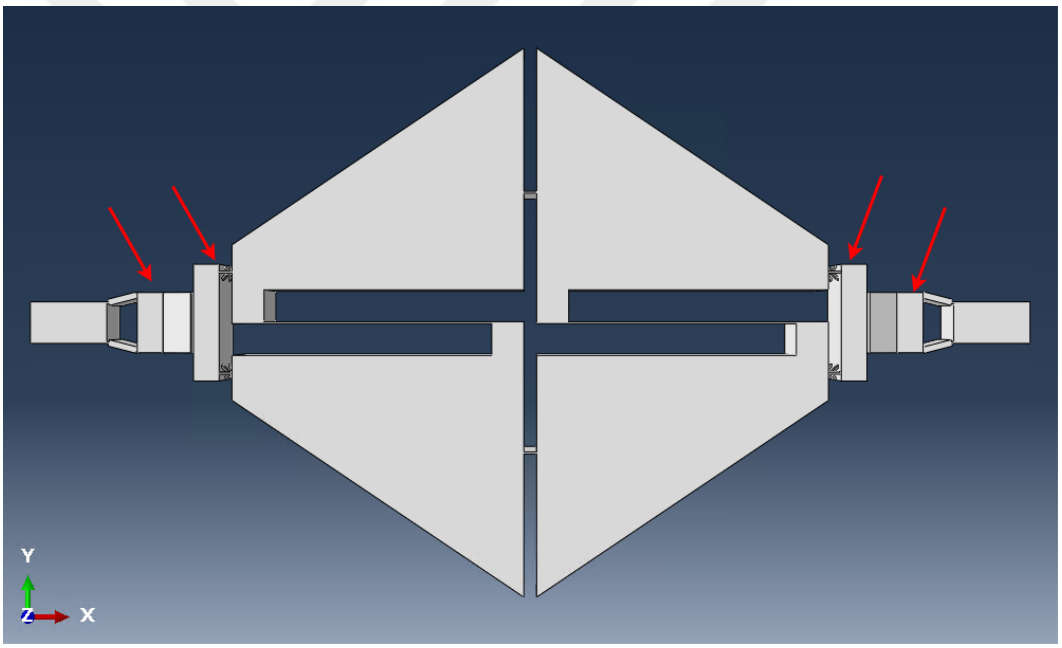


Figure 3.58. Inertial amplification mechanism with cross flexures.

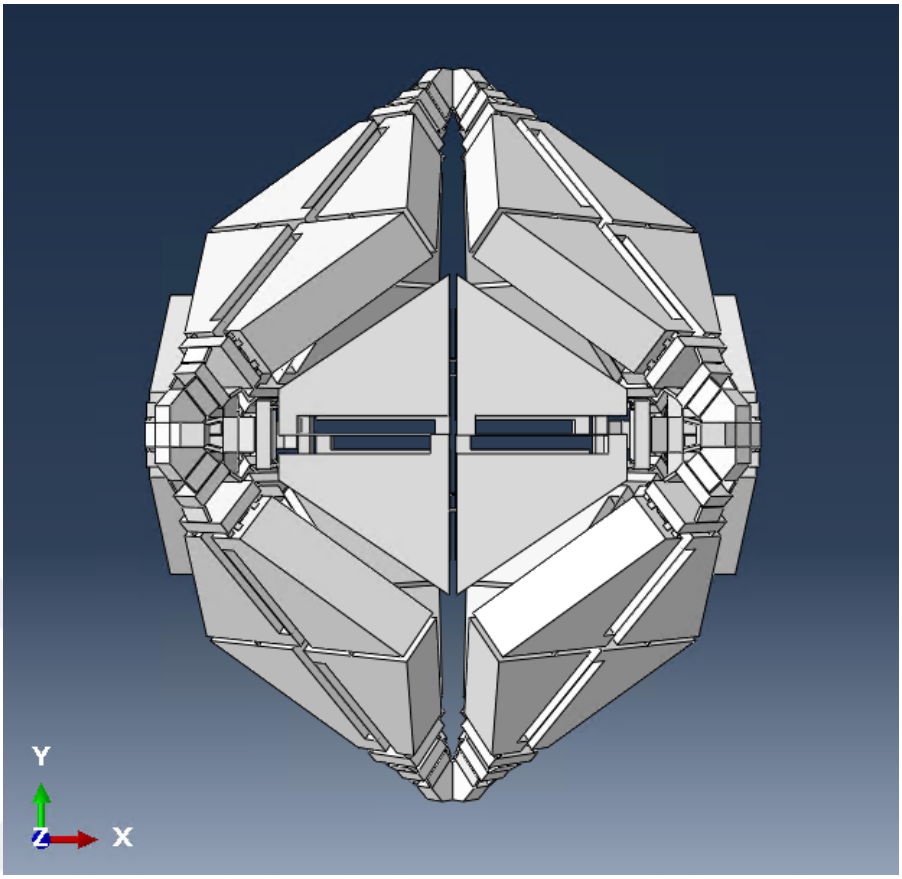


Figure 3.59. Octahedron structure formed with the mechanisms in Figure 3.58.

Imposing free boundary conditions, the natural frequencies of the octahedron structure are calculated. The first 40 non-zero natural frequencies of the octahedron are given in Table 3.5.

Table 3.5. First 40 non-zero natural frequencies of the octahedron structure shown in Figure 3.59 imposed to free boundary conditions.

Natural frequencies	Frequency (Hz)	Natural frequencies	Frequency (Hz)
ω_1	43.33	ω_{21}	376.4
ω_2	44.97	ω_{22}	376.6
ω_3	45.59	ω_{23}	376.7
ω_4	45.61	ω_{24}	426.8
ω_5	51.12	ω_{25}	427.3
ω_6	51.12	ω_{26}	427.3
ω_7	51.46	ω_{27}	440.1
ω_8	56.63	ω_{28}	441.0
ω_9	56.66	ω_{29}	445.4
ω_{10}	56.93	ω_{30}	445.4
ω_{11}	61.79	ω_{31}	445.8
ω_{12}	61.99	ω_{32}	446.2
ω_{13}	277.6	ω_{33}	455.4
ω_{14}	277.7	ω_{34}	458.7
ω_{15}	300.4	ω_{35}	459.2
ω_{16}	301.0	ω_{36}	459.3
ω_{17}	301.1	ω_{37}	487.9
ω_{18}	353.5	ω_{38}	488.1
ω_{19}	353.9	ω_{39}	489.0
ω_{20}	355.2	ω_{40}	510.0

It can be seen that the stop band occurs again between the 12th and 13th modes. The lower limit of the stop band, ω_{12}, is 61.99 Hz and the upper limit of the stop band, ω_{13}, is 277.6 Hz. Comparing this stop band with the one in Table 3.4, it can be seen that ω_{12} increases from 50.69 Hz to 61.99 Hz and ω_{13} increases from 209.7 Hz to 277.6 Hz. Since the increase in the upper limit of the stop band, ω_{13}, is relatively larger than

the increase in the lower limit of the stop band, ω_{12}, the ratio ω_{13}/ω_{12} increases from 4.14 to 4.48. The mode shapes at the lower and upper limit of the stop band of the octahedron in Figure 3.59 are shown in Figures 3.60 and 3.61, respectively.

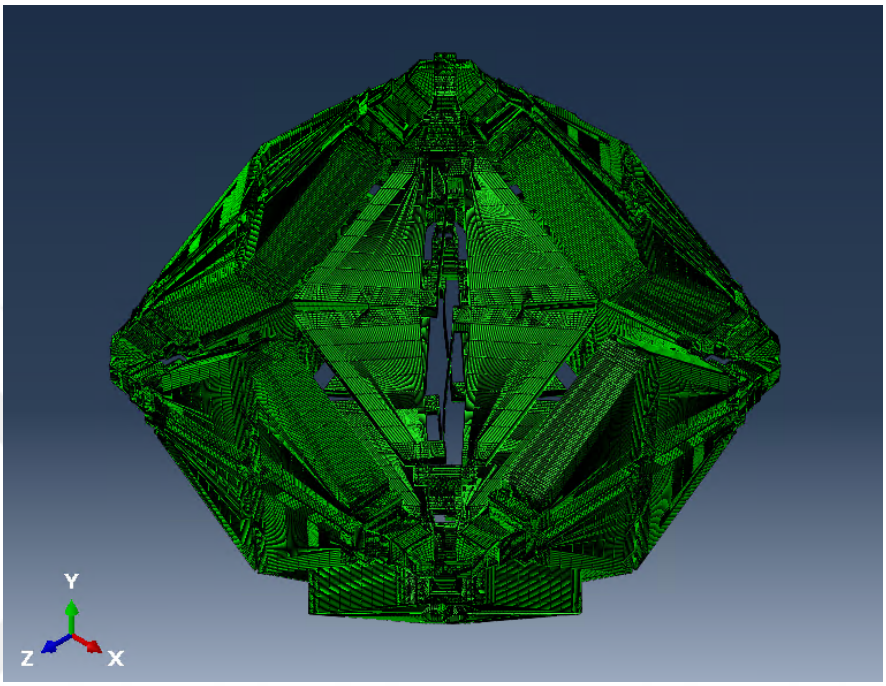


Figure 3.60. 12th mode shape of the octahedron in Figure 3.59 at 61.99 Hz.

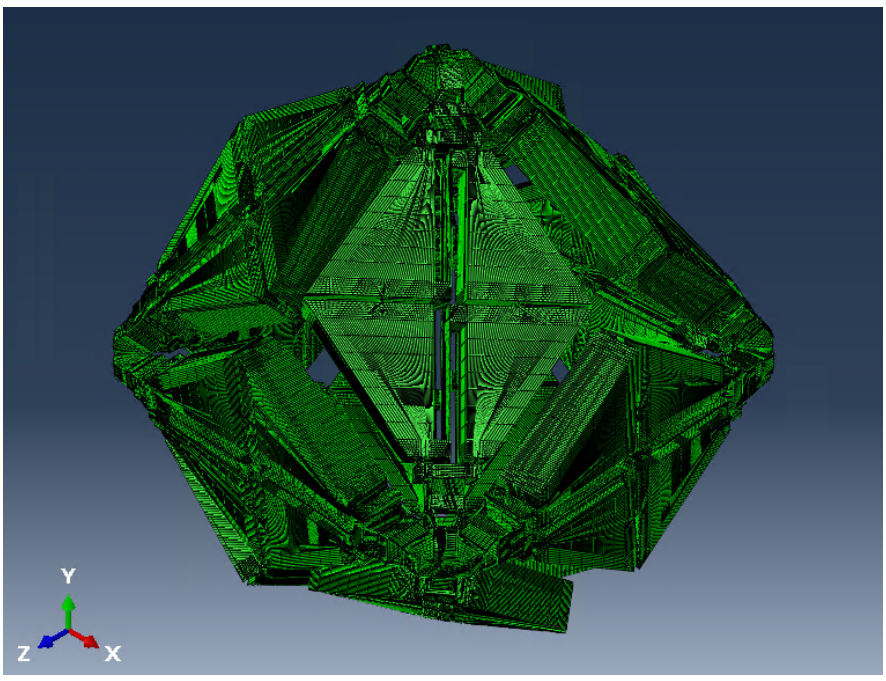


Figure 3.61. 13th mode shape of the octahedron in Figure 3.59 at 277.6 Hz.

In Figure 3.62, the horizontal and vertical axes are drawn passing through the center of the mechanism. In order to increase the natural frequency of the torsional mode shape of this mechanism, the centers of mass of the triangular blocks should approach the horizontal axis, and the moment of inertia of the rotating part should be decreased. To do that, the peak point of the triangular blocks are decreased as in Figure 3.63. Furthermore, the triangular blocks are hollowed out as shown in Figure 3.64 and supported with a truss structure in order to prevent the bending of the triangular blocks. Thus, the centers of mass of the triangular blocks are brought closer to both the vertical and horizontal axes as shown in Figure 3.62. If the center of mass of the triangular blocks were placed close to the vertical axis and its mass were preserved, the first natural frequency would decrease. However, the mass of the triangular blocks are significantly reduced due to the truss structure. Thus, the first natural frequency will increase. But, the natural frequency of the torsional mode will increase more. As a result, the ratio of the upper and lower limits of natural frequencies will increase.

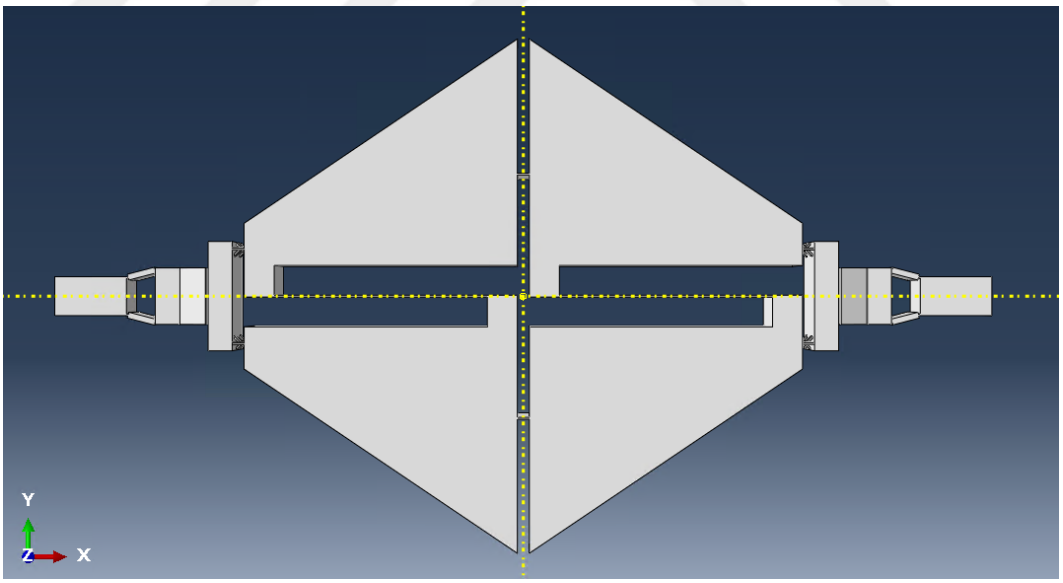


Figure 3.62. Inertial amplification mechanism in Figure 3.58 with horizontal and vertical lines passing through the center of mass of the mechanism.

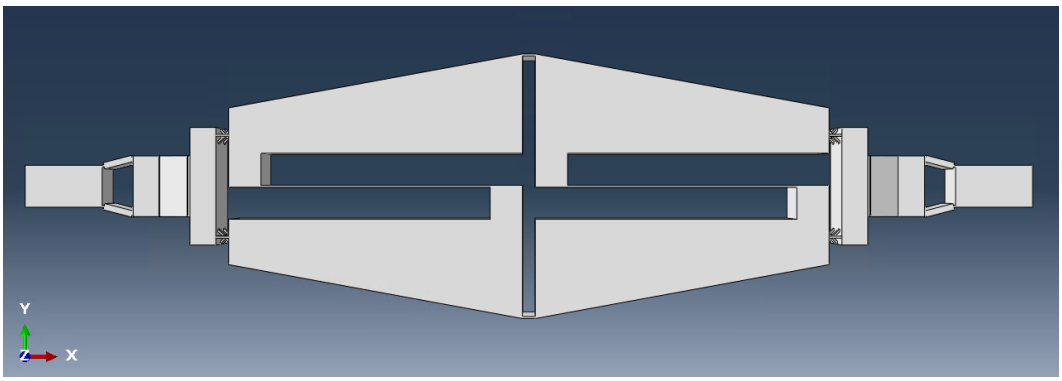


Figure 3.63. Inertial amplification mechanism with triangular blocks with reduced heights.

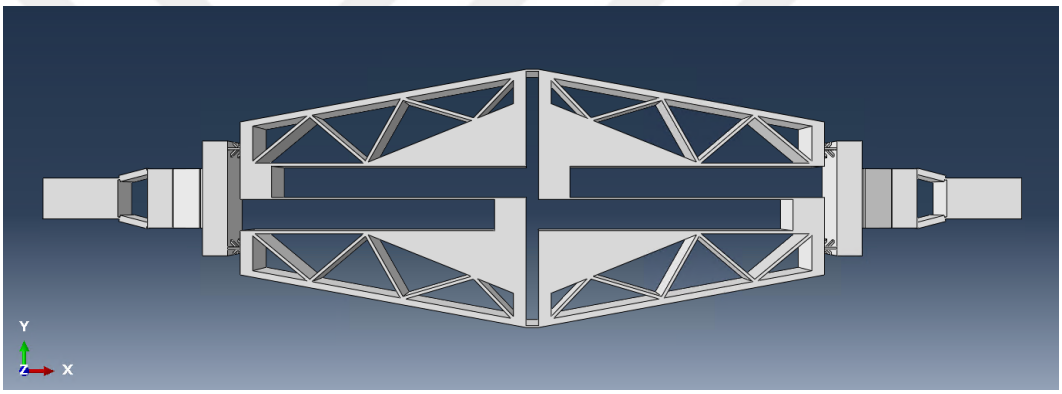


Figure 3.64. Inertial amplification mechanism with triangular blocks supported by trusses.

The octahedron structure built with the mechanism in Figure 3.64 is shown in Figure 3.65. Imposing free boundary conditions, the natural frequencies of the octahedron structure are calculated and the first 40 non-zero natural frequencies are given in Table 3.6.

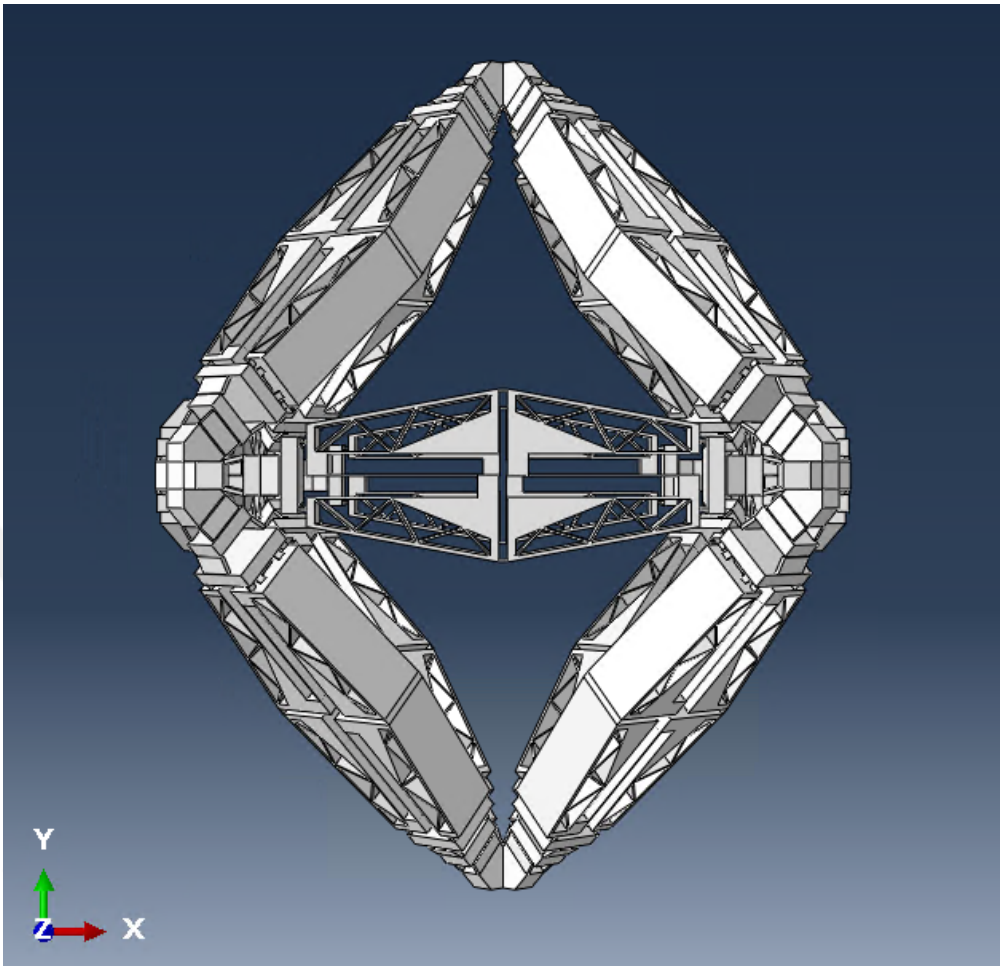


Figure 3.65. Octahedron structure formed with the mechanism in Figure 3.64.

Table 3.6. First 40 non-zero natural frequencies of the octahedron structure shown in Figure 3.65 imposed to free boundary conditions.

Natural frequencies	Frequency (Hz)	Natural frequencies	Frequency (Hz)
ω_1	75.49	ω_{21}	715.8
ω_2	78.35	ω_{22}	718.3
ω_3	79.53	ω_{23}	718.4
ω_4	79.53	ω_{24}	723.2
ω_5	88.48	ω_{25}	723.2
ω_6	88.49	ω_{26}	724.2
ω_7	89.14	ω_{27}	829.3
ω_8	97.23	ω_{28}	851.6
ω_9	97.24	ω_{29}	851.7
ω_{10}	97.82	ω_{30}	851.7
ω_{11}	107.1	ω_{31}	896.7
ω_{12}	107.4	ω_{32}	898.6
ω_{13}	623.0	ω_{33}	898.8
ω_{14}	624.9	ω_{34}	994.0
ω_{15}	625.0	ω_{35}	995.5
ω_{16}	670.0	ω_{36}	1039
ω_{17}	670.1	ω_{37}	1039
ω_{18}	671.2	ω_{38}	1039
ω_{19}	704.5	ω_{39}	1040
ω_{20}	705.9	ω_{40}	1040

Again, the stop band occurs between the 12th and 13th modes. When the stop bands in Tables 3.5 and 3.6 are compared, it can be seen that both ω_{12} and ω_{13} increase, since the total mass of the mechanism is decreased. ω_{12} increases from 61.99 Hz to 107.4 Hz and ω_{13} increases from 277.6 Hz to 623.0 Hz. However, the ratio ω_{13}/ω_{12} increases from 4.48 to 5.80. The 12th and 13th mode shapes are shown in Figures 3.66

and 3.67. As can be seen in Figure 3.67, the mode shape of the upper limit changes this time. In Figure 3.61, the mechanisms make the torsional motion. However, in Figure 3.67, the mechanisms make the out-of-plane bending motion.

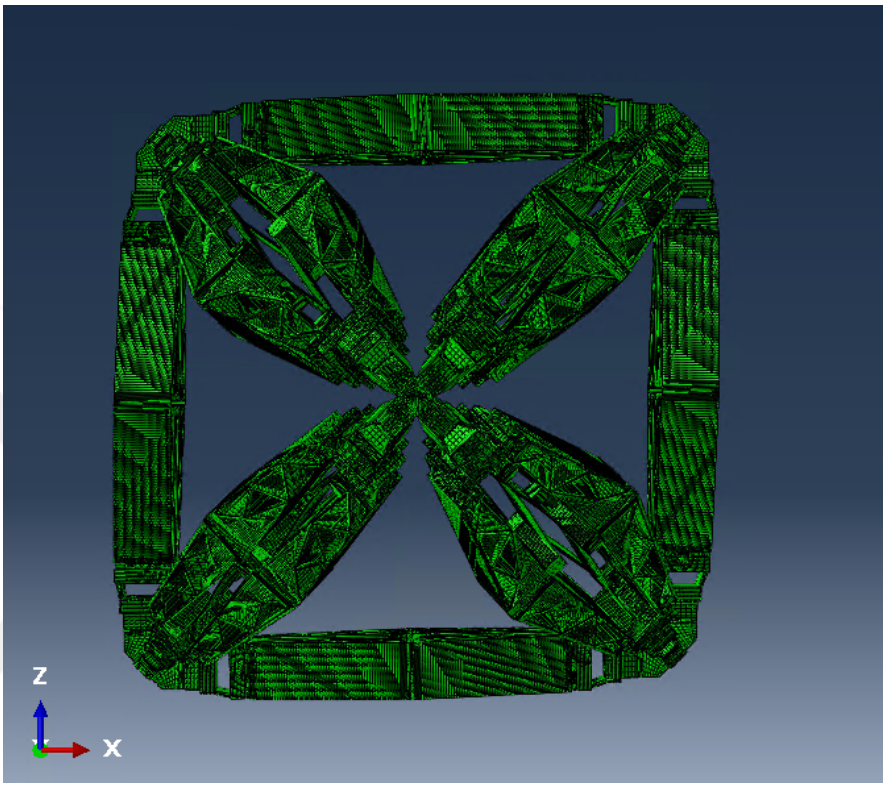


Figure 3.66. 12th mode shape of the octahedron in Figure 3.65 at 107.4 Hz.

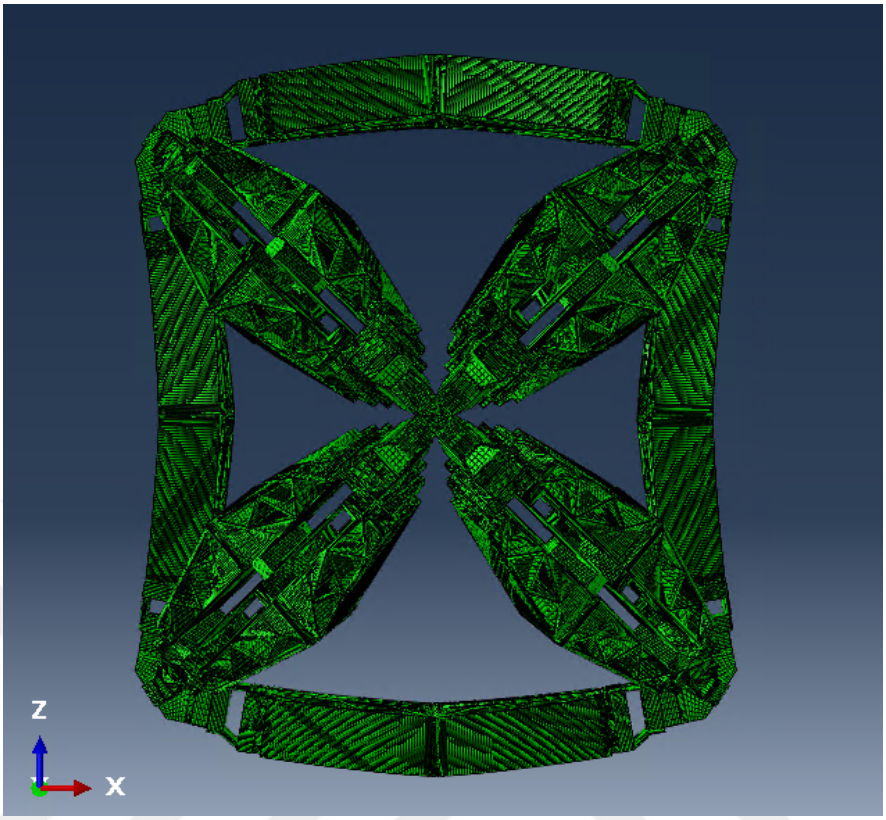


Figure 3.67. 13th mode shape of the octahedron in Figure 3.65 at 623.0 Hz.

In order to increase the natural frequency of the mode shape with out-of-plane bending motion, the out-of-plane bending stiffness of the middle short flexures can be increased. To that end, the width of the mechanism is increased in the middle by adding rectangular blocks to the sides of the mechanism and the middle flexures are divided into two as in Figures 3.68 and 3.69. The two pieces are placed towards the two ends of the widened section to increase the out-of-plane bending stiffness. If the middle short flexures were extended across the widened section of the mechanism, their in-plane bending stiffness would increase, which in turn would increase the first natural frequency. As a result, the bandwidth would decrease.

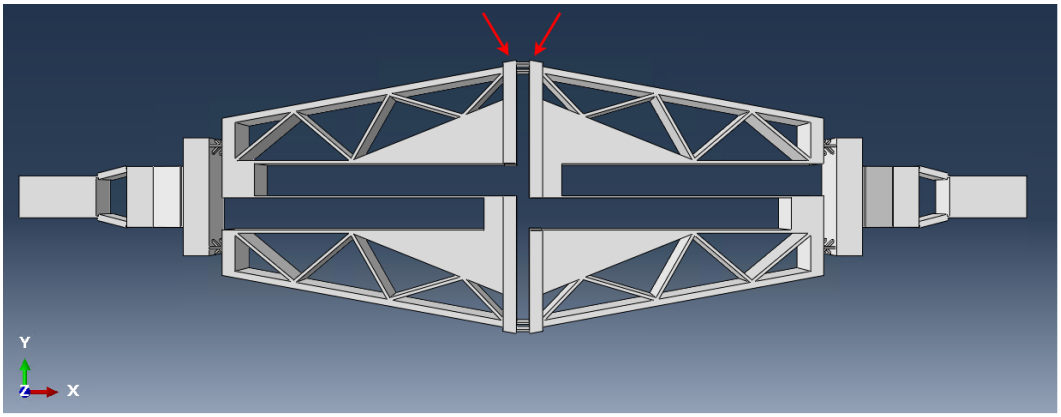


Figure 3.68. Inertial amplification mechanism with the added rectangular blocks in the middle.

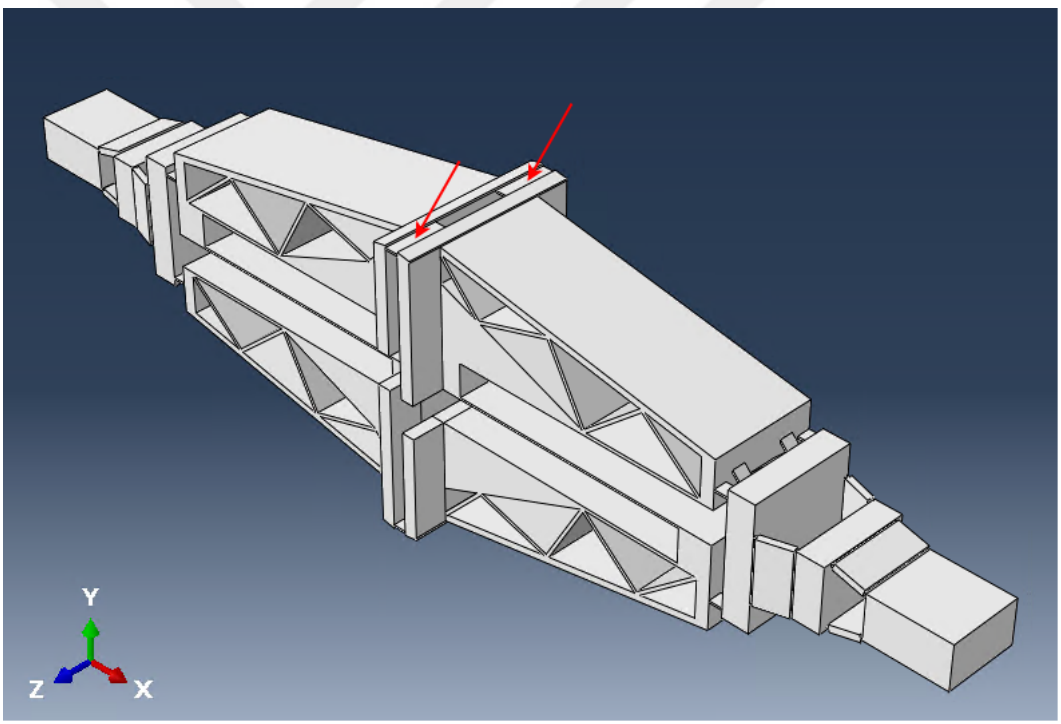


Figure 3.69. Isometric view of the inertial amplification mechanism in Figure 3.68 in which the middle flexures are divided into two and placed far away from each other to increase the out-of-plane bending stiffness.

With the inertial amplification mechanism in Figure 3.68, the octahedron structure is built and shown in Figure 3.70. The natural frequencies of the octahedron imposed to free boundary conditions are given in Table 3.7.

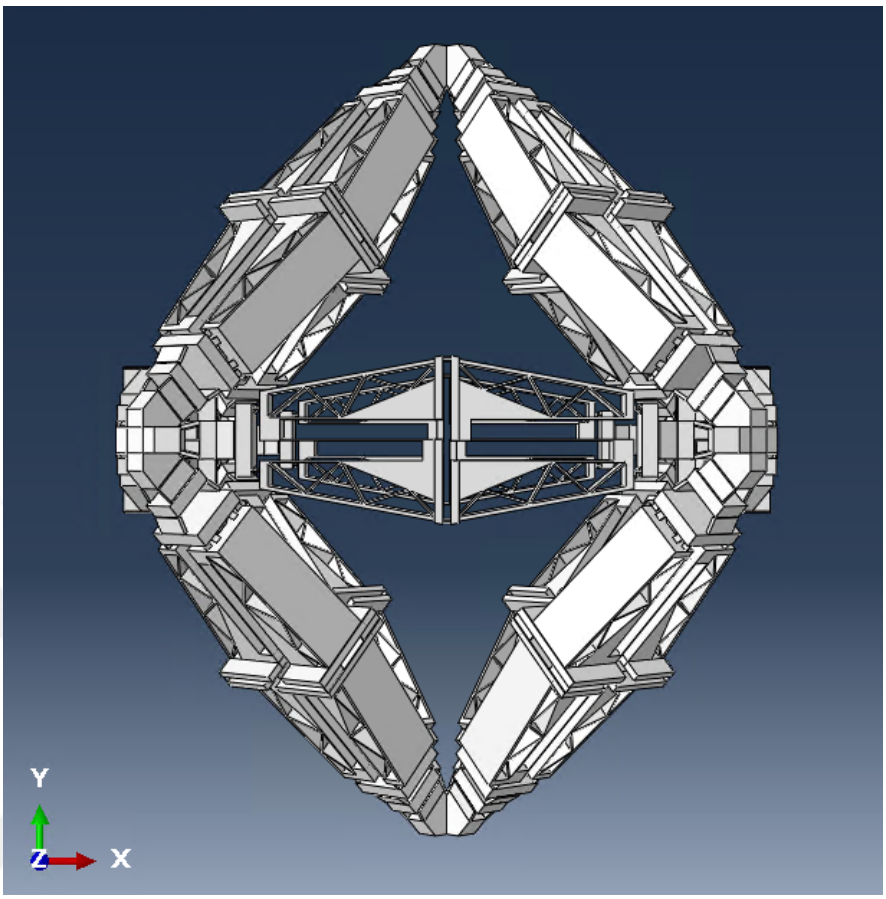


Figure 3.70. Octahedron structure formed with the mechanism in Figure 3.68.

Table 3.7. First 40 non-zero natural frequencies of the octahedron structure shown in Figure 3.70 imposed to free boundary conditions.

Natural frequencies	Frequency (Hz)	Natural frequencies	Frequency (Hz)
ω_1	71.90	ω_{21}	713.4
ω_2	74.79	ω_{22}	714.7
ω_3	75.89	ω_{23}	721.0
ω_4	75.89	ω_{24}	724.0
ω_5	84.11	ω_{25}	724.0
ω_6	84.12	ω_{26}	725.0
ω_7	84.72	ω_{27}	795.1
ω_8	93.20	ω_{28}	813.5
ω_9	93.21	ω_{29}	813.6
ω_{10}	93.77	ω_{30}	813.6
ω_{11}	102.3	ω_{31}	850.2
ω_{12}	102.7	ω_{32}	852.3
ω_{13}	630.7	ω_{33}	852.4
ω_{14}	632.5	ω_{34}	938.6
ω_{15}	632.6	ω_{35}	940.2
ω_{16}	678.3	ω_{36}	986.8
ω_{17}	678.3	ω_{37}	986.8
ω_{18}	679.5	ω_{38}	989.4
ω_{19}	685.6	ω_{39}	994.0
ω_{20}	685.8	ω_{40}	994.0

Similar to previous octahedron analyses, the stop band occurs between the 12th and 13th modes. The lower limit of the stop band, ω_{12}, decreases from 107.4 Hz to 102.7 Hz due to the addition of the rectangular blocks in the middle, and the upper limit of the stop band, ω_{13}, increases from 623.0 Hz to 630.7 Hz due to the increasing out-of-plane bending stiffness of the middle flexures. Hence, the ratio ω_{13}/ω_{12} increases

from 5.80 to 6.14. The 12th and 13th mode shapes are shown in Figures 3.71 and 3.72, respectively. It can be seen that the mode shape at the upper limit of the stop band of the octahedron is still the out-of-plane motion.

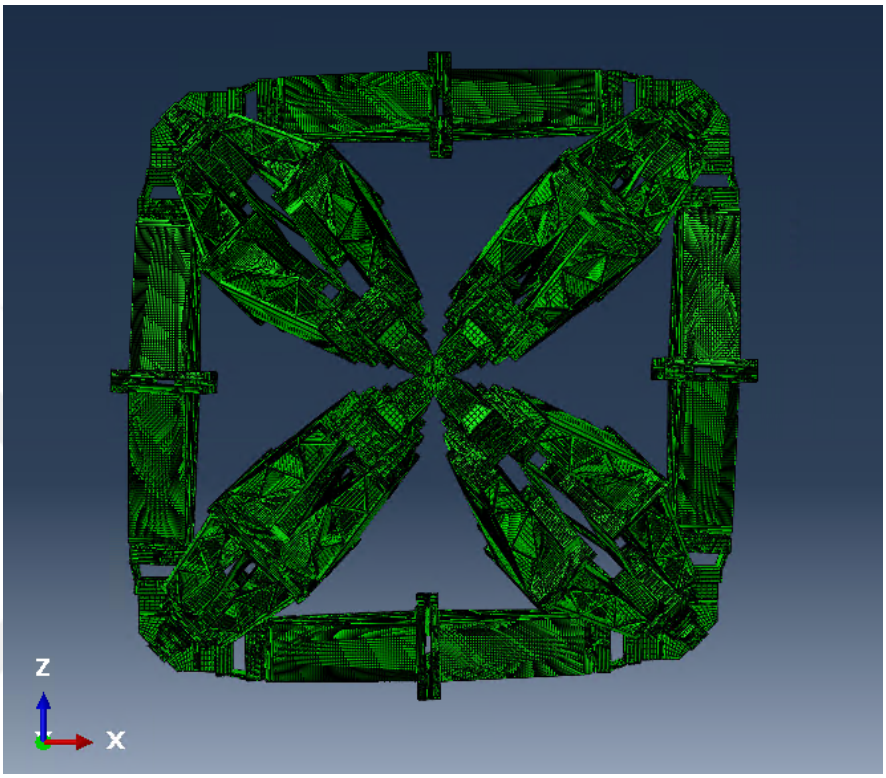


Figure 3.71. 12th mode shape of the octahedron in Figure 3.70 at 102.7 Hz.

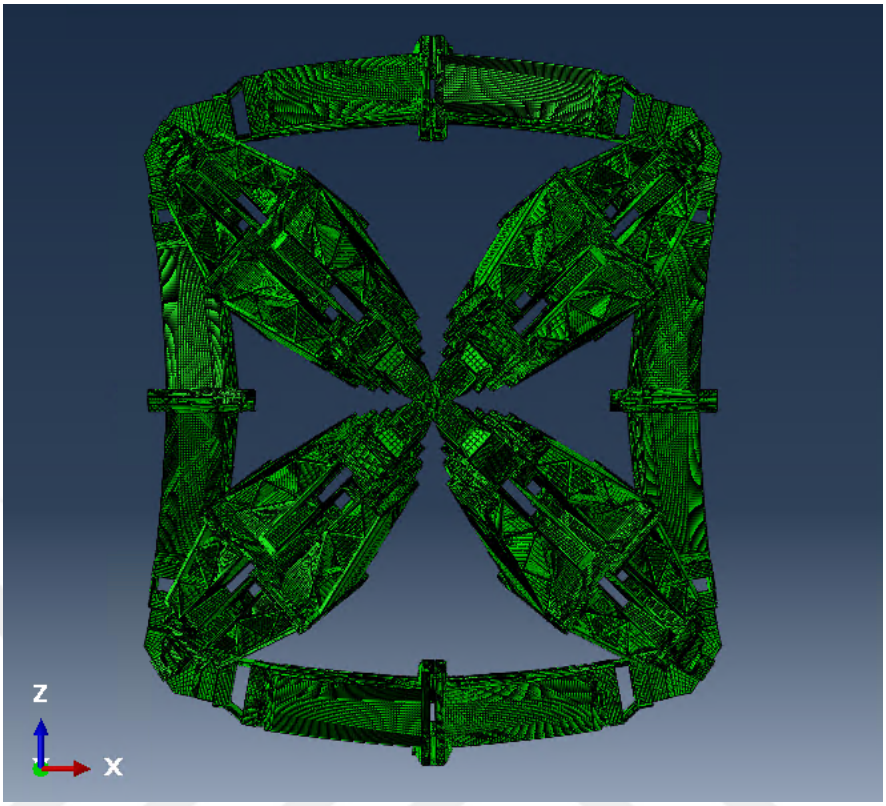
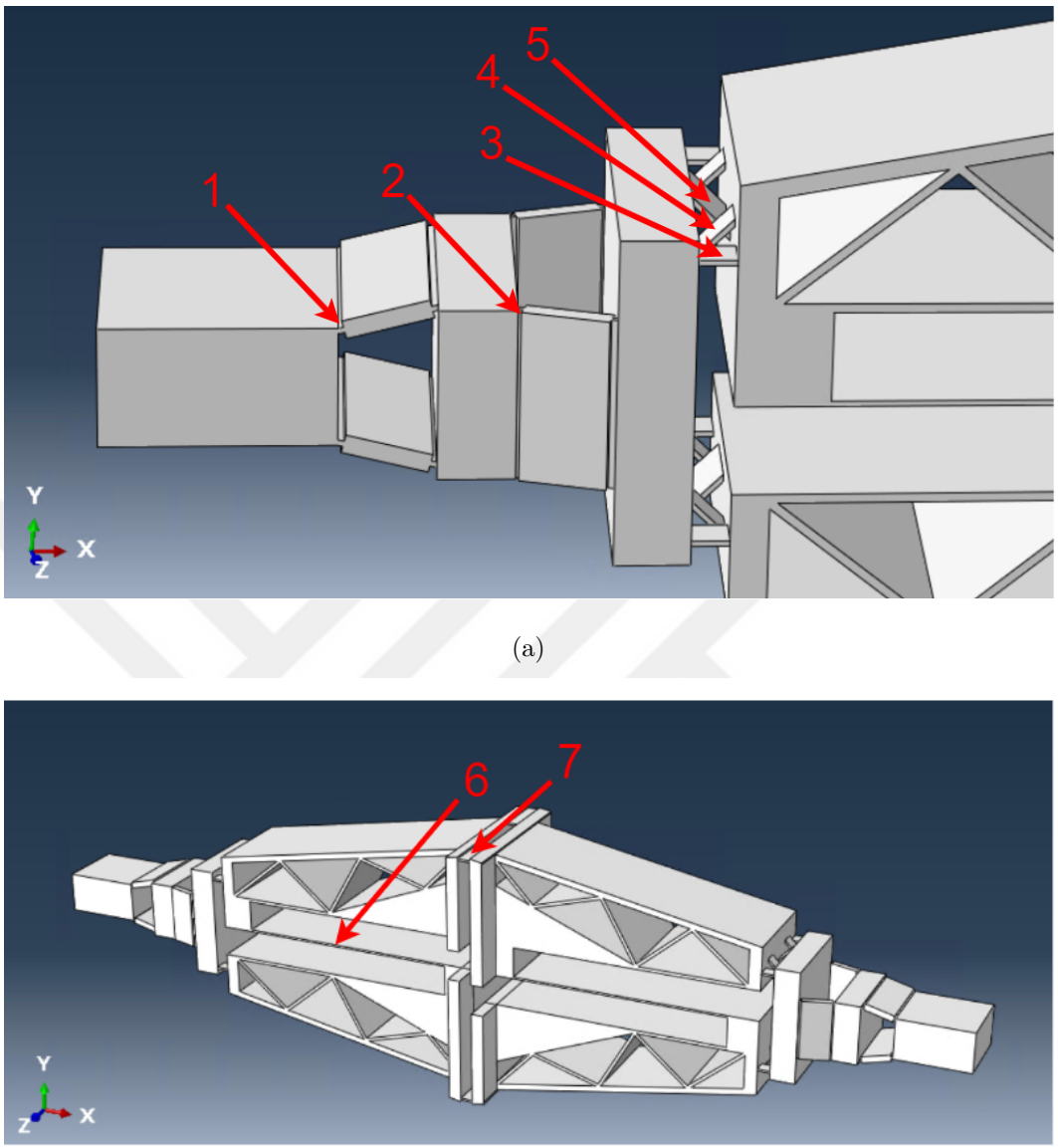


Figure 3.72. 13th mode shape of the octahedron in Figure 3.70 at 630.7 Hz.

3.4. Optimization of the Inertial Amplification Mechanism

In the previous section, several design improvements and topological changes were made to increase the bandwidth of the mechanism. In this section, size optimization will be conducted on the thin flexures that are used in the mechanism.



(a)

(b)

Figure 3.73. Seven different thin flexures of the inertial amplification mechanism. (a) Flexures of the first remote center mechanism, (1), flexures of the second remote center mechanism, (2), horizontal short flexures, (3), cross flexures making a 45° angle with the vertical axis, (4) and (5). (b) Long flexures in the middle, (6), and short flexures between the triangular blocks, (7).

In the final design of the inertial amplification mechanism, there are seven different thin flexures shown in Figure 3.73 which affect the natural frequencies, mode shapes, and hence, the 3D stop band of the octahedron structure. These are the flex-

ures of the first remote center mechanism, (1), the flexures of the second remote center mechanism, (2), the horizontal short flexures, (3), each of two different cross flexures, (4) and (5), the long flexures in the middle, (6), and the short flexures between the triangular blocks, (7). By changing their thicknesses, the lower limit of the stop band of the octahedron structure can be decreased and the upper one can be increased. Certainly, there are lots of other dimensions in the mechanism that can increase the frequency ratio. However, in this thesis, it is aimed to maximize the frequency ratio by optimizing the thicknesses of these seven flexures.

In the optimization process, the shell model of the octahedron structure is used instead of the solid model. The shell model makes it possible to change the thicknesses of the flexures parametrically and shorten the analysis time. In Table 3.8, the natural frequencies of the octahedron with shell elements are given. Notice that the frequencies in Table 3.8 are slightly lower than the ones in Table 3.7. However, the ratio ω_{13}/ω_{12} does not change much (6.14 vs. 6.21). Run time comparison of the solid and shell models is given in Table 3.9. It can be seen that the run time for the model with shell elements is order of magnitude less than the one with solid elements.

Table 3.8. First 40 non-zero natural frequencies of the octahedron structure with shell elements imposed to free boundary conditions.

Natural frequencies	Frequency (Hz)	Natural frequencies	Frequency (Hz)
ω_1	70.37	ω_{21}	672.8
ω_2	74.58	ω_{22}	673.1
ω_3	74.92	ω_{23}	678.2
ω_4	75.14	ω_{24}	682.1
ω_5	81.22	ω_{25}	683.3
ω_6	81.57	ω_{26}	683.8
ω_7	81.59	ω_{27}	740.2
ω_8	91.81	ω_{28}	754.0
ω_9	92.26	ω_{29}	755.3
ω_{10}	92.29	ω_{30}	756.9
ω_{11}	96.15	ω_{31}	850.2
ω_{12}	96.25	ω_{32}	851.6
ω_{13}	598.0	ω_{33}	852.6
ω_{14}	598.1	ω_{34}	941.3
ω_{15}	598.6	ω_{35}	942.8
ω_{16}	640.4	ω_{36}	943.0
ω_{17}	640.7	ω_{37}	943.6
ω_{18}	640.8	ω_{38}	947.9
ω_{19}	659.9	ω_{39}	948.7
ω_{20}	661.1	ω_{40}	949.9

Table 3.9. Run time comparison of solid and shell models of the octahedron structure.

Solid model	Shell model
6 h 29 min 47 sec	15 min 48 sec

The variables of the optimization process are determined as follows: x_1 is the thickness of the flexures of both outer and inner remote center flexure mechanisms, (1) and (2), x_2 is the thickness of the horizontal flexures, (3), x_3 is the thickness of the cross flexures, (4) and (5), and x_4 is the thickness of the short flexures in the middle, (7).

The thickness of the long flexures in the middle, (6), is not taken as one of the optimization variables. Instead, it is kept thick enough such that its mode shapes shown in Figures 3.30 and 3.31 do not appear within the stop band. The thickness of the long flexure is directly proportional to its natural frequency at these modes. Therefore, after the optimization process, the thickness of these parts is chosen such that their mode shapes are located just above the upper limit of the stop band. Hence, as the thickness of the long flexures are decreased, the lower limit of the stop band is expected to decrease more effectively than the upper one, resulting in a higher frequency ratio.

At the beginning of the optimization process, the thicknesses of all the flexures are decreased from 0.3 mm to 0.15 mm. When the thicknesses of the seven flexures are reduced to half, the lower limit of the stop band of the octahedron, ω_{12}, becomes 39.60 Hz, and the upper limit of the stop band of the octahedron, ω_{13}, becomes 469.0 Hz. Hence, the frequency ratio dramatically increases from 6.14 to 11.84.

Using the Latin hypercube sampling method [75, 76], 90 different trials between 0.1 and 0.2 are made for these four design variables. The numerical results show that maximum values of frequency ratio are obtained when x_1 is between 0.14 and 0.17, and the other variables are around 0.1, which is their lower limit. In order to obtain the

global maximum of the search space, the lower limit is relaxed for these three variables and selected as 0.05. Then, another 30 data points are determined with the Latin hypercube sampling method for a narrower search space: x_1 is between 0.14 and 0.17, x_2 is between 0.05 and 0.14, x_3 is between 0.05 and 0.13, x_4 is between 0.05 and 0.12. 30 data points are given in Table 3.10.

Table 3.10. 30 data points with frequency ratios in descending order determined with the Latin hypercube sampling method for the following search space: x_1 is between 0.14 and 0.17, x_2 is between 0.05 and 0.14, x_3 is between 0.05 and 0.13, x_4 is between 0.05 and 0.12.

x_1 (mm)	x_2 (mm)	x_3 (mm)	x_4 (mm)	ω_{12} (Hz)	ω_{13} (Hz)	ω_{13}/ω_{12}
0.1513	0.0857	0.0943	0.0781	34.676	462.01	13.3236
0.1451	0.0676	0.0836	0.0809	33.145	440.34	13.2853
0.1663	0.1203	0.1017	0.0916	39.108	516.12	13.1973
0.1407	0.0989	0.0970	0.0753	32.369	426.81	13.1858
0.1593	0.1246	0.0697	0.0972	37.215	489.56	13.1549
0.1589	0.1043	0.0675	0.0764	36.44	479.30	13.1531
0.1572	0.0710	0.0895	0.0733	35.865	471.27	13.1401
0.1546	0.1332	0.0599	0.0964	35.981	472.48	13.1314
0.1672	0.1173	0.0752	0.0921	39.226	514.02	13.1041
0.1622	0.0733	0.0562	0.0868	37.406	489.43	13.0843
0.1530	0.0779	0.1278	0.1009	36.335	474.8	13.0673
0.1449	0.1305	0.1155	0.0881	34.234	446.04	13.0292
0.1636	0.0976	0.0623	0.1031	38.403	500.32	13.0281
0.1612	0.1360	0.1090	0.1091	38.648	503.33	13.0234
0.1467	0.0893	0.1206	0.0691	33.785	439.59	13.0114
0.1535	0.0584	0.1079	0.1109	36.514	474.06	12.9830
0.1489	0.0947	0.1034	0.1080	35.509	459.26	12.9336
0.1560	0.0808	0.1191	0.1161	37.608	485.21	12.9018
0.1604	0.0870	0.0543	0.1193	38.101	488.26	12.8149

0.1427	0.1387	0.0813	0.1053	34.124	436.17	12.7819
0.1699	0.1097	0.0869	0.1136	40.685	519.76	12.7752
0.1495	0.1031	0.0517	0.0653	33.595	419.8	12.4959
0.1436	0.0524	0.0731	0.0624	32.03	395.75	12.3556
0.1682	0.0541	0.1114	0.0839	39.209	483.16	12.3227
0.1658	0.0645	0.1269	0.0669	38.393	441.14	11.4901
0.1414	0.1128	0.0648	0.0581	31.728	361.04	11.379s2
0.1559	0.0751	0.0915	0.0616	35.343	393.52	11.1343
0.1503	0.1151	0.0987	0.0557	34.065	342.11	10.0428
0.1476	0.0604	0.0775	0.0501	32.807	294.2	8.9676
0.1647	0.1274	0.1226	0.0544	38.202	332.46	8.7027

Examining Table 3.10, one can see that the variables x_1 and x_4 converge to specific values while x_2 and x_3 change over a wider range for the highest frequency ratios. Using the computational method Smoothed-particle hydrodynamics [77–79], a surface plot can be obtained for $x_1 = 0.15$ and $x_4 = 0.08$ while x_2 and x_3 are varied. In Figure 3.74, the surface plot is given that x_2 is between 0.05 and 0.14, and x_3 is between 0.05 and 0.13.

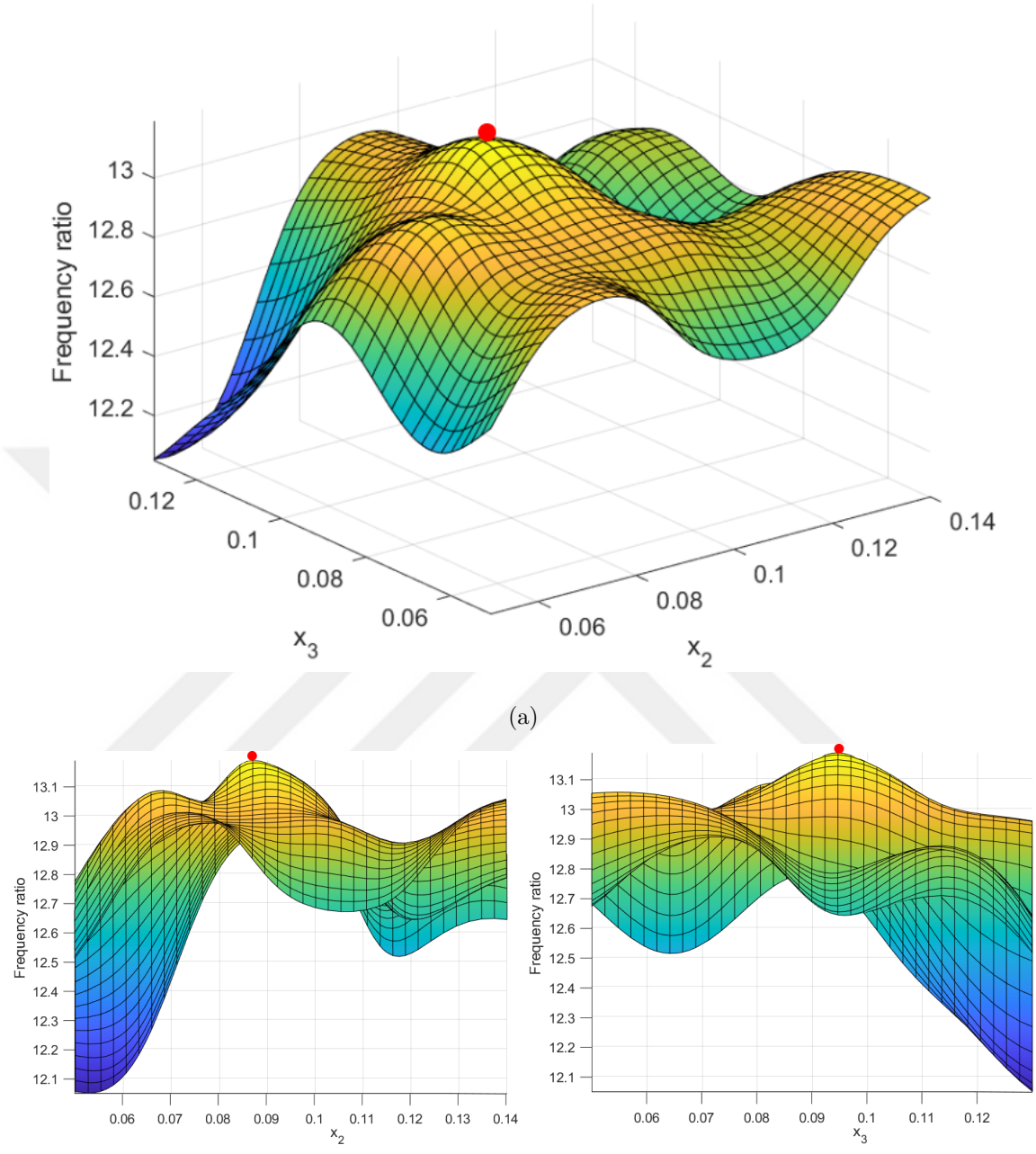


Figure 3.74. Surface plot of data given in Table 3.10 with Smoothed-particle hydrodynamics method for $x_1 = 0.15$ and $x_4 = 0.08$. The red dots show the maximum point on the surfaces. (a) Isometric view. (b) Side view such that x_2 is the horizontal axis. (c) Side view such that x_3 is the horizontal axis.

In Figure 3.74, the global maximum of the surface can be seen clearly. However, there are several other local maxima near the global maximum. Since this surface

is formed by using the data points in Table 3.10, the global maximum may improve if a gradient based optimization method is utilized around the peak point. Around this peak, a new set of x_1, x_2, x_3 and x_4 is determined in order to find the maximum frequency ratio with the steepest descent method. Considering many peaks in narrow intervals of variables, the step size is chosen as 1%. After two steps of iterations with the steepest descent method, the variables are found as follows: $x_1 = 0.1542$, $x_2 = 0.08417$, $x_3 = 0.08958$, and $x_4 = 0.07940$. The lower limit of the stop band, ω_{12}, becomes 35.29 Hz and the upper limit, ω_{13}, becomes 471.0 Hz. Consequently, ω_{13}/ω_{12} is obtained as 13.35. Finally, decreasing the thickness of the long flexures, (6), from 0.15 mm to 0.115 mm causes ω_{12} to decrease to 34.41 Hz, and also ω_{13} to decrease to 469.6 Hz, leading to the ratio ω_{13}/ω_{12} of 13.65. The mode shapes at the lower and upper limit of the stop band are shown in Figures 3.75 and 3.76, respectively.

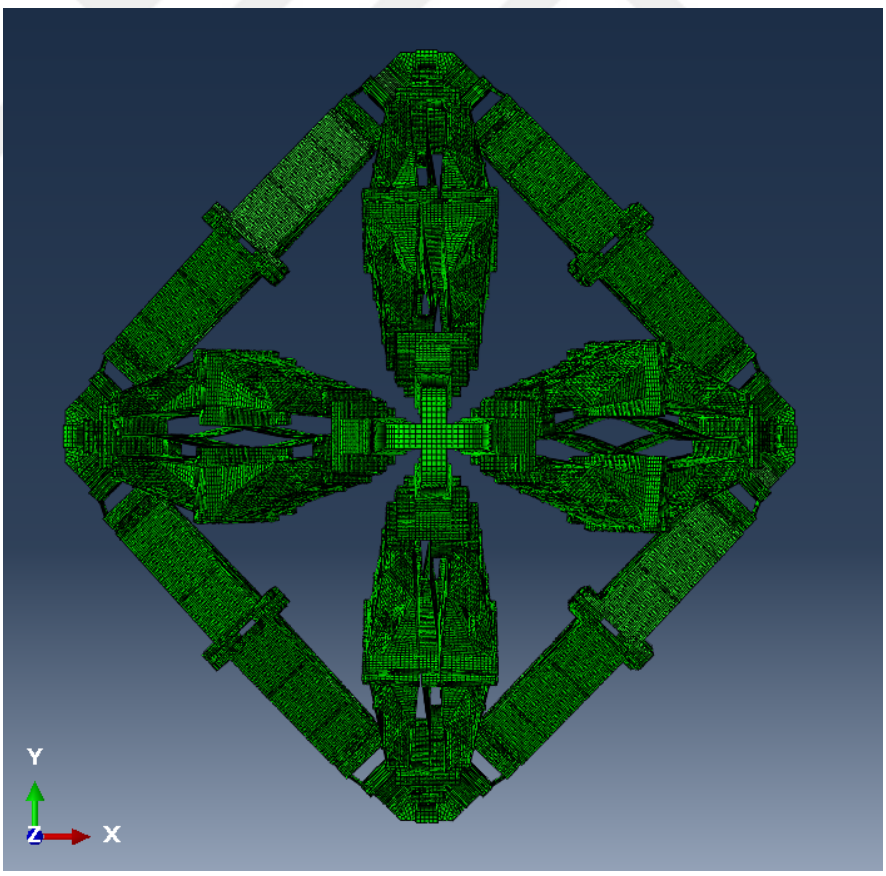


Figure 3.75. 12th mode shape of the final design of the octahedron at 34.41 Hz.

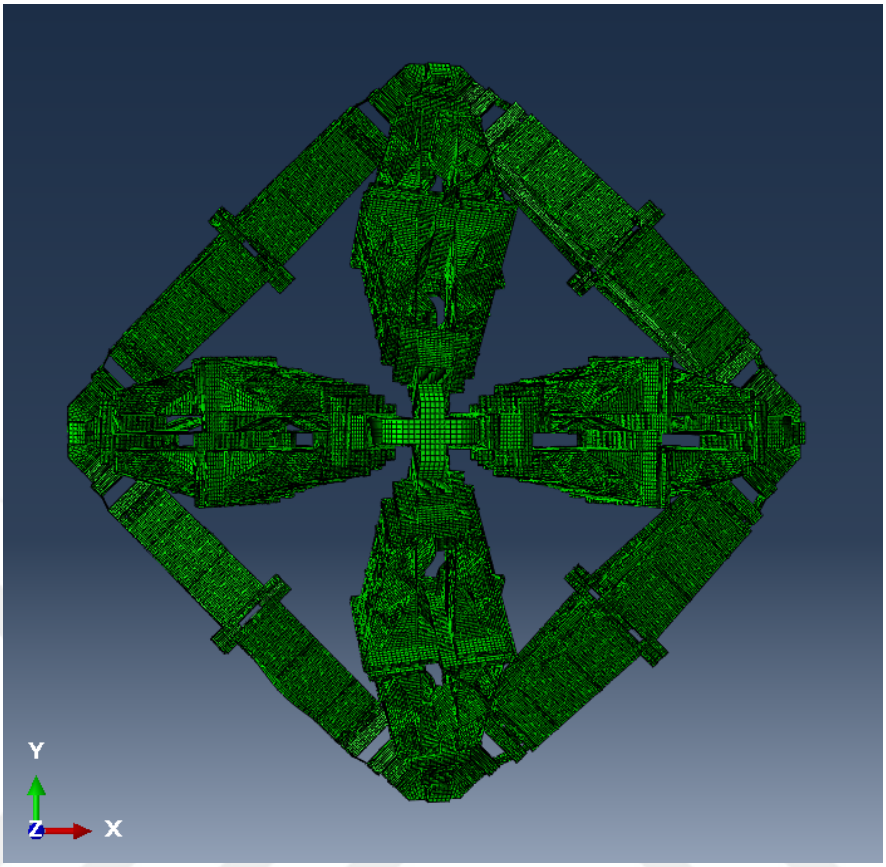


Figure 3.76. 13th mode shape of the final design of the octahedron at 469.6 Hz.

Finally, a 3x2 periodic structure is formed by using optimized octahedron structure shown in Figure 3.77. There are 72 modes up to 39.76 Hz and the next mode appears at 448.1 Hz. Notice that the stop band in the 3x2 periodic structure has a upper to lower limit ratio of 11.27, while the building block octahedron has a frequency ratio of 13.65. Hence, periodic assembly of the octahedrons slightly reduce the stop band frequency range.

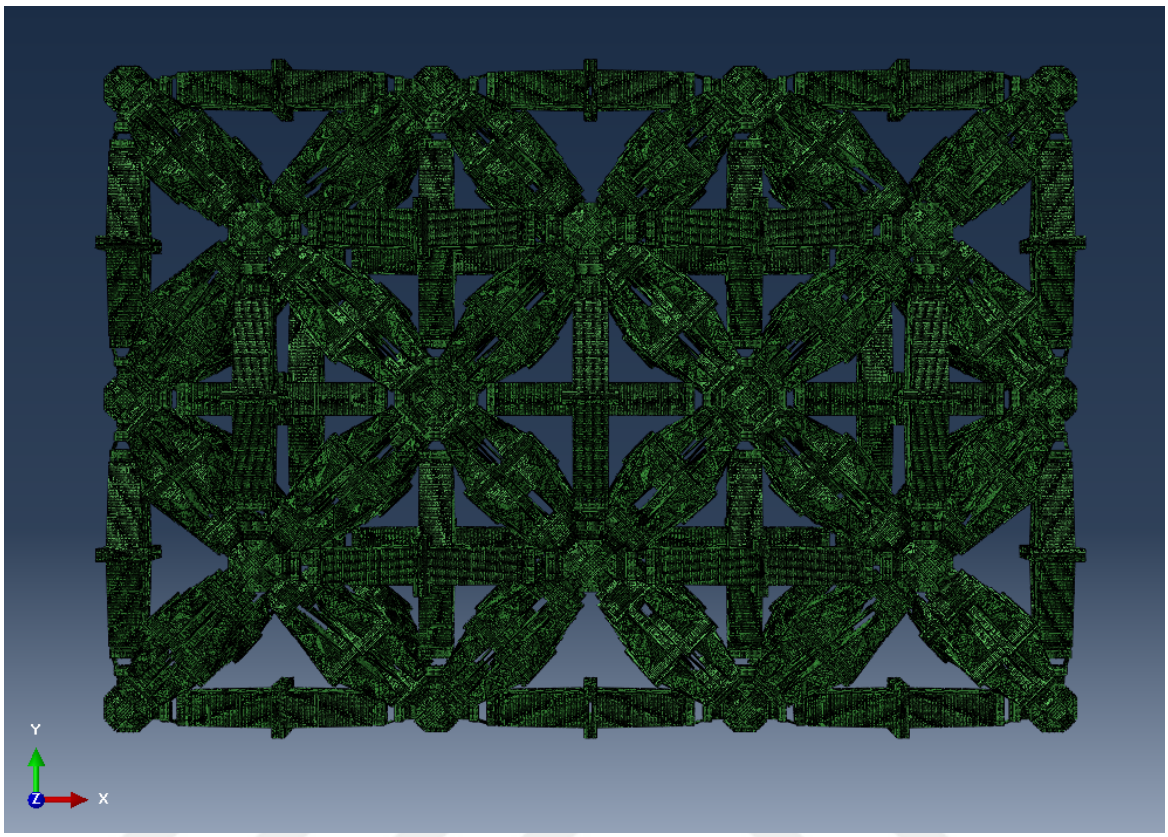


Figure 3.77. 3x2 periodic structure formed with optimized octahedron structure.

4. CONCLUSION

Using the novel inertial amplification method, an ultrawide stop band is obtained in three dimensions. First, an inertial amplification mechanism is designed suitable for 3D assembly. Since 3D structures can be subject to both in-plane and out-of-plane bending loads, spatial remote center flexure mechanisms are used at the ends of the mechanism. They are constituted of two stages allowing rotation around two axes orthogonal to each other. Using the inertial amplification mechanisms, an octahedron is formed. Between the 12th and 13th modes of the octahedron, a wide frequency gap is obtained and its width is quantified by the ratio of the upper limit of the stop band to the lower one, ω_{13}/ω_{12}. In this thesis, this frequency ratio is aimed to be maximized. To do that, the mode shapes and natural frequencies of a single inertial amplification mechanism and the octahedron structure are examined. By imposing different boundary conditions to a single mechanism, mode shapes are identified. While the first natural frequency corresponding to the first mode shape is the same, higher modes differ as the boundary conditions change. Moreover, even small dimensional changes in the mechanism can affect natural frequencies and change the mode shape at the upper limit of the stop band of the octahedron. With design improvements and topological changes, the 12th natural frequency of the octahedron, ω_{12}, is aimed to be minimized, and the 13th natural frequency, ω_{13}, is aimed to be maximized. For that purpose, the novel cross flexure design is added to the mechanism to increase the torsional, in-plane bending and out-of-plane bending modes of the mechanism. Moreover, the triangular blocks in the middle of the mechanism are hollowed out by supporting them with a truss structure in order to bring their centers of mass closer to the rotation axis of the torsional mode shape motion. In order to increase the natural frequency of the out-of-plane bending motion, the width of the mechanism is increased in the middle with additional blocks and the middle short flexures are divided into two and placed towards the two ends of the widened section in order to increase the out-of-plane bending stiffness. The final design of the inertial amplification mechanism has seven thin flexures which affect the natural frequencies and mode shapes of the

mechanism. Size optimization is conducted on these flexures and the stop band of the octahedron is obtained between 34.41 Hz and 469.6 Hz, resulting in a frequency ratio of 13.65. This frequency ratio is the highest considering all the 3D designs in the literature. Finally, a 3x2 periodic structure is formed by using the optimized octahedrons. It is seen that the stop band of this periodic structure is between 39.76 Hz and 448.1 Hz. Hence, its frequency ratio is 11.27, which is slightly less than the octahedron building block.

REFERENCES

1. Yuksel, O. and C. Yilmaz, "Realization of an Ultrawide Stop Band in a 2-D Elastic Metamaterial with Topologically Optimized Inertial Amplification Mechanisms", *International Journal of Solids and Structures*, Vol. 203, pp. 138–150, 2020.

2. Acar, G. and C. Yilmaz, "Experimental and Numerical Evidence for the Existence of Wide and Deep Phononic Gaps Induced by Inertial Amplification in Two-Dimensional Solid Structures", *Journal of Sound and Vibration*, Vol. 332, No. 24, pp. 6389–6404, 2013.

3. Yuksel, O. and C. Yilmaz, "Shape Optimization of Phononic Band Gap Structures Incorporating Inertial Amplification Mechanisms", *Journal of Sound and Vibration*, Vol. 355, pp. 232–245, 2015.

4. Taniker, S. and C. Yilmaz, "Generating Ultra Wide Vibration Stop Bands by a Novel Inertial Amplification Mechanism Topology with Flexure Hinges", *International Journal of Solids and Structures*, Vol. 106-107, pp. 129–138, 2017.

5. Taniker, S. and C. Yilmaz, "Design, Analysis and Experimental Investigation of Three-Dimensional Structures with Inertial Amplification Induced Vibration Stop Bands", *International Journal of Solids and Structures*, Vol. 72, pp. 88–97, 2015.

6. Economou, E. N. and M. Sigalas, "Stop Bands for Elastic Waves in Periodic Composite Materials", *The Journal of the Acoustical Society of America*, Vol. 95, No. 4, pp. 1734–1740, 1994.

7. Kafesaki, M., M. M. Sigalas and E. Economou, "Elastic Wave Band Gaps in 3-D Periodic Polymer Matrix Composites", *Solid State Communications*, Vol. 96, No. 5, pp. 285–289, 1995.

8. Kushwaha, M. S., "Classical Band Structure of Periodic Elastic Composites", *In-*

ternational Journal of Modern Physics B, Vol. 10, No. 09, pp. 977–1094, 1996.

9. Kushwaha, M., B. Djafari-Rouhani, L. Dobrzynski and J. O. Vasseur, "Sonic Stop-Bands for Cubic Arrays of Rigid Inclusions in Air", *The European Physical Journal B-Condensed Matter and Complex Systems*, Vol. 3, No. 2, pp. 155–161, 1998.

10. Sainidou, R., N. Stefanou and A. Modinos, "Formation of Absolute Frequency Gaps in Three-Dimensional Solid Phononic Crystals", *Physical Review B*, Vol. 66, No. 21, p. 212301, 2002.

11. Jensen, J. S., "Phononic Band Gaps and Vibrations in One- and Two-Dimensional Mass-Spring Structures", *Journal of Sound and Vibration*, Vol. 266, No. 5, pp. 1053–1078, 2003.

12. Goffaux, C. and J. Sánchez-Dehesa, "Two-Dimensional Phononic Crystals Studied Using a Variational Method: Application to Lattices of Locally Resonant Materials", *Physical Review B*, Vol. 67, No. 14, p. 144301, 2003.

13. Wang, G., J. Wen and X. Wen, "Quasi-One-Dimensional Phononic Crystals Studied Using the Improved Lumped-Mass Method: Application to Locally Resonant Beams with Flexural Wave Band Gap", *Physical Review B*, Vol. 71, No. 10, p. 104302, 2005.

14. Halkjær, S., O. Sigmund and J. S. Jensen, "Maximizing Band Gaps in Plate Structures", *Structural and Multidisciplinary Optimization*, Vol. 32, No. 4, pp. 263–275, 2006.

15. Jensen, J. S. and N. L. Pedersen, "On Maximal Eigenfrequency Separation in Two-Material Structures: the 1D and 2D Scalar Cases", *Journal of Sound and Vibration*, Vol. 289, No. 4-5, pp. 967–986, 2006.

16. Wang, G., X. Wen, J. Wen and Y. Liu, "Quasi-One-Dimensional Periodic Structure with Locally Resonant Band Gap", *Journal of Applied Mechanics*, Vol. 73, No. 1,

pp. 167–170, 2006.

17. Yu, D., Y. Liu, H. Zhao, G. Wang and J. Qiu, "Flexural Vibration Band Gaps in Euler-Bernoulli Beams with Locally Resonant Structures with Two Degrees of Freedom", *Physical Review B*, Vol. 73, No. 6, p. 064301, 2006.

18. Chen, J. J., H. L. W. Chan and J. C. Cheng, "Large One-Dimensional Band Gaps in Three-Component Phononic Crystals Plates", *Physics Letters A*, Vol. 366, No. 4-5, pp. 493–496, 2007.

19. Shen, H., J. Wen, D. Yu and X. Wen, "The Vibrational Properties of a Periodic Composite Pipe in 3D Space", *Journal of Sound and Vibration*, Vol. 328, No. 1-2, pp. 57–70, 2009.

20. Soliman, Y. M., M. F. Su, Z. C. Leseman, C. M. Reinke, I. El-Kady and R. H. Olsson III, "Phononic Crystals Operating in the Gigahertz Range with Extremely Wide Band Gaps", *Applied Physics Letters*, Vol. 97, No. 19, p. 193502, 2010.

21. Yu, D., J. Wen, H. Shen, Y. Xiao and X. Wen, "Propagation of Flexural Wave in Periodic Beam on Elastic Foundations", *Physics Letters A*, Vol. 376, No. 4, pp. 626–630, 2012.

22. Badreddine Assouar, M. and M. Oudich, "Enlargement of a Locally Resonant Sonic Band Gap by Using Double-Sides Stubbed Phononic Plates", *Applied Physics Letters*, Vol. 100, No. 12, p. 123506, 2012.

23. Olhoff, N., B. Niu and G. Cheng, "Optimum Design of Band-Gap Beam Structures", *International Journal of Solids and Structures*, Vol. 49, No. 22, pp. 3158–3169, 2012.

24. Yin, J., J. Huang, S. Zhang, H. W. Zhang and B. S. Chen, "Ultrawide Low Frequency Band Gap of Phononic Crystal in Nacreous Composite Material", *Physics Letters A*, Vol. 378, No. 32-33, pp. 2436–2442, 2014.

25. Wang, P., F. Casadei, S. H. Kang and K. Bertoldi, "Locally Resonant Band Gaps in Periodic Beam Lattices by Tuning Connectivity", *Physical Review B*, Vol. 91, No. 2, p. 020103, 2015.

26. Trainiti, G., J. J. Rimoli and M. Ruzzene, "Wave Propagation in Periodically Undulated Beams and Plates", *International Journal of Solids and Structures*, Vol. 75, pp. 260–276, 2015.

27. Bacigalupo, A. and L. Gambarotta, "Simplified Modelling of Chiral Lattice Materials with Local Resonators", *International Journal of Solids and Structures*, Vol. 83, pp. 126–141, 2016.

28. Bao, J., Z. Shi and H. Xiang, "Dynamic Responses of a Structure with Periodic Foundations", *Journal of Engineering Mechanics*, Vol. 138, No. 7, pp. 761–769, 2012.

29. Xiang, H. J., Z. F. Shi, S. J. Wang and Y. L. Mo, "Periodic Materials-Based Vibration Attenuation in Layered Foundations: Experimental Validation", *Smart Materials and Structures*, Vol. 21, No. 11, p. 112003, 2012.

30. Shi, Z., Z. Cheng and H. Xiang, "Seismic Isolation Foundations with Effective Attenuation Zones", *Soil Dynamics and Earthquake Engineering*, Vol. 57, pp. 143–151, 2014.

31. Liu, X., Z. Shi, Y. L. Mo and Z. Cheng, "Effect of Initial Stress on Attenuation Zones of Layered Periodic Foundations", *Engineering Structures*, Vol. 121, pp. 75–84, 2016.

32. Oh, J. H., S. Qi, Y. Y. Kim and B. Assouar, "Elastic Metamaterial Insulator for Broadband Low-Frequency Flexural Vibration Shielding", *Physical Review Applied*, Vol. 8, No. 5, p. 054034, 2017.

33. Yuksel, O. and C. Yilmaz, "Size and Topology Optimization of Inertial Amplifi-

cation Induced Phononic Band Gap Structures", *ASME International Mechanical Engineering Congress and Exposition*, Vol. 58486, p. V013T01A007, American Society of Mechanical Engineers, 2017.

34. Dianlong, Y., L. Yaozong, W. Gang, C. Li, Q. Jing *et al.*, "Low Frequency Torsional Vibration Gaps in the Shaft with Locally Resonant Structures", *Physics Letters A*, Vol. 348, No. 3-6, pp. 410–415, 2006.

35. Coffy, E., T. Lavergne, M. Addouche, S. Euphrasie, P. Vairac and A. Khelif, "Ultra-Wide Acoustic Band Gaps in Pillar-Based Phononic Crystal Strips", *Journal of Applied Physics*, Vol. 118, No. 21, p. 214902, 2015.

36. Li, J. and S. Li, "Generating Ultra Wide Low-Frequency Gap for Transverse Wave Isolation via Inertial Amplification Effects", *Physics Letters A*, Vol. 382, No. 5, pp. 241–247, 2018.

37. Jia, G. and Z. Shi, "A New Seismic Isolation System and Its Feasibility Study", *Earthquake Engineering and Engineering Vibration*, Vol. 9, No. 1, pp. 75–82, 2010.

38. Cheng, Z. and Z. Shi, "Novel Composite Periodic Structures with Attenuation Zones", *Engineering Structures*, Vol. 56, pp. 1271–1282, 2013.

39. Yan, Y., A. Laskar, Z. Cheng, F. Menq, Y. Tang, Y. L. Mo and Z. Shi, "Seismic Isolation of Two Dimensional Periodic Foundations", *Journal of Applied Physics*, Vol. 116, No. 4, p. 044908, 2014.

40. Jiang, S., H. Hu and V. Laude, "Ultra-Wide Band Gap in Two-Dimensional Phononic Crystal with Combined Convex and Concave Holes", *Physica Status Solidi (RRL)–Rapid Research Letters*, Vol. 12, No. 2, p. 1700317, 2018.

41. Wen, G., H. Ou and J. Liu, "Ultra-Wide Band Gap in a Two-Dimensional Phononic Crystal with Hexagonal Lattices", *Materials Today Communications*, Vol. 24, p. 100977, 2020.

42. Bilal, O. R. and M. I. Hussein, "Ultrawide Phononic Band Gap for Combined in-Plane and out-of-Plane Waves", *Physical Review E*, Vol. 84, No. 6, p. 065701, 2011.

43. Shi, Z. and J. Huang, "Feasibility of Reducing Three-Dimensional Wave Energy by Introducing Periodic Foundations", *Soil Dynamics and Earthquake Engineering*, Vol. 50, pp. 204–212, 2013.

44. Yan, Y., A. Laskar, Z. Cheng, F. Menq, Y. Tang, Y. L. Mo and Z. Shi, "Periodic Materials-Based 3D Seismic Base Isolators for Nuclear Power Plants", *Pressure Vessels and Piping Conference*, Vol. 46070, p. V008T08A008, American Society of Mechanical Engineers, 2014.

45. Yan, Y., Z. Cheng, F. Menq, Y. L. Mo, Y. Tang and Z. Shi, "Three Dimensional Periodic Foundations for Base Seismic Isolation", *Smart Materials and Structures*, Vol. 24, No. 7, p. 075006, 2015.

46. Yan, Y., W. Witarto, S. J. Wang, Y. L. Mo, K. C. Chang, Y. Tang and M. Ruis, "Periodic Material Based Seismic Isolation for Small Modular Reactors", *Pressure Vessels and Piping Conference*, Vol. 57034, p. V008T08A041, American Society of Mechanical Engineers, 2015.

47. D'Alessandro, L., R. Ardito, F. Braghin and A. Corigliano, "Low Frequency 3D Ultra-Wide Vibration Attenuation via Elastic Metamaterial", *Scientific Reports*, Vol. 9, No. 1, pp. 1–8, 2019.

48. D'Alessandro, L., E. Belloni, R. Ardito, A. Corigliano and F. Braghin, "Modeling and Experimental Verification of an Ultra-Wide Bandgap in 3D Phononic Crystal", *Applied Physics Letters*, Vol. 109, No. 22, p. 221907, 2016.

49. Lu, Y., Y. Yang, J. K. Guest and A. Srivastava, "3-D Phononic Crystals with Ultra-Wide Band Gaps", *Scientific Reports*, Vol. 7, No. 1, pp. 1–14, 2017.

50. Muhammad, "Design and Manufacturing of Monolithic Mechanical Metastructures Governing Ultrawide Low Frequency Three-Dimensional Gandgaps", *Additive Manufacturing*, Vol. 47, 2021.

51. Muhammad, S., S. Wang, F. Li and C. Zhang, "Bandgap Enhancement of Periodic Nonuniform Metamaterial Beams with Inertial Amplification Mechanisms", *Journal of Vibration and Control*, Vol. 26, No. 15-16, pp. 1309–1318, 2020.

52. Muhammad and C. W. Lim, "Phononic Metastructures with Ultrawide Low Frequency Three-Dimensional Bandgaps as Broadband Low Frequency Filter", *Scientific Reports*, Vol. 11, No. 1, pp. 1–11, 2021.

53. Muhammad and C. W. Lim, "Ultrawide Bandgap by 3D Monolithic Mechanical Metastructure for Vibration and Noise Control", *Archives of Civil and Mechanical Engineering*, Vol. 21, No. 2, pp. 1–11, 2021.

54. Yilmaz, C., G. M. Hulbert and N. Kikuchi, "Phononic Band Gaps Induced by Inertial Amplification in Periodic Media", *Physical Review B*, Vol. 76, No. 5, p. 054309, 2007.

55. Yilmaz, C. and G. M. Hulbert, "Theory of Phononic Gaps Induced by Inertial Amplification in Finite Structures", *Physics Letters A*, Vol. 374, No. 34, pp. 3576–3584, 2010.

56. Orta, A. H. and C. Yilmaz, "Inertial Amplification Induced Phononic Band Gaps Generated by a Compliant Axial to Rotary Motion Conversion Mechanism", *Journal of Sound and Vibration*, Vol. 439, pp. 329–343, 2019.

57. Taniker, S. and C. Yilmaz, "Phononic Gaps Induced by Inertial Amplification in BCC and FCC Lattices", *Physics Letters A*, Vol. 377, No. 31-33, pp. 1930–1936, 2013.

58. Taniker, S. and C. Yilmaz, "Inertial Amplification Induced Phononic Band Gaps

in SC and BCC Lattices", *ASME International Mechanical Engineering Congress and Exposition*, Vol. 56437, p. V014T15A046, American Society of Mechanical Engineers, 2013.

59. Schmied, J. U., C. Sugino, A. Bergamini, P. Ermanni, M. Ruzzene and A. Erturk, "Toward Structurally Integrated Locally Resonant Metamaterials for Vibration Attenuation", *Active and Passive Smart Structures and Integrated Systems*, Vol. 10164, No. 4, p. 1016413, 2017.

60. Hou, M., J. H. Wu, S. Cao, D. Guan and Y. Zhu, "Extremely Low Frequency Band Gaps of Beam-Like Inertial Amplification Metamaterials", *Modern Physics Letters B*, Vol. 31, No. 27, p. 1750251, 2017.

61. Adhikari, S. and A. Banerjee, "Enhanced Low-Frequency Vibration Energy Harvesting with Inertial Amplifiers", *Journal of Intelligent Material Systems and Structures*, p. 1045389X211032281, 2021.

62. Li, Y. and W. Zhou, "Bandgap and Vibration Transfer Characteristics of Scissor-Like Periodic Metamaterials", *Journal of Applied Physics*, Vol. 130, No. 2, p. 025103, 2021.

63. Miniaci, M., M. Mazzotti, A. Amendola and F. Fraternali, "Inducing Dispersion Curves with Negative Group Velocity in Inertially Amplified Phononic Crystals through the Application of an External State of Prestress", *XI International Conference on Structural Dynamic, EURODYN 2020*, pp. 612–620, 2020.

64. Miniaci, M., M. Mazzotti, A. Amendola and F. Fraternali, "Effect of Prestress on Phononic Band Gaps Induced by Inertial Amplification", *International Journal of Solids and Structures*, Vol. 216, pp. 156–166, 2021.

65. Shoaib, M., W. Pang and F. Li, "Vibration Reduction of Pipes Conveying Fluid with Periodic Inertial Amplification Mechanisms", *Waves in Random and Complex*

Media, pp. 1–16, 2021.

66. Banerjee, A., S. Adhikari and M. I. Hussein, "Inertial Amplification Band-Gap Generation by Coupling a Levered Mass with a Locally Resonant Mass", *International Journal of Mechanical Sciences*, Vol. 207, p. 106630, 2021.

67. Barys, M. and R. Zalewski, "Analysis of Inertial Amplification Mechanism with Smart Spring-Damper for Attenuation of Beam Vibrations", *MATEC Web of Conferences*, Vol. 157, p. 03002, EDP Sciences, 2018.

68. Cheng, Z., A. Palermo, Z. Shi and A. Marzani, "Enhanced Tuned Mass Damper Using an Inertial Amplification Mechanism", *Journal of Sound and Vibration*, Vol. 475, p. 115267, 2020.

69. Li, J., P. Yang and S. Li, "Phononic Band Gaps by Inertial Amplification Mechanisms in Periodic Composite Sandwich Beam with Lattice Truss Cores", *Composite Structures*, Vol. 231, p. 111458, 2020.

70. Barys, M., J. S. Jensen and N. M. Frandsen, "Efficient Attenuation of Beam Vibrations by Inertial Amplification", *European Journal of Mechanics-A/Solids*, Vol. 71, pp. 245–257, 2018.

71. Mu, D., H. Shu, L. Zhao and S. An, "A Review of Research on Seismic Metamaterials", *Advanced Engineering Materials*, Vol. 22, No. 4, p. 1901148, 2020.

72. Zhou, J., L. Dou, K. Wang, D. Xu and H. Ouyang, "A Nonlinear Resonator with Inertial Amplification for Very Low-Frequency Flexural Wave Attenuations in Beams", *Nonlinear Dynamics*, Vol. 96, No. 1, pp. 647–665, 2019.

73. Martinez, J. A. I., J. Moughames, G. Ulliac, M. Kadic and V. Laude, "Three-Dimensional Phononic Crystal with Ultra-Wide Bandgap at Megahertz Frequencies", *Applied Physics Letters*, Vol. 118, No. 6, p. 063507, 2021.

74. Yilmaz, C. and N. Kikuchi, "Analysis and Design of Passive Band-Stop Filter-Type Vibration Isolators for Low-Frequency Applications", *Journal of Sound and Vibration*, Vol. 291, No. 3-5, pp. 1004–1028, 2006.

75. Loh, W.-L., "On Latin Hypercube Sampling", *The Annals of Statistics*, Vol. 24, No. 5, pp. 2058–2080, 1996.

76. Stein, M., "Large Sample Properties of Simulations Using Latin Hypercube Sampling", *Technometrics*, Vol. 29, No. 2, pp. 143–151, 1987.

77. Monaghan, J. J., "Smoothed Particle Hydrodynamics", *Annual Review of Astronomy and Astrophysics*, Vol. 30, No. 1, pp. 543–574, 1992.

78. Monaghan, J. J., "Smoothed Particle Hydrodynamics", *Reports on Progress in Physics*, Vol. 68, No. 8, p. 1703, 2005.

79. Liu, M. and G. Liu, "Smoothed Particle Hydrodynamics (SPH): an Overview and Recent Developments", *Archives of Computational Methods in Engineering*, Vol. 17, No. 1, pp. 25–76, 2010.

APPENDIX A: ELSEVIER LICENSE NUMBER 5236891087000

ELSEVIER LICENSE
TERMS AND CONDITIONS

Jan 27, 2022

This Agreement between bogazici university -- sedef nisan otlu ("You") and Elsevier ("Elsevier") consists of your license details and the terms and conditions provided by Elsevier and Copyright Clearance Center.

License Number	5236891087000
License date	Jan 27, 2022
Licensed Content Publisher	Elsevier
Licensed Content Publication	International Journal of Solids and Structures
Licensed Content Title	Realization of an ultrawide stop band in a 2-D elastic metamaterial with topologically optimized inertial amplification mechanisms
Licensed Content Author	Osman Yuksel,Cetin Yilmaz
Licensed Content Date	Oct 15, 2020
Licensed Content Volume	203
Licensed Content Issue	n/a
Licensed Content Pages	13
Start Page	138
End Page	150
Type of Use	reuse in a thesis/dissertation
Portion	figures/tables/illustrations
Number of figures/tables/illustrations	4
Format	both print and electronic
Are you the author of this Elsevier article?	No
Will you be translating?	No
Title	ULTRAWIDE STOP BAND IN A 3D ELASTIC METAMATERIAL WITH INERTIAL AMPLIFICATION MECHANISMS HAVING CROSS FLEXURE HINGES
Institution name	BOGAZICI UNIVERSITY
Expected presentation date	Jan 2022

Figure A.1. Elsevier license of [1] for Figures 2.1, 3.6, 3.13 and 3.14.

APPENDIX B: ELSEVIER LICENSE NUMBER 5236891191376

ELSEVIER LICENSE
TERMS AND CONDITIONS

Jan 27, 2022

This Agreement between bogazici university -- sedef nisan otlu ("You") and Elsevier ("Elsevier") consists of your license details and the terms and conditions provided by Elsevier and Copyright Clearance Center.

License Number	5236891191376
License date	Jan 27, 2022
Licensed Content Publisher	Elsevier
Licensed Content Publication	Journal of Sound and Vibration
Licensed Content Title	Experimental and numerical evidence for the existence of wide and deep phononic gaps induced by inertial amplification in two-dimensional solid structures
Licensed Content Author	G. Acar,C. Yilmaz
Licensed Content Date	Nov 25, 2013
Licensed Content Volume	332
Licensed Content Issue	24
Licensed Content Pages	16
Start Page	6389
End Page	6404
Type of Use	reuse in a thesis/dissertation
Portion	figures/tables/illustrations
Number of figures/tables/illustrations	4
Format	both print and electronic
Are you the author of this Elsevier article?	No
Will you be translating?	No
Title	ULTRAWIDE STOP BAND IN A 3D ELASTIC METAMATERIAL WITH INERTIAL AMPLIFICATION MECHANISMS HAVING CROSS FLEXURE HINGES
Institution name	BOGAZICI UNIVERSITY
Expected presentation date	Jan 2022

Figure B.1. Elsevier license of [2] for Figures 3.1, 3.2, 3.3 and 3.4.

APPENDIX C: ELSEVIER LICENSE NUMBER 5236891010401

ELSEVIER LICENSE
TERMS AND CONDITIONS

Jan 27, 2022

This Agreement between bogazici university -- sedef nisan otlu ("You") and Elsevier ("Elsevier") consists of your license details and the terms and conditions provided by Elsevier and Copyright Clearance Center.

License Number	5236891010401
License date	Jan 27, 2022
Licensed Content Publisher	Elsevier
Licensed Content Publication	Journal of Sound and Vibration
Licensed Content Title	Shape optimization of phononic band gap structures incorporating inertial amplification mechanisms
Licensed Content Author	Osman Yuksel,Cetin Yilmaz
Licensed Content Date	Oct 27, 2015
Licensed Content Volume	355
Licensed Content Issue	n/a
Licensed Content Pages	14
Start Page	232
End Page	245
Type of Use	reuse in a thesis/dissertation
Portion	figures/tables/illustrations
Number of figures/tables/illustrations	1
Format	both print and electronic
Are you the author of this Elsevier article?	No
Will you be translating?	No
Title	ULTRAWIDE STOP BAND IN A 3D ELASTIC METAMATERIAL WITH INERTIAL AMPLIFICATION MECHANISMS HAVING CROSS FLEXURE HINGES
Institution name	BOGAZICI UNIVERSITY
Expected presentation date	Jan 2022

Figure C.1. Elsevier license of [3] for Figure 3.5.

APPENDIX D: ELSEVIER LICENSE NUMBER 5236890632592

ELSEVIER LICENSE
TERMS AND CONDITIONS

Jan 27, 2022

This Agreement between bogazici university -- sedef nisan otlu ("You") and Elsevier ("Elsevier") consists of your license details and the terms and conditions provided by Elsevier and Copyright Clearance Center.

License Number	5236890632592
License date	Jan 27, 2022
Licensed Content Publisher	Elsevier
Licensed Content Publication	International Journal of Solids and Structures
Licensed Content Title	Generating ultra wide vibration stop bands by a novel inertial amplification mechanism topology with flexure hinges
Licensed Content Author	S. Taniker,C. Yilmaz
Licensed Content Date	Feb 1, 2017
Licensed Content Volume	106
Licensed Content Issue	n/a
Licensed Content Pages	10
Start Page	129
End Page	138
Type of Use	reuse in a thesis/dissertation
Portion	figures/tables/illustrations
Number of figures/tables/illustrations	3
Format	both print and electronic
Are you the author of this Elsevier article?	No
Will you be translating?	No
Title	ULTRAWIDE STOP BAND IN A 3D ELASTIC METAMATERIAL WITH INERTIAL AMPLIFICATION MECHANISMS HAVING CROSS FLEXURE HINGES
Institution name	BOGAZICI UNIVERSITY
Expected presentation date	Jan 2022

Figure D.1. Elsevier license of [4] for Figures 3.7, 3.8, and 3.10.

APPENDIX E: ELSEVIER LICENSE NUMBER 5236890878590

ELSEVIER LICENSE
TERMS AND CONDITIONS

Jan 27, 2022

This Agreement between bogazici university -- sedef nisan otlu ("You") and Elsevier ("Elsevier") consists of your license details and the terms and conditions provided by Elsevier and Copyright Clearance Center.

License Number	5236890878590
License date	Jan 27, 2022
Licensed Content Publisher	Elsevier
Licensed Content Publication	International Journal of Solids and Structures
Licensed Content Title	Design, analysis and experimental investigation of three-dimensional structures with inertial amplification induced vibration stop bands
Licensed Content Author	S. Taniker,C. Yilmaz
Licensed Content Date	Oct 15, 2015
Licensed Content Volume	72
Licensed Content Issue	n/a
Licensed Content Pages	10
Start Page	88
End Page	97
Type of Use	reuse in a thesis/dissertation
Portion	figures/tables/illustrations
Number of figures/tables/illustrations	3
Format	both print and electronic
Are you the author of this Elsevier article?	No
Will you be translating?	No
Title	ULTRAWIDE STOP BAND IN A 3D ELASTIC METAMATERIAL WITH INERTIAL AMPLIFICATION MECHANISMS HAVING CROSS FLEXURE HINGES
Institution name	BOGAZICI UNIVERSITY
Expected presentation date	Jan 2022

Figure E.1. Elsevier license of [5] for Figures 3.9, 3.11 and 3.12.